UNIVERSITY OF CALIFORNIA

Los Angeles

Methodologies and Applications of MicroED

A dissertation submitted in partial satisfaction of the

requirements for the degree Doctor of Philosophy

in Molecular Biology

by

Cody Gillman

2023

ABSTRACT OF THE DISSERTATION

Methodologies and Applications of MicroED

by

Cody Gillman

Doctor of Philosophy in Molecular Biology

University of California, Los Angeles, 2023

Professor Tamir Gonen, Chair

Since its advent in 2013, Microcrystal Electron Diffraction (MicroED) has revolutionized structural determination across a spectrum of samples, encompassing small organic molecules to proteins. MicroED closed a crucial gap between the determination of structures from 2D crystals and 3D crystals, facilitating the study of small 3D crystals that are too small for analysis by X-ray diffraction. The structures of molecules that were previously intractable using other existing structural methodologies have been finally determined using MicroED. As MicroED is an emerging cryogenic electron microscopy (cryo-EM) technique, forging an entirely new branch in the field of structural biology, it is still under active development. The early success of MicroED was largely enabled by technological advancements introduced in cryo-EM, including high performance cameras and state-of-the-art electron microscopes. More recently, the

implementation of focused ion beam (FIB) milling has opened many new avenues for MicroED. Crystal samples of any kind can be thinned to a suitable thickness for MicroED using a FIB mill. It is now possible to access crystals that are submerged in surrounding media or otherwise too large for the transmission of electrons. This work seeks to further develop the application of FIB milling in the MicroED workflow to solve critical issues related to sample preparation. The innovative methodologies that were designed and demonstrated in this thesis have accelerated MicroED development and will allow structural biologists to determine challenging molecular structures more rapidly.

The dissertation of Cody Gillman is approved.

Jeffrey S. Abramson

Ambre M. Bertholet

Stephen C. Cannon

Ernest M. Wright

Tamir Gonen, Committee Chair

University of California, Los Angeles

2023

Dedication

This thesis is dedicated to the Washington Student Achievement Council (WSAC) of Washington State. During my 2008-2009 senior year of high school, WSAC awarded me with the Passport to College Promise Scholarship. The Passport to College program was founded in 2008 to help students from foster care attend and succeed in college. Before receiving this award as a surprise in the mail one day, I had no plans of attending university. My life was set on a very different course that day. Roughly 2% of ex-foster youth graduate from a four-year university and a much smaller percentage go on to receive a PhD. Managing the difficulties of rigorous study causes an unfortunately high number of ex-foster youth to forego pursuing a college degree. I was also fortunate to be assigned amazing and dedicated social care workers while I was a foster youth. They helped me gain crucial life skills and confidence in my abilities to face and overcome adversity. I thank them every day for their service.

Table of Contents

List of Tables

Chapter 3: A comprehensive protocol for MicroED sample preparation

Chapter 4: Design and implementation of suspended drop crystallization

Chapter 5: Eliminating the missing cone challenge through innovative approaches

Chapter 6: The structure of the neurotoxin palytoxin determined by MicroED

List of Figures

Chapter 2: An overview of Microcrystal Electron Diffraction (MicroED)

Chapter 3: A comprehensive protocol for MicroED sample preparation

Chapter 4: Design and implementation of suspended drop crystallization.

Chapter 5: Eliminating the missing cone challenge through innovative approaches

Chapter 6: The structure of the neurotoxin palytoxin determined by MicroED

Acknowledgements

I would like to thank my PhD thesis advisor, Dr. Tamir Gonen. From the beginning, Tamir set a high bar for me in the lab, and it has been a difficult climb. He has shown me an immense amount of support and I thank him for his incredible patience. Tamir's inspiring vision and quest for precision in the research he conducts has set a valuable example for me and I am grateful.

I would like to thank all the members of the Gonen lab who I have had the pleasure of working alongside during my PhD research. They provided me with support when I need it most. I thank Dr. William Nicolas (HHMI) for useful discussions that contributed to Chapter 3 and Dr. Steve Halaby for work that contributed to Chapter 5.

All the work presented in this thesis was supported by funds from the National Institutes of Health, National Institute of General Medical Sciences (NIGMS) grant No. P41GM136508 awarded to Dr. Gonen, the US Department of Defense, Defense Threat Reduction Agency grant No. HDTRA1-21-1-0004 awarded to Dr. Gonen, and funds from the Howard Hughes Medical Institute.

The work in Chapters 3-6, in addition to the funding listed above, was further supported by the National Institutes of Health, National Institute of Arthritis and Musculoskeletal and Skin Diseases (NIAMS) grant No. T32AR065972 awarded to me.

VITA

Cody Gillman

https://orcid.org/0000-0002-3548-9200

EDUCATION

Master of Science, Chemistry (2014-2016) Central Washington University

Thesis advisor: Dr. Todd Kroll

Bachelor of Science, Chemistry (2009-2014) Central Washington University

Biochemistry Specialization

HONORS

Margaret C. Etter Student Lecturer Award	ACA Conference, 2023
Audree Fowler Fellowship in Protein Science	UCLA, 2022
NIH T32 Pre-doctoral Fellowship (MCBPT)	UCLA, 2022
Whitcome Pre-doctoral Fellowship in Molecular Biology	UCLA, 2021
SOURCE 2016 Outstanding Presentation Award	CWU, 2016
Graduate Student Summer Research Fellowship	CWU, 2015
Master's Research Fellowship	CWU, 2014

PUBLICATIONS

9 **Gillman, C.,** Bu, G., Danelius, E., Gonen, T. "Eliminating the missing cone challenge through innovative approaches". (Submitted).

8 **Gillman, C.,** Weaver S, Clabbers, M, Shiriaeva, A, Sae Her, A, , Martynowycz M, and Gonen, T (2023) A comprehensive protocol for sample preparation for MicroED. (Submitted).

7 **Gillman, C.,** Patel, K., Unge, J. & Gonen, T. (2023) The structure of the neurotoxin palytoxin determined by MicroED. Biorxiv. PMID: 37034718.

6 **Gillman, C.,** Nicolas, W. J., Martynowycz, M. W. & Gonen, T. (2023) Design and implementation of suspended drop crystallization. IUCrJ, 10. PMID: 37223996.

5 Mu, X., **Gillman, C.**, Nguyen C, Gonen T. (2021) An Overview of Microcrystal Electron Diffraction (MicroED). Annu Rev Biochem, 90(1): 431–50. PMID: 34153215.

4 Mitachi, K., Kansal, R. G., Hevener, K. E., **Gillman, C. D.**, Hussain, S. M., Yun, H. G., Miranda-Carboni, G. A., Glazer, E. S., Clemons, W. M., & Kurosu, M. (2020) DPAGT1 Inhibitors of Capuramycin Analogues and Their Antimigratory Activities of Solid Tumors. J Med Chem, 63(19): 10855–10878. PMC7554145.

3 Mitachi, K., Yun, H. G., **Gillman, C. D.**, Skorupinska-Tudek, K., Swiezewska, E., Clemons Jr, W. M., & Kurosu, M. (2019) Substrate Tolerance of Bacterial Glycosyltransferase MurG: Novel Fluorescence based Assays. ACS Infect Dis, 6(6): 1501-1516. PMC7286788.

2 Mitachi, K., Kurosu, S. M., **Gillman, C. D.**, Yun, H. G., Clemons Jr, W. M., & Kurosu, M. (2019) A practical synthesis of a novel DPAGT1 inhibitor, aminouridyl phenoxypiperidinbenzyl butanamide (APPB) for in vivo studies. MethodsX, 6: 2305-2321. PMC6812346.

1 Groves, J. A., **Gillman, C.**, DeLay, C. N., & Kroll, T. T. (2019) Identification of Novel Binding Partners for Transcription Factor Emx2. The Protein Journal, 38(1): 2-11.

PATENTS

1 U.S. Patent No. 63/387,479 entitled SUSPENDED SAMPLE GROWTH DEVICE FOR IMAGING APPLICATIONS, filed on 12/14/2022.

SERVICE

2023 Graduate Student Panelist, Student Orientation, *UCLA Bruin Guardian Scholars (BGS)*

2022 Event Volunteer, End of Year Celebration, *UCLA Bruin Guardian Scholars (BGS)*

2021 Graduate Student Panelist, Student Orientation, *UCLA Bruin Guardian Scholars (BGS)*

Chapter 1: Introduction

Microcrystal electron diffraction (MicroED) is a cryogenic electron microscopy (cryo-EM) technique that adapts electron diffraction movies acquired in a cryogenic transmission electron microscope (cryo-TEM) to data processing programs first developed for x-ray crystallography[1]. In MicroED, submicron-sized 3D nanocrystals are diffracted by a focused electron beam in the cryo-TEM while the sample stage is continuously rotated, and a diffraction movie is recorded using a fast camera. Although electron diffraction of frozen-hydrated crystals in cryo-TEMs was first reported in 1974 for thin crystals of the membrane protein catalase[2], electron crystallography was not routinely applied to 3D crystals due to challenges associated with radiation damage and diffraction pattern indexing[3]. In 2013, Shi et al. demonstrated that if the exposure to the electron beam was dramatically reduced, a single 3D nanocrystal could tolerate more than 90 exposures with limited radiation damage. This study generated the first near-atomic resolution protein structure from 3D microcrystals using electron diffraction, leading to the birth of MicroED as a distinct branch of cryo-EM[1].

With the recent surge of technological improvements introduced to cryo-EM in the last decade, MicroED is becoming an increasingly important tool for structure investigation of proteins and small molecules for drug discovery. It is possible to diffract small crystals that are a billion times smaller than crystals routinely used for x-ray neutron crystallography in MicroED because electrons interact more strongly with matter than x-rays do[4,5]. After it was discovered that seemingly amorphous powers often contain nanocrystals[6], MicroED opened a new pathway for the routine and rapid determination of

atomic resolution structures from complex small molecule mixtures without any purification or crystallization trials necessary. To date, there are close to 100 PDB entries reporting MicroED structures and the number of entries is growing at a rapid rate for globular proteins, membrane proteins, protein complexes, peptides, and chemicals compounds**.**

MicroED holds tremendous potential in the field of membrane protein structure because membrane proteins often form small crystals that are difficult to study using X-ray crystallography[7–9]. Several novel membrane protein structures have already been determined by MicroED[10–13]. Employing lipid-based crystallization techniques such as lipidic cubic phase (LCP)[14], bicelle crystallization[15], and lipid reconstitution[16] as a strategy for determining membrane protein structures is possible and attractive in MicroED because it is often difficult to produce crystals that meet the size requirements of X-ray crystallography using these techniques. Pursuing structures of membrane proteins in lipid-bilayer environments rather than detergent micelles environments is important because in the absence of long-chain lipids stacking parallel against transmembrane helices, as in the native environment of the cell lipid bilayer, detergent micelles may allow membrane proteins to adopt low-energy (i.e., non-native) structural conformations[17–19].

In **Chapter 2** of this manuscript, an overview of MicroED is presented. MicroED is compared with the other cryo-EM modalities, which include cryo-tomography, single particle analysis, and 2D electron crystallography. As a relatively new cryo-EM modality, MicroED filled a crucial gap between the determination of structures from thin 2D crystals and large 3D crystals, facilitating the study of small 3D crystals. The distinct advantages of MicroED in various applications including drug discovery and protein structure is

discussed in detail. Next, the workflow, from preparation of MicroED crystal samples to data collection and processing, is discussed. Also in this section is an introduction to how cryogenic focused ion beam (FIB) milling has been implemented in the MicroED workflow for samples that are too thick for electron transmission. Since MicroED is ideally suited for protein nanocrystals[20,21], when crystals are too thick for traditional MicroED, thereby blocking the transmission of scattered electrons, thinning the crystals using cryo-FIB milling prior to MicroED diffraction is a powerful approach. Last in this section are discussions of the areas of MicroED that are still under development, including overcoming radiation damage and solving the phase problem. This work has been published as:

Mu, X., Gillman, C., Nguyen C, Gonen T. (2021) An Overview of Microcrystal Electron Diffraction (MicroED). Annu Rev Biochem, 90(1): 431–50.

In **Chapter 3,** a comprehensive protocol for MicroED sample preparation is presented. This manuscript starts with an in-depth discussion of the history of electron crystallography and how sample preparation procedures have evolved over time. This is followed by an overview of the considerations that should typically be made during the design of a MicroED experiment based on the nature of the crystal sample. A specialized protocol for milling crystals of membrane proteins grown in lipidic cubic phase (LCP) was developed in the Gonen lab and is includes as well as a protocol for suspended drop crystallization, which allows users to bypass sample transfer and blotting. This work has been submitted as:

Weaver S, Clabbers, M, Shiriaeva, A, Sae Her, A, Gillman, C, Martynowycz M, and Gonen, T (2023) A comprehensive protocol for sample preparation for MicroED. (*Submitted*).

In **Chapter 4,** an alternative workflow for MicroED dubbed “suspended drop crystallization” is presented. The conventional workflow for MicroED entails transferring the crystal sample from the crystallization tray to an EM grid with a perforated carbon support film. The EM grid is then blotted to remove excess crystallization media and plunge frozen in liquid ethane or nitrogen. In some cases, physically transferring and blotting crystal samples are challenging steps to perform and can introduce significant bottlenecks during sample preparation. In suspended drop crystallization, a novel method for crystal growth that we envisaged is employed that allows one to bypass both the crystal transfer and blotting steps during sample preparation. Here, the protein sample and precipitant are mixed directly on a bare EM grid that is absent of the perforated carbon support film. Because vapor diffusion can occur from all sides of the drop, the drop is effectively “suspended” by the grid bars alone. An apparatus that allows the grid to be suspended above crystallization mother liquor during crystal growth was designed and 3D printed in-house. Once crystals have formed, the grid with drop is removed, frozen, and crystals are access by generating a lamella with a cryo-FIB/SEM. The prepared lamella is then transferred to a cryo-TEM and MicroED data is acquired. Suspended drop crystallization overcomes many of the challenges associated with sample preparation, providing an alternative workflow for crystals embedded in viscous media, sensitive to mechanical stress, and/or suffering from preferred orientation on EM grids. This work has been published as:

Gillman, C., Nicolas, W. J., Martynowycz, M. W. & Gonen, T. (2023) Design and implementation of suspended drop crystallization. IUCrJ, 10.

In **Chapter 5,** a new methodology that solves a technical issue sometimes experienced in MicroED – referred to as the "missing cone" – is presented. The missing wedge is a hurdle that occurs when crystals with plate-like morphologies recurrently adopt a preferential orientation on the EM grid, lying flat with one axis perpendicular to the support surface. When this is the case, all acquired MicroED datasets represent the same wedge of reciprocal space, thus merging multiple datasets together is nonadditive and fails to improve dataset completeness. Without the missing wedge of data, it may not be possible to make a structure determination. In cases where a structure can be determined, despite the low dataset completeness, the quality of the density map will be poor. To address the missing cone problem, we designed an experimental approach that allows one to directly target the missing wedge of the crystal lattice using a workflow similar to that demonstrated in "suspended drop crystallization". A slurry of crystals that would otherwise adopt preferred orientations was added to a support-free grid and crystals were frozen in random orientations. The crystals that appeared as thin needles rather than plates when viewed normal to the grid surface were targeted for cryo-FIB milling. The crystal fragment that was preserved in the milled lamella presented the missing wedge of the crystal lattice and a MicroED diffraction dataset was collected. This dataset was merged with previously obtained datasets representing the preferred orientation. The missing cone was filled, and the completeness significantly improved. The structure statistics and map quality also significantly improved. This work has been submitted as:

Gillman, C., Bu, G., Danelius, E., Nannenga, B., Gonen, T. (2023) Capturing the missing wedge in MicroED. (*Submitted*).

In **Chapter 6,** the MicroED structure of palytoxin (PTX), a potent neurotoxin produced by marine corals of the genus *Palythoa*, is presented. PTX is a 2.7 kDa nonproteinacious molecule that binds the integral membrane protein complex Na,K-ATPase very tightly and is an extremely lethal poison[22–27]. Na,K-ATPase maintains the electrochemical gradient of sodium and potassium across the plasma membrane by hydrolyzing ATP to pump three sodium ions outside the cell and two potassium ions inside the cell[28]. When bound by PTX, Na,K-ATPase is converted from an active ion pump to a passive cation pore that allows sodium and potassium to move down their concentration gradients[27,29,30]. The irreversible depolarization of the membrane results in violent contraction of skeletal muscles, heart failure[31], hemolysis[32], platelet aggregation[33], bone resorption[34], and tumorigenesis[35].

Following isolation from *Palythoa*, the dinoflagellate *Ostreopsis* spp. was found to also be a primary producer of PTX and many different analogues[25]. Inhalation of *Ostreopsis* during blooming events has caused many cases of severe illness and hospitalization[36]. In tropical waters containing PTX producers, PTX can move up the food chain and accumulate to deadly levels in popular seafood, including fish, crabs, sea urchins, and mussels[24,37–40]. Cases of exposure also occur when aquarium hobbyists mishandle *Palythoa* coral or inhale aerosolized PTX[41,42]. To date, there are no known treatments for PTX exposure other than direct injection to the heart immediately after exposure[43]. Despite over a half century of scientific investigation, very little has been

uncovered regarding the three-dimensional structure of palytoxin when bound to Na,K-ATPase.

We determined the first 3D structure of PTX in complex with a short chain variable fragment (scFv) using MicroED at 3.2 Å resolution. The 3D binding mode of PTX determined by the MicroED structure was used to perform docking simulations to determine the potential binding mode of PTX on Na,K-ATPase. This study provides valuable insights on the mechanism of PTX, which can be used in the development of anti-PTX molecules that inhibit the binding of PTX on Na,K-ATPase. This work has been submitted as:

> Gillman, C., Patel, K., Unge, J. & Gonen, T. (2023) The structure of the neurotoxin palytoxin determined by MicroED. *Biorxiv preprint (submitted). doi: 10.1101/2023.03.31.535166*

References

1. Shi, D., Nannenga, B. L., Iadanza, M. G. & Gonen, T. Three-Dimensional Electron Crystallography of Protein Microcrystals. *Elife* **2**, 1345.

2. Taylor, K. A. & Glaeser, R. M. Electron Diffraction of Frozen, Hydrated Protein Crystals. *Science (1979)* **186**, 1036–1037.

3. Martynowycz, M. W. & Gonen, T. From Electron Crystallography of 2D Crystals to MicroED of 3D Crystals. *Curr Opin Colloid Interface Sci* **34**, 9–16.

4. Henderson, R. The potential and limitations of neutrons, electrons and X-rays for atomic resolution microscopy of unstained biological molecules. *Q Rev Biophys* **28**, 171–193 (1995).

5. Nannenga, B. L. & Gonen, T. The cryo-EM method microcrystal electron diffraction (MicroED). *Nat Methods* **16**, 369–379 (2019).

6. Newman, J. A. *et al.* From Powders to Single Crystals: A Crystallographer's Toolbox for Small-Molecule Structure Determination. *Molecular Pharmaceutics, May* doi:10.1021/acs.molpharmaceut.2c00020.

7. Yonekura, K., Kato, K., Ogasawara, M., Tomita, M. & Toyoshima, C. Electron crystallography of ultrathin 3D protein crystals: Atomic model with charges. *Proceedings of the National Academy of Sciences* **112**, 3368–3373 (2015).

8. Xu, H. *et al.* Solving a new R2lox protein structure by microcrystal electron diffraction. *Sci Adv* **5**, eaax4621 (2019).

9. Bill, R. M. *et al.* Overcoming barriers to membrane protein structure determination. *Nat Biotechnol* **29**, 335–340 (2011).

10. Liu, S. & Gonen, T. MicroED structure of the NaK ion channel reveals a Na+ partition process into the selectivity filter. *Commun Biol* **1**, 1–6 (2018).

11. Martynowycz, M. W., Khan, F., Hattne, J., Abramson, J. & Gonen, T. MicroED structure of lipid-embedded mammalian mitochondrial voltage dependent

anion channel. *bioRxiv* 2020.09.17.302109 (2020) doi:10.1101/2020.09.17.302109.

12. Shiriaeva, A., Martynowycz, M. W., Nicolas, W. J., Cherezov, V. & Gonen, T. MicroED structure of the human vasopressin 1B receptor. *Biorxiv: the preprint server* (2023).

13. Martynowycz, M. W. *et al.* MicroED Structure of the Human Adenosine Receptor Determined from a Single Nanocrystal in LCP. *Proc Natl Acad Sci U S A* **118**, 2106041118.

14. Ujwal, R. & Bowie, J. U. Crystallizing membrane proteins using lipidic bicelles. *Methods* **55**, 337–341 (2011).

15. Faham, S. & Bowie, J. U. Bicelle Crystallization : A New Method for Crystallizing Membrane Proteins Yields a Monomeric Bacteriorhodopsin Structure. 1–6 (2002) doi:10.1006/jmbi.2001.5295.

16. Gonen, T. *et al.* Lipid-Protein Interactions in Double-Layered Two-Dimensional AQP0 Crystals. *Nature* **438**, 633–638.

17. Hunte, C. & Richers, S. Lipids and membrane protein structures. *Curr Opin Struct Biol* **18**, 406–411 (2008).

18. Westerlund, A. M., Fleetwood, O., Pérez-Conesa, S. & Delemotte, L. Network analysis reveals how lipids and other cofactors influence membrane protein allostery. *J Chem Phys* **153**, 141103 (2020).

19. Ujwal, R. & Abramson, J. High-throughput Crystallization of Membrane Proteins Using the Lipidic Bicelle Method. *Journal of Visualized Experiments* e3383 (2012) doi:10.3791/3383.

20. Mu, X., Gillman, C., Nguyen, C. & Gonen, T. An Overview of Microcrystal Electron Diffraction (MicroED). *Annu Rev Biochem* **90**, 431–450 (2021).

21. Nannenga, B. L. & Gonen, T. The cryo-EM method microcrystal electron diffraction (MicroED). *Nat Methods* **16**, 369–379 (2019).

22. Böttinger, H., Béress, L. & Habermann, E. Involvement of (Na+ + K+)-ATPase in binding and actions of palytoxin on human erythrocytes. *BBA - Biomembranes* **861**, 165–176 (1986).

23. Riobó, P. & Franco, J. M. Palytoxins: Biological and chemical determination. *Toxicon* **57**, 368–375 (2011).

24. Taniyama, S. *et al.* Ostreopsis sp., a possible origin of palytoxin (PTX) in parrotfish Scarus ovifrons. *Toxicon* **42**, 29–33 (2003).

25. Usami, M. *et al.* Palytoxin analogs from the dinoflagellate Ostreopsis siamensis. *J Am Chem Soc* **117**, 5389–5390 (1995).

26. Ukena, T. *et al.* Structure Elucidation of Ostreocin D, a Palytoxin Analog Isolated from the Dinoflagellate Ostreopsis siamensis. *Biosci Biotechnol Biochem* **65**, 2585–2588 (2014).

27. Habermann, E. Palytoxin acts through Na+, K+-ATPase. *Toxicon* **27**, 1171–1187 (1989).

28. Christian Skou, J. I. & Esmann, M. I. The Na,K-ATPase. *J Bioenerg Biomembr* **24**, (1992).

29. Ozaki, H., Nagase, H. & Urakawa, N. Interaction of palytoxin and cardiac glycosides on erythrocyte membrane and (Na++ K+) ATPase. *Eur J Biochem* **152**, 475–480 (1985).

30. Wang, X. & Horisberger, J. D. Palytoxin effects through interaction with the Na,K-ATPase in Xenopus oocyte. *FEBS Lett* **409**, 391–395 (1997).

31. Artigas, P. & Gadsby, D. C. Na+/K+-pump ligands modulate gating of palytoxin-induced ion channels. *Proc Natl Acad Sci U S A* **100**, 501–505 (2003).

32. Tubaro, A., Sosa, S. & Hungerford, J. *Toxicology and diversity of marine toxins. Veterinary toxicology: basic and clinical principles*. (Academic press, 2012).

33. Nagase, H., Karaki, H., Ozaki, H. & Azuma, H. Palytoxin, a novel and potent platelet activator. in *JAPANESE JOURNAL OF PHARMACOLOGY* vol. 43 P290--P290 (1987).

34. Lazzaro, M., Tashjian Jr., A., Fujiki, H. & Levinef, L. Palytoxin : An Extraordinarily Potent Stimulator of. *Endocrinology* **120**, 1338–1345 (1987).

35. Aligizaki, K., Katikou, P., Milandri, A. & Diogène, J. Occurrence of palytoxin-group toxins in seafood and future strategies to complement the present state of the art. *Toxicon* **57**, 390–399 (2011).

36. Ciminiello, P. *et al.* The Genoa 2005 Outbreak. Determination of Putative Palytoxin in Mediterranean Ostreopsis o vata by a New Liquid Chromatography Tandem Mass Spectrometry Method. *Anal Chem* **78**, 6153–6159 (2006).

37. Patocka, J., Gupta, R. C., Wu, Q. & Kuca, K. Toxic potential of palytoxin. *Journal of Huazhong University of Science and Technology [Medical Sciences]* **35**, 773–780 (2015).

38. Fukui, M., Murata, M., Inoue, A., Gawel, M. & Yasumoto, T. Occurrence of palytoxin in the trigger fish Melichtys vidua. *Toxicon* **25**, 1121–1124 (1987).

39. Deeds, J. R. & Schwartz, M. D. Human risk associated with palytoxin exposure. *Toxicon* **56**, 150–162 (2010).

40. Rhodes, L., Towers, N., Briggs, L., Munday, R. & Adamson, J. Uptake of palytoxin-like compounds by shellfish fed Ostreopsis siamensis (Dinophyceae). *N Z J Mar Freshwater Res* **36**, 631–636 (2002).

41. Hoffmann, K. *et al.* A case of palytoxin poisoning due to contact with zoanthid corals through a skin injury. *Toxicon* **51**, 1535–1537 (2008).

42. Rumore, M. M. & Houst, B. M. Palytoxin poisoning via inhalation in pediatric siblings. *Int J Case Rep Images* **5**, 501–504 (2014).

43. Wiles, J. S., Vick, J. A. & Christensen, M. K. Toxicological evaluation of palytoxin in several animal species. *Toxicon* **12**, 427–433 (1974)

Chapter 2: An overview of Microcrystal Electron Diffraction (MicroED)

Xuelang Mu[1,2,3*], Cody Gillman[1,2,3*], Chi Nguyen[1*] and Tamir Gonen[1,2,3$]

[1] Howard Hughes Medical Institute, Department of Biological Chemistry, University of California, Los Angeles, Los Angeles CA 90095 USA

[2] Molecular Biology Institute, University of California, Los Angeles, Los Angeles CA 90095 USA

[3] Howard Hughes Medical Institute, Department of Physiology, University of California, Los Angeles, Los Angeles CA 90095 USA

[*] Authors contributed equally

[$] Correspondence to T.G. (tgonen@g.ucla.edu)

Abstract

The bedrock of drug discovery and a key tool for understanding cellular function and drug mechanisms of action is the structure determination of chemical compounds, peptides, and proteins. The development of new structure characterization tools, particularly those that fill critical gaps in existing methods, presents important steps forward for structural biology and drug discovery. The emergence of microcrystal electron diffraction (MicroED) expands the application of cryo–electron microscopy to include samples ranging from small molecules and membrane proteins to even large protein complexes using crystals that are one-billionth the size of those required for X-ray crystallography. This review outlines the conception, achievements, and exciting future trajectories for MicroED, an important addition to the existing biophysical toolkit.

Introduction

Cryo electron-microscopy (CryoEM) encompasses techniques that use a transmission electron microscope (TEM) to extract structural information about cellular, protein, peptides, and chemical samples[1–3]. Since its inception, CryoEM has provided complimentary methods for structural determination of samples that may be intractable by other structural techniques.

To date, of the nearly 150,000 protein structures deposited in the PDB, 90%, 8%, and 2% were solved by X-ray crystallography, NMR, and CryoEM, respectively. Despite trailing in the overall number of structures determined, CryoEM has experienced a recent surge driven by the advent of improved hardware[4–6] data processing software[7–10], and innovative practices for sample preparation[11]. Progress in detector technology, in particular, arguably had the greatest impact on the recent successes in CryoEM[12]. As a result, the number of high-resolution structures determined by these techniques has grown at a rapid rate since the first atomic-resolution cryoEM protein structure was determined in 2005[13]. Further, since cryoEM facilities have become much more readily accessible in the last decade, on track to be on the scale of X-ray crystallography, structural biologists around the globe are increasingly becoming equipped to tackle notoriously difficult targets and to push the resolution limits that can be achieved by CryoEM[14]. Owing to this progress, in 2017, for the first time, CryoEM surpassed NMR for the number of annual entries in the PDB[15].

In this chapter, the accomplishments and future directions of the CryoEM technique microcrystal electron-diffraction (MicroED) are discussed. MicroED was developed for structure determination of proteins using very small 3D microcrystals[16]. In 2013, Shi et al.

demonstrated that a single 3D lysozyme crystal could tolerate more than 90 exposures with limited radiation damage, if the exposure to the electron beam was dramatically reduced by two orders of magnitude. This seminal study generated the first near-atomic resolution protein structure from 3D microcrystals using electron diffraction, leading to the birth of MicroED as a distinct branch in cryoEM modalities[16]. Since 2013, numerous improvements in the MicroED workflow and technology have been invented and implemented to streamline and democratise the application of MicroED for broader use.

CryoEM modalities include single particle analysis (SPA)[17–19], cryo-electron tomography (cryo-ET)[20–22], two-dimensional (2D) electron crystallography[23,24] and MicroED[16,54] (Figure 2.1).

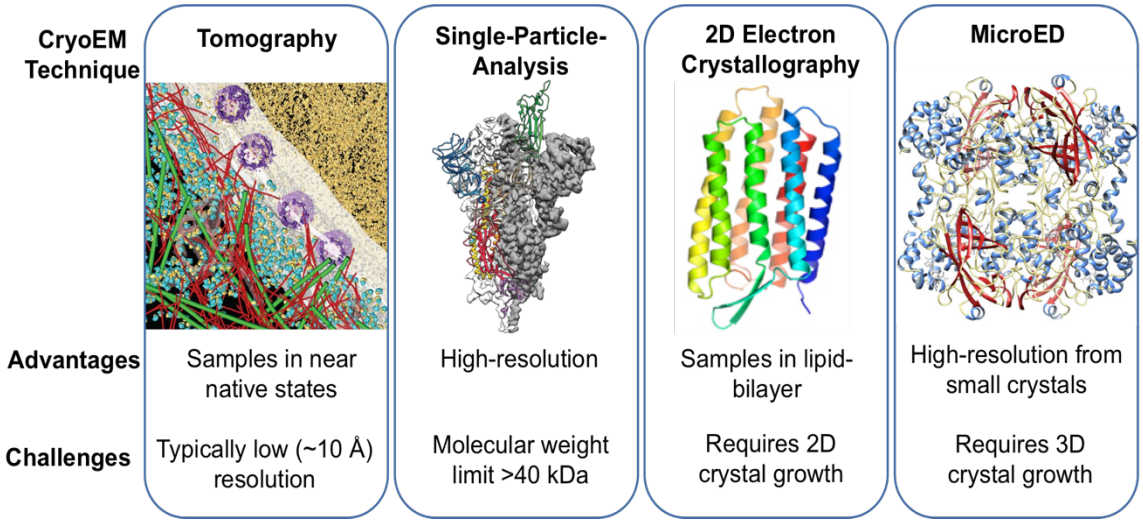

Figure 2.1. Four modalities of cryoEM. From left to right. A model of the HeLa cell nuclear periphery[25] (Reprint permission from AAAS) by tomography. Model of COVID-19 spike protein by SPA[26] (Reprint with permission from AAAS). The structure of bacteriorhodopsin determined by electron crystallography[27] of 2D crystals (Reprint from reference 36) and the structure of catalase determined by MicroED[28] of 3D crystals (Reprint from reference 37).

SPA uses high-magnification imaging of purified samples, typically proteins, for reconstruction of 3D models[29]. During SPA, thousands of 2D projection images of ice-embedded particles are captured. Because particles are often positioned in random orientations on the EM grid, the images can be classified based on particle orientation using alignment algorithms[10,30,31]. The 2D projection averages obtained are then used to reconstruct 3D models[32–34]. Since SPA does not require crystallization, this technique is ideal for proteins that resist forming well-ordered crystals, typical of large complexes and flexible or highly dynamic proteins. Another advantage to SPA is the ability to capture different conformational states of proteins, particularly those regions that may have a high degree of flexibility[35]. There are, however, many challenges intrinsic to SPA, including bottlenecks associated with sample preparation, vitrification, and imaging, that make obtaining high-resolution information difficult. The molecular weight limit is arguably the greatest caveat of SPA. It is exceedingly difficult to determine the structures of particles with molecular weights below 40 kDa[36,37], which is bigger than the average size of a protein in the cell.

In CryoET, imaging by TEMs is used to generate models of proteins in the context of their native cellular environments[38–41]. This technique provides valuable insights into subcellular localization and organization of macromolecular complexes[41], in particular those that may be too transient or difficult to capture *in vitro.* The workflow for CryoET is similar to SPA, with a few key differences. Instead of purified proteins, whole microorganisms or cells are vitrified on the EM grid and sliced into thin cross-sections using a scanning electron microscope coupled with a focused ion beam (FIB-SEM)[42–44]. Images are taken at different tilt angles, aligned, and merged to produce 3D

reconstructions of the region of interest[22,45,46]. The clear advantage of CryoET is the ability to recapitulate models of macromolecular complexes within the context of their native cellular environment[38–41,47]. The major drawbacks of CryoET are low-throughput workflow and difficulties in achieving high-resolution[48]. The latter is mainly due to repeated high electron dose exposure required for imaging of a single region leading to severed beam induced radiation damage.

Unlike SPA and CryoET, which depend on imaging, 2D electron crystallography and MicroED can also take advantage of diffraction. 2D crystallography was developed specifically for membrane proteins that form crystalline material in a lipid bilayer[49]. In the TEM, 2D crystals are diffracted using a focused electron beam. The diffraction patterns are indexed and merged to create a 3D model[50]. The appeal of this technique stems from the ability to stabilize the membrane protein of interest in an environment that mimics the native membrane[51,52] or by directly isolating native 2D crystals from cells[23,53,54]. However, like X-ray crystallography, a major bottleneck for 2D crystallography is often the time-consuming optimization trials required to successfully grow 2D crystals which consumes large amounts of highly pure protein[19]. Another limitation is that 2D crystals are highly susceptible to radiation damage[2,17]. As such, acquiring a complete dataset in 2D electron crystallography often requires diffraction and merging of data from hundreds or thousands of individual crystals[13,55,56].

MicroED was developed as a hybrid method that exploits the advantages of both cryoEM and X-ray crystallography[16,53]. In MicroED (Figure 2.2), an electron beam set at an ultra-low dose rate is used for diffraction from 3D crystals that are a billionth the size that is required for X-ray crystallography[57]. During the exposure, the crystal is continuously rotated by the sample stage[58,59] as the data is recorded as a movie using a fast camera. Each frame in this movie contains a wedge of reciprocal space so the data can be processed using standard X-ray crystallographic software to generate 3D models[60]. The main advantage of MicroED is the ability to diffract and extract high-resolution structural information from samples that resist forming large crystals while using significantly less material. The charged state of the sample is determined with MicroED because electrons, as charged particles, can probe electrostatic potential of matter[27,61–63], whereas X-rays, in sharp contrast yield an electron density map[64]. Thus, MicroED offers users the advantage of mapping the charged, electrotatic states of atoms in

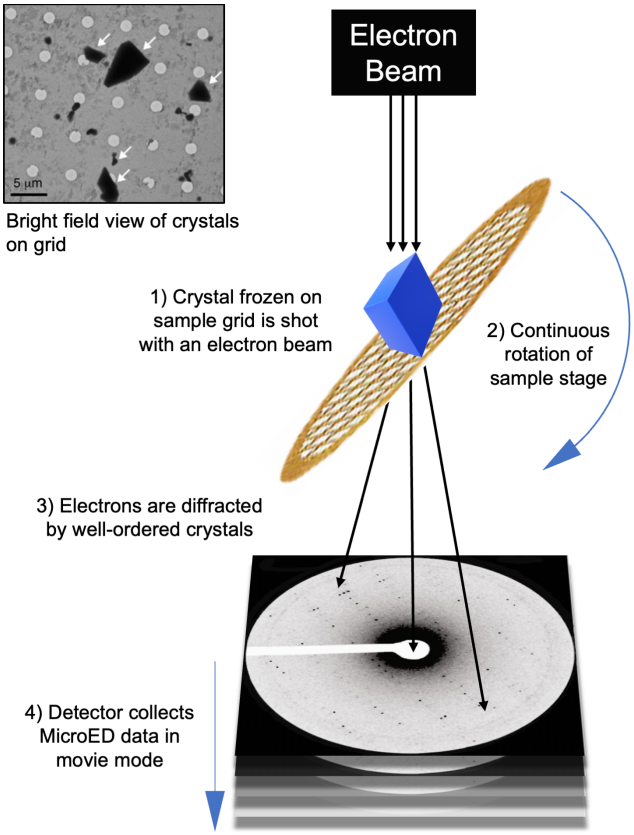

Figure 2.2. Overview of MicroED. An image of an EM grid in bright field during scanning for microcrystals (Top left). Once located, a microcrystal is exposed to an electron beam in diffraction mode while the crystal is continuously rotated on the sample stage. The diffraction data are then collected as movie using a fast camera.

structures. Lastly, all MicroED structures determined to date were done to relatively high resolution.

With the recent surge of technological improvements introduced to CryoEM in the last decade, MicroED is increasingly becoming an important tool for structure investigation of proteins and small molecules for drug discovery. To date, there are close to 100 PDB entries reporting MicroED structures, and the number of entries is growing at a rapid rate for globular proteins, membrane proteins, protein complexes, peptides, and chemicals compounds**.** The application of faster and more sensitive electron detectors, including direct electron cameras, automated pipelines for data collection and analyses, and specialized computational methods is expected to elevate the potential that MicroED holds for transforming the capabilities of macromolecular crystallography.

MicroED Workflow

Growing protein crystals for MicroED follows the same established pipelines as for X-ray crystallography; however, MicroED is useful for extracting structural information from crystals that are a billionth the size required for X-ray diffraction[57]. The initial identification of microcrystals, however, requires practice as they are difficult to visualize under a light microscope[65]. Microcrystals can be identified in crystallization drop experiments using alternatives detection methods including UV fluorescence, Second Order Nonlinear Imaging of Chiral Crystals (SONICC)[66], fluorescence microscopy or negative-stain electron microscopy[67]. Crystallization drops that appear “cloudy,” which are ordinarily considered failed crystallization experiments for X-ray diffraction, should also be carefully inspected as micro- and nano-crystals may be present[62]. Once

microcrystals have been obtained, the crystal solution is transferred to a glow-discharged EM grid, blotted to remove excess solution, and cryo-cooled by plunging into liquid ethane[60]. For anhydrous samples, typically small molecules or natural products, the crystals, often as powder, are applied directly to an EM grids[68] and analyzed under cryogenic conditions[57] to minimize beam damage[69]. In some cases where the samples are robust, MicroED analysis can be conducted without cooling[70]. When larger crystals form (1-5 microns, sizes that are still challenging for traditional X-ray crystallography but too big for MicroED) fragmentation methods[71] or focused ion beam milling on a scanning electron microscope (FIB-SEM) can be used to generate smaller crystals for MicroED[72–75].

Once the sample is on the EM grid, the samples are then loaded onto the TEM under cryogenic conditions for data acquisition. The grid is typically surveyed in bright field mode or overfocused diffraction to assess overall ice thickness and identify sites that contain crystals of appropriate sizes without significant exposure to the damaging beam[76]. Once crystals are located, a test diffraction pattern is recorded to assess crystal quality[76]. This step can be achieved using automated software such as serial EM[77]. If high-quality diffraction is observed, a dataset is recorded on a fast camera as a movie with the electron dose rate (exposure) set to 0.01–0.05 $e^{-}Å^{-2}s^{-1}$ while the crystal is continuously rotated on the sample stage[58,60]. This does rate is ~100x lower than what is used for other cryoEM modalities. Continuous rotation of the sample in MicroED improves the accuracy of the reflection intensities and reduces the effects of dynamical scattering[16,58,60,78] leading to superior datasets compared with still-diffraction.

Continuous rotation of the crystal at a fixed speed during diffraction in MicroED is analogous to the rotation method used in X-ray crystallography where individual frames in the MicroED movie contain a wedge of reciprocal space[76,79]. As such, MicroED data can be directly processed using standard crystallographic software[72,80]. MicroED data has been successfully indexed, integrated, and scaled using standard X-ray crystallography software including XDS[81], iMOSFLM[82], DIALS[83], SHELX[84], and HKL2000[80]. High-resolution (better than ~1.2 Å) datasets are required for solving structures by ab initio methods[84]. As such, historically, the majority of protein structures solved by MicroED have depended on molecular replacement to solve the phase problem, which is contingent upon the availability of a search model with high homology[85]. Recent breakthroughs in phasing strategies including the use of imaging[86–89], fragment based phase extension[27], ARCIMBOLDO[90], and radiation damage[91] have been successful as alternative methods to phasing.

Advantages and Application of Microcrystals for MicroED

The growth of large and well-ordered single crystals suitable for X-ray analysis is a major rate-liming step for structure determination of proteins[92], especially those that are localized to the membrane or form complexes. Quality biochemical preparation of protein samples is essential for all structural characterization. This includes determining the conditions to obtain highly pure andar stable protein or their complex of interest. Because electrons interact with matter more strongly than X-rays and those interactions result in more useful elastic scattering events[65], the crystals needed for MicroED can often be a billionth the size of those needed for X-ray diffraction. As such, MicroED fills an important

gap in biophysics to enable structure elucidation from samples that may not be tractable by other methods.

Small crystals, those that can be used for MicroED, offer several advantages over larger crystals. Small crystals are typically much easier to obtain than larger ones, which typically also contain more detrimental pathologies such as twinning, multiple and/or mosaic lattices[71,93] Smaller crystals suffer less long-range defects and tend to be better ordered. Line-width analysis of powder protein crystallography has shown that nanocrystals may be more useful, containing fewer defects that contribute to increased mosaicity[49]. Comparative analysis of eight different samples using both X-ray and MicroED found that smaller crystalline domains resulted in higher resolution and better-quality data than the larger parent crystals[71].

The advantage offered by small crystals have expanded the application of MicroED to the study of small organic and inorganic molecules as well as peptides and natural products[16,55,56,94,95]. Between 2016-2018, MicroED made an important leap in method development for structure determination of small molecules as powders instead of grown crystals[57,68,93,96] and directly from mixtures[65]. Chemical compounds often crystallize as multiple different lattices, referred to as polymorphs. The presence of multiple crystal lattices in a single experiment, particularly those in mixtures of small, nano-sized crystals, have posed major hurdles for structural characterization by X-ray diffraction[95]. In sharp contrast, MicroED was able to obtain distinct structures from a mixture of powders containing nano-crystals of several different small-molecules and natural products[57,68]. In these studies, hydrogen atoms of the small-molecules, including Carbamazepine, prescribed today for the treatment of convulsive and bipolar diseases[97,98], were identified

(Figure 2.3). Many other structures of small-molecules have been reported by MicroED recently, including, Grippostad[95], an antiviral drug for treatment of the common cold and the flu[99], and a recent example of the non-fulleren acceptor (NFA) semi-conductive material ITIC-Th (Figure 2.3).

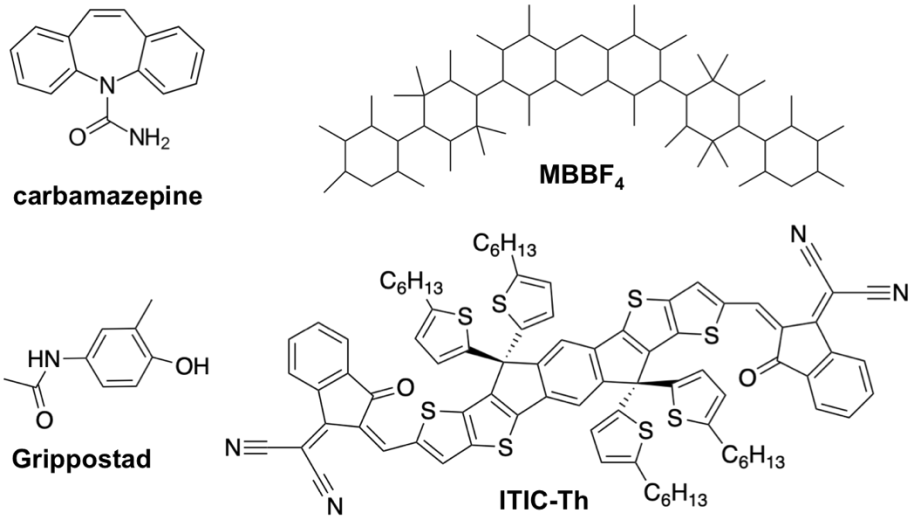

Figure 2.3. Examples of structures of small-molecule chemical compounds by MicroED.

While nanocrystals, not thicker than ~500 nm, are ideal for MicroED, thicker crystals (that are still too small for X-ray) can also be optimized for MIcroED. Large crystals can be trimmed to appropriate sizes for MicroED by mechanical fragmentation

methods[71] or FIB-SEM[72–75]. Several mechanical fragmentation approaches have been applied to prepare large crystals for MicroED, including sonication, vigorous pipetting, and vortexing[71]. Generally, the gentler fragmentation through pipetting is better for fragile samples, while harsher methods, such as vortexing and sonication, are needed to break more robust crystals. As proof-of-principle, eight proteins, lysozyme, xylanase, thaumatin, trypsin, proteinase K, thermolysin, TGF-βm–TßRII, and a segment of the tau protein, with molecular weights ranging from 0.7 to 34.6 kDa and solvent contents between 30% to 60% were fragmented and their structures determined by MicroED[71]. The first six of these proteins are standard model systems. The last two samples, transforming growth factor beta paired type II complex, TGF-βm–TßRII, and a segment of the tau protein, are non-standard and tended to form large, imperfect crystals. In all examples the large crystals were fragmented by one of the three mechanical methods mentioned above before transferring onto cryoEM grids for MicroED. The distribution of micrometer- or nanometer-sized crystal fragments on the EM grid was relatively uniform, and single-crystal data sets were collected by continuous rotation. The standard samples obtained by MicroED are comparable or, in some cases, higher in resolution than those obtained by X-ray diffraction[71]. For the two non-standard samples, the resolution obtained from fragmented crystallites was better than the parent crystals and, in one case, the resolution of the structure improved from 8 Å in X-ray to ~1 Å in MicroED. These results suggest that mechanical fragmentation itself does not lead to additional adverse damage to the crystal lattice and instead is a viable method for sample preparation for MicroED.

FIB milling of frozen protein crystals is another approach for sample preparation for MicroED. During this process, the FIB is used to mill away and remove excess material

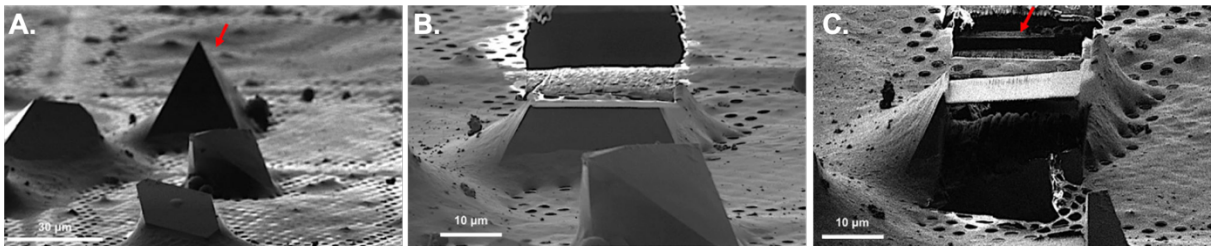

from the crystal to generate lamellae with appropriate thickness for MicroED[72–74,100,101] (Figure 2.4). Pre-coating samples with a thin layer of platinum is used to protect the sample[72]. Platinum coating can also enhance the physical stability of the grid, working as a protective layer above the specimen. Cryo-FIB milling of lysozyme crystals have been shown to preserve the internal structure of trimmed lamellae and could maintain high-resolution diffraction capacity. In combination with MicroED, FIB milled lamellae of crystals generated a 1.9 Å resolution lysozyme structure[72]. To further push the boundaries of samples that could be used for structure determination by FIB mill-MicroED, new crystal "polishing" protocols were established[74]. Using proteinase K as a model system,

Figure 2.4. FIB milling of crystals for MicroED. (A) Image of select proteinase K crystals at high magnification before milling. The arrow indicates the crystal that was milled in (C). (B) FIB image of select crystal from (A) after milling the top of the crystal. (C) FIB image of crystal after milling and cleaning both the top and bottom of the crystal leaving a lamella indicated by an arrow. (Reprint from reference[69]).

a lower-current ion beam was used as a final polishing step of the crystals by trimming away flanking regions of lamellae. Because the final FIB current used was lower, the amount of radiation decay was reduced. This strategy was successful in improving the resolution of the proteinase K crystal lamellae to 1.79 Å[74]. Fragmentation and milling widen the application range crystals sizes suitable for MicroED without significant additional effort required for sample screening.

Structures of proteins bound with small molecule ligands provide important information about mechanism of action, insights that are vital for dissecting protein function to lay the groundwork for drug discovery and development (Discussed further below). These protein-ligand crystal complexes are generated by either co-crystallizing the protein with the ligands or soaking ligands into pre-formed protein crystals[102]. Here, MicroED offers another advantage as diffusion of small molecules into small crystals is more efficient than diffusion into large crystals[103]. A recent study demonstrated that simply soaking small molecules into pre-formed proteinase K microcrystals on TEM grid was sufficient to yield a high-resolution structure where several ligands were observed at high occupancy[104]. Ligand soaked crystals combined with MicroED offers strategies to improve the current drug discovery pipeline.

A robust method for structure determination using single 3D nanocrystals

The very first novel protein structure determined by electron diffraction was that of the water channel Aquaporin-0[13,105], which formed very thin double layered crystals. Although labelled as 2D crystals the crystals had two layers officially making them 3D crystals. Electron diffraction data was collected from thousands of crystals and data from more than 200 were integrated, merged and yielded a fully refined structure at atomic resolution at 1.9A in 2005[13]. In 2013 MicroED established robust streamlined methods for the collection of data using single 3D nanocrystals and in 2015 the first novel structure was determined by continuous rotation MicroED – that of the α-synuclein NACore (Figure 2.5a), the underlying pathology of Parkinson's disease[106]. α-synuclein NACore resisted structure determination for more than 10 years because large crystals could not be obtained. The microcrystals used for MicroED were invisible by light microscopy and not

suitable for X-ray diffraction studies. These tiny crystals, however, yielded an atomic-resolution 1.4 Å resolution structure of α-synuclein NACore by MicroED, enabling the observation of protons by cryoEM[65]. Another four prion peptides from Sup35 prion protein were also determined by MicroED at 1 Å resolution in 2016[93]. The high resolutions achieved in these studies allowed ab initio structure determination by direct methods (Discussed below).

Membrane proteins that are crystallized in the form of protein-detergent micelles, bicelles, or in lipid cubic phases, often have fewer crystal contact sites than soluble proteins. As such, membrane proteins are especially fragile and tend to grow small crystals that diffract poorly. In 2015, MicroED was successfully used to determine a 3.4 Å resolution structure of the membrane protein $Ca2^{+}$-ATPase using ultrathin 3D protein crystals[63] (Figure 2.5b). Importantly, the Coulomb potential maps that were generated by MicroED contained unique information about the charged states of amino acid residues, cofactors, and ligands. In 2018, the structure of the nonselective cation channel NaK (Figure 2.5b), was captured in two new conformations by MicroED[62]. Because MicroED can be used to gauge the charge-states of chemical moieties in structures, hydrated Na^{+} ions could be visualized at the entrance of the channel pore to reveal a new transient state in which a partially hydrated sodium ion occupied the entrance to the channel selectivity filter. Together, these studies demonstrated the capacity of MicroED to investigate dynamics and Coulomb potential in membrane proteins structures. In addition to membrane proteins, MicroED also successfully determined the structure of TGF-βm:TβRII[107]. This complex formed large yet poorly-ordered crystals without growth optimization, posing considerable challenges for X-ray crystallography. Breaking these

large, poorly-ordered into fragments produced well-diffracting microcrystals (Discussed above) that yielded diffraction data at atomic-resolution of the TGF-βm:TβRII complex[107] (Figure 2.5c).

MicroED in Drug Discovery

Structural characterization of proteins, as well as ligands and protein-ligand complexes is challenging, presenting a major bottleneck in rational drug design and

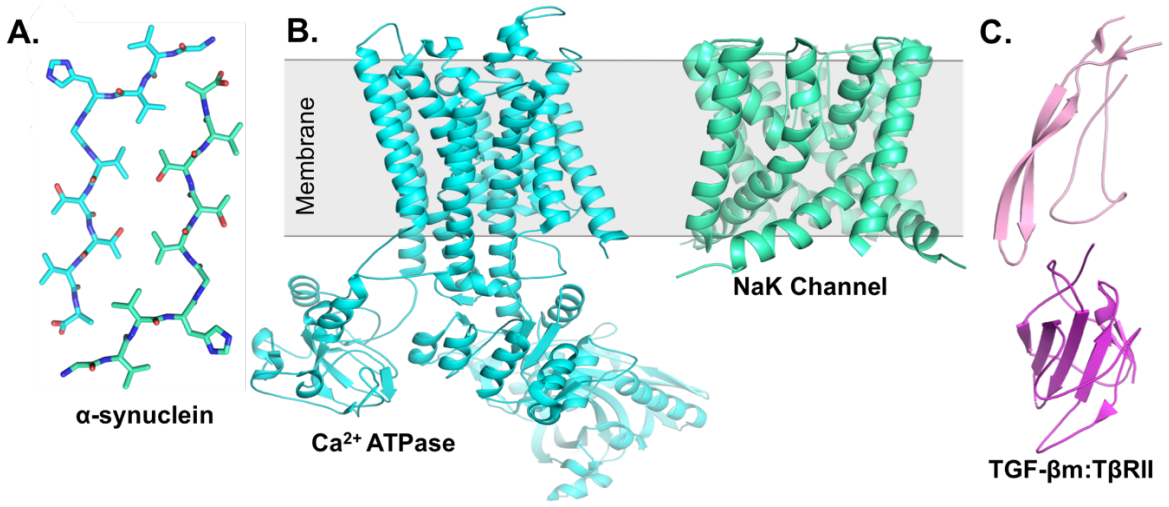

Figure 2.5. Examples of protein structures solved by MicroED that were challenging by other techniques. (A) Structure of α-synuclein core[65] (PDB 4ZNN). (B) MicroED structures of the membrane proteins rendered as cyan and green ribbon for Ca^{2+} ATPase (PDB 3J7T/U)[63] and NaK (PDB 6CPV)[62], repectively. (B) MircoED structure of the TGF-βm:TβRII protein-protein complex (PBD 5TY4)[71]. Protein rendered as pink and magenta ribbon for TGF-βm and TβRII, respectively.

development. MicroED has already contributed to drug discovery efforts through structure determination of protein-ligand complexes and supra-resolution (better than ~1 Å resolution) of bioactive small-molecules and natural-products. The very first drug discovery study using MicroED was that of homohexameric HIV GAG capsid protein in

complex with the viral maturation inhibitor bevirimat[108]. HIV Gag is a structural protein required for the budding of mature, infectious HIV viral particles from host cells[109] (Figure 2.6). Prior to the release of the viral particles and during viral maturation, the GAG proteins must be processed through proteolytic cleavage by HIV proteases at several sites[110]. Bevirimat is a small molecule ligand that binds directly to GAG to block the proteolytic processing of GAG[111]. The unprocessed and un-cleaved GAG protein results in the release of immature and noninfectious HIV particles[111]. Although bevirimat reached

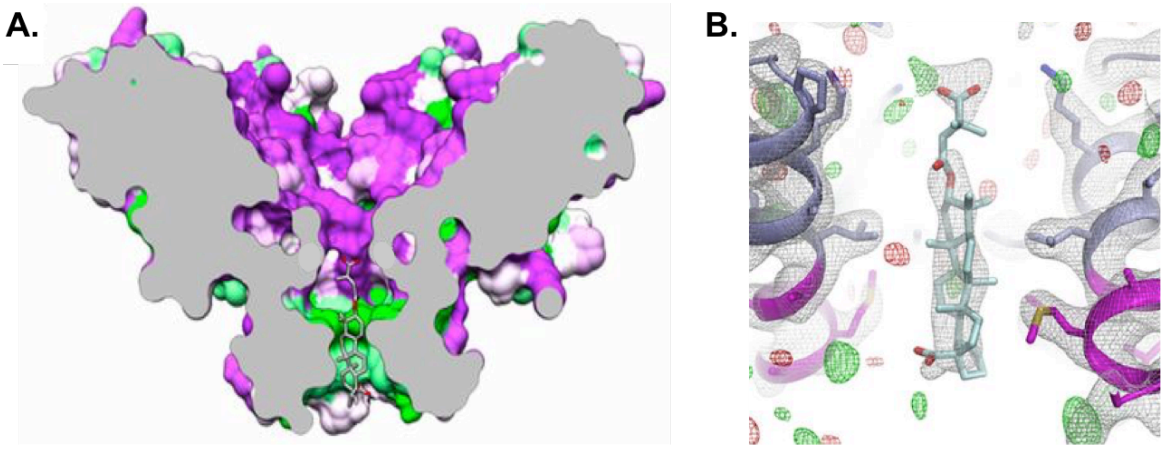

Figure 2.6. The structure of HIV GAG-bevirmat complex by MicroED. (A) Overall architecture of HIV GAG-bevirimat complex*[108]* (Reprint from reference 72). (B) Expanded view of the bevirimat binding site in the pore of HIV GAG*[108]* (Reprint from reference 72).

Phase IIb clinical trials, it was never fully developed into a marketed therapeutic because drug efficacy was low and many patients were unresponsive to the drug. At the time, the mechanism-of-action of bevirimat was unknown, abrogating efforts to reengineer this drug for its full therapeutic potential. To better understand the mechanism-of-action, the structure of HIV GAG in complex with bevirimat has been pursued by X-ray crystallography. Efforts to determine structure of GAG- bevirimat complex by both co-

crystallization and ligand soaking failed to produce crystals useful for X-ray diffraction. However, coupling time-resolved studies with MicroED allowed for structure determination of this elusive complex. To obtain MicroED data of the complex, bevirimat was added to GAG crystals on EM grids and immediately frozen in liquid ethane. This strategy allow for rapid diffusion of the ligand into the crystals (See section on Advantages and Application of Microcrystals for MicroED) while preserving the structural integrity of the GAG microcrystals[108] (Figure 2.6a). The HIV GAG-bevirimat MicroED structure revealed the binding-site of the drug, wedged in the 6-fold axis of the Gag hexamer where bevirimat acts as an allosteric inhibitor to prevent processing by proteases, trapping the immature form of HIV[108] (Figure 2.6b). This MicroED structure revealed the bevirimat mechanism of action, laying the groundwork for chemists to modify this ligand to tune the chemical properties of derivatives for altered bioactivity and future therapeutic application.

Although MicroED was originally developed for studying protein assemblies[16,28], it rapidly expnded as a powerful tool for structural characterization of small-molecules and natural-products. One of the first MicroED structures of a small-molecule drug was that of carbamazepine in 2016 to 1 Å resolution[112] (Figure 2.3). Importantly, the ab initio carbamazepine structure was the first to demonstrate that MicroED data can be obtained from samples prepared under anhydrous conditions, at room temperature, using continuous rotation, and with phases solved by direct methods. These new developments expanded the application of MicroED for structure determination of chemical compounds by circumventing the challenging and, often, laborious steps involved in the preparation of hydrated samples under cryogenic conditions[65]. In 2018, the structure of frozen and hydrated carbamezapine was determined using a break-through method for grid

preparation where powders were used for MicroED instead of grown crystals[68]. Under cryogenic conditions, the MicroED structure of carbamezapine was determined at a higher resolution compared with the room temperature study; and all hydrogen atoms were identified. Later in 2018, the structure of 12 different small moleules[57] as well as MBBF4[95], a methylene blue derivative with wide medical applications including its activity as a photo-activatable antimicrobial agent[113], was solved, further solidifying the capabilities of continuous rotation MicroED for small molecule structure determination[57] (Figure 2.3).

Unlike small-molecules, biosynthesized natural-products are typically larger, structurally dynamic, obtained in small quantities, and are difficult to crystallize, posing considerable challenges for X-ray studies. When natural-products do crystallize, these crystals are often too small and do not yield structures by X-ray diffraction[114,115]. Using the powder to structure pipeline[68], the structure of Brucine[116] (Figure 2.7), an alkaloid toxin with anticancer properties[116], was obtained by MicroED. The MicroED structure of brucine at 0.9 Å resolution allowed for definitive assignment of its chiral centers, key for understanding its toxicity and anticancer properties[57]. Relative to brucine, amino-acid derived natural-products called ribosomally synthesized and post-translationally modified peptides (RiPPs) are large, reaching several kilodaltons in size[117]. 3-thiaGlu[114] and thiostreptin are two examples of RiPP natural-products with structures determined by microED[118] (Figure 2.7). Thiostreptin is a RiPP antibiotic currently used in veterinary medicine[118]. Although, thiostreptin has been studied by NMR[114] and X-ray crystallography[119], the ease of its characterization by the powder to structure pipeline

speaks to the robustness of MicroED for structural characterization of large, flexible natural-products (Figure 2.7).

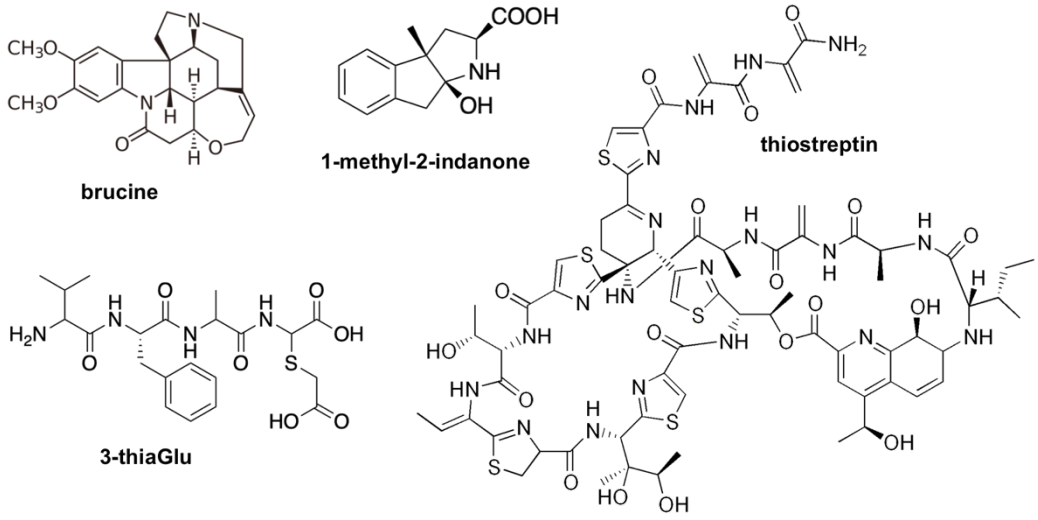

Figure 2.7. Examples of natural products with structures determined by MicroED.

Genome analysis of a plant pathogen *pseudomonas Syringae pv. maculicola* revealed a gene cluster encoding an unusual combination of biosynthetic enzymes that produces an unknown natural product[114]. Analysis of the biosynthetic enzymes revealed that, unlike other RiPPs, biosynthesis of the final natural product, later called 3-thiaGlu (Figure 2.7), involves the extension of the peptide in an ATP and amino acyl-tRNA-dependent manner, instead of the canonical scheme via the ribosome[114]. Completion of the biosynthesis of 3-thiaGlu also requires several additional steps including proteolysis of a terminal cysteine for installation of the glutamylated thiol group, a peptide modification that blocks jasmonate and ethylene signaling pathways[120]. Despite considerable effort, X-ray

crystallography failed to generate a structure of 3-thiaGlu. Using nano-crystals, MicroED readily provided a 0.9 Å resolution of the 3-thiaGlu peptide (PDB 6PO6)[114], allowing assignment of the chiral centers and providing further evidence for the proposed biosynthetic scheme and RiPP.

Like the difficulties encountered for 3-thiaGlu, the structures of non-canonical amino acids, 3-methyloxindole and 1-methyl-2-indanone (Figure 2.7) was only solved with the application of MicroED[115]. These non-canonical amino-acids are products from the condensation of 3-substituted oxindoles and L-serine, a reaction catalyzed by an engineered TrpB enzyme through directed evolution. The MicroED structure of the 3-methyloxindole and 1-methyl-2-indanone products from the engineered TrpB provided evidence of the newly installed *S*- configuration at the γ carbon, broadening the application of the enzyme for asymmetric catalysis. Here, the structures of these amino-acids by MicroED was used to inform biosynthetic pathways for green chemistry.

Thus far, MicroED still requires internal markers to determine the absolute configuration of chemical compounds[114,115]. For instance, internal markers such as a naturally occurring L amino acid is typically incorporated and used to deduce the relative configuration of all other centers in natural product and small molecule samples. Moving forward, the development of strategies for determining the absolute configurations of chemical compounds without the use of internal markers would widen the application of MicroED for drug discovery.

Overcoming Radiation Damage in MicroED

To date, radiation damage remains a major obstacle for all structural studies, leading to reduced resolution, poor map quality, and structural damage by bond breakage and even gross morphological decay[121]. For protein X-ray crystallography, the first study that addressed radiation damage dates back to 1962 when Blake & Phillips measured the loss in intensities of reflections as a function of time of X-ray exposure[122]. Several subsequent studies, including those by Hendrickson, moved the field from room temperature to cryogenic data collection to minimize the effects of radiation damage[123].

Radiation damage can be subcategorized into two forms: global and site-specific. Global radiation damage typically results from the disruption of the crystal lattice, leading to decreases in the intensities of diffraction patterns. This phenomenon can be detected during data-processing when changes in unit cell dimension[124] and increases in B-factors are observed[125]. On the other hand, site-specific radiation damage is not uniform, accumulates at certain chemical moieties, are not typically detected during data processing, and observable only during examination of the real-space map[126]. For both global and site-specific radiation damage, the degree of sample decay depends, among other things, on the composition of the sample, the surrounding solution, and is proportional to the amount of energy used[124–126].

Using proteinase K as a model system, both global and site-specific radiation damage have been examined in MicroED[69] (Figure 2.8). These studies illustrate that the increase in electron beam total dose (from 1.1 e^{-} $Å^{-2}$ to 3.1 e^{-} $Å^{-2}$) resulted in greater loss of detectable reflections in higher resolution shells of MicroED data[69] (Figure 2.8a). The

higher exposures during MicroED experiments also resulted in increases in unit cell dimensions and B-factors, both indicators of global radiation damage (Figure 2.8b).

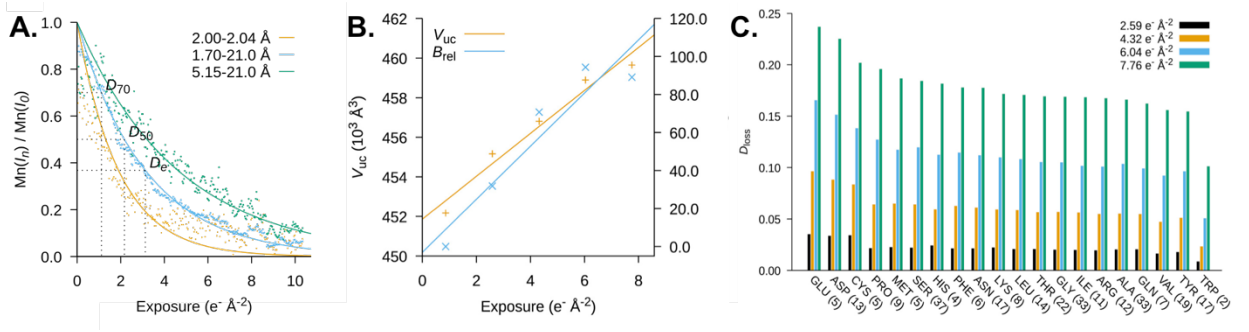

Figure 2.8. Radiation damage in MicroED. (A) Proteinase K recorded at an exposure rates. (B) Volume and B-factor were averaged across all the crystals at each exposure for proteinase K. (C) Density loss in arbitrary units for all the amino acids, ligands, and ions present in the refined models of proteinase K.

Similarly, higher exposures also led to greater site-specific radiation damage that accumulated on specific amino-acids including glutamatic acid, aspartic acid, and cysteines suggesting that radiation damage in MicroED follows similar trends to radiation damage in X-ray crystallography (Figure 2.8c). To curb the effects of radiation damage, samples are often vitrified[127]. However, even the combination of vitrification, continuous rotation data collection, and exposure to extremely low doses of electrons (0.01 e−/Å^2/s) during MicroED experiments, samples can still suffer from radiation damage[69]. However, recent studies suggest that by using a faster and more sensitive camera, the direct electron detector Falcon 3, radiation damage can be outrun[114,115,128] (Figure 2.9).

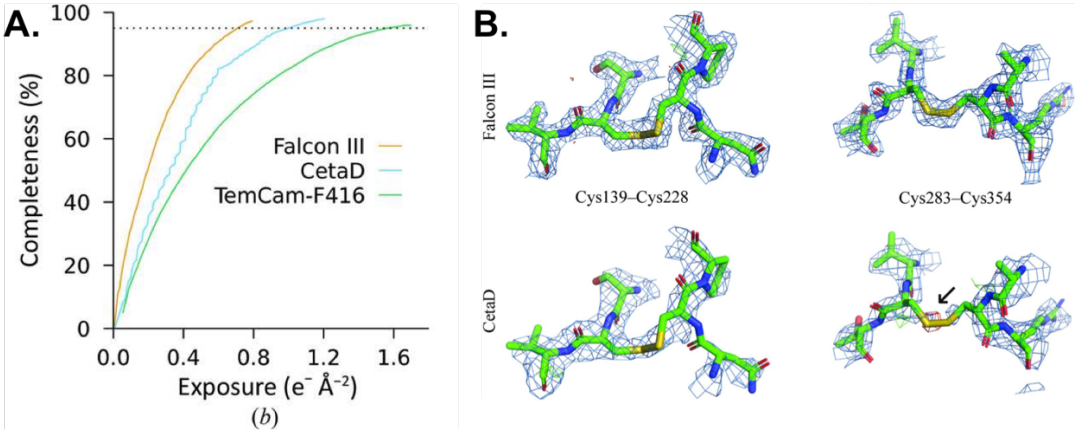

Figure 2.9. Expanding the use of direct electron detectors and mitigating radiation damage in MicroED. (A) The exposure-dependency of the completeness of proteinase K. The dotted horizontal line marks 95% completeness. (B) The density around the two disulfide bonds for the considered cameras for proteinase K.

Solving the Phase Problem in MicroED

As with X-ray diffraction, phases are lost in MicroED experiments, referred to in both techniques as "the phase problem"[129]. For both the MicroED and X-ray crystallography, the phases can be recovered by molecular replacement and ab initio direct methods[57,65]. While molecular replacement is dependent on topological similarities between the search models and the structures to be determined[130], direct methods require crystals that diffract to fairly high-resolution at ~1 Å or better[131]. The PDB contains 150,000 deposited structures, many of which share conserved folds. Due to the conservation of folds across families of proteins, molecular replacement is currently used to calculate phases of roughly 90% of structures deposited to the PDB.

For MicroED, several methods have been successful in solving the phase problem including the use of image data[86–89], ARCIMBOLDO [90], and radiation induced damage[91] for phasing (RIP). Traditionally, during RIP, a single dataset from the sample crystal is

split into two[132]. The first part of the dataset consists of earlier frames that contain less accumulated radiation damage. The second set of frames is comprised of data collected after the first set, which, as a result, contain higher accumulation of radiation damage[132]. Like isomorphous replacement[133] and anomalous dispersion[134], the two halved sub-datasets are subtracted from one another to generate a difference dataset[132]. The difference dataset is then used to identify focal points of specific radiation damaged sites, such as the hydrolysis of disulfide bonds or ionized metals. Because exposure to electron beams, even at low dosages, can lead to radiation damage during diffraction studies[69], RIP is a promising strategy for obtaining experimental phases for MicroED experiments.

To test if experimental phasing using RIP is a viable strategy for determining novel MicroED structures, a previously solved structure of the prion hepta-peptide corresponding the GSNQNNF sequence was used as a model system[91]. To maximize completeness, eleven crystals of the hepta-peptide were used to collect two datasets one with the exposure of 0.17 e^{-} $Å^{-2}$ and the second at 0.5 e^{-} $Å^{-2}$. The structure amplitudes of the low-dose were subtracted from the high-dose dataset to calculate a difference dataset. The difference dataset was used to calculate a difference Patterson map to identify the location of radiation damage resulting from higher dosages of electron[91]. This strategy identified a single solution corresponding to a zinc atom (Figure 2.10a). The zinc position was then used to calculate the initial phases to generate a density map for model building of the peptide structure[91] (Figure 2.10b-d).

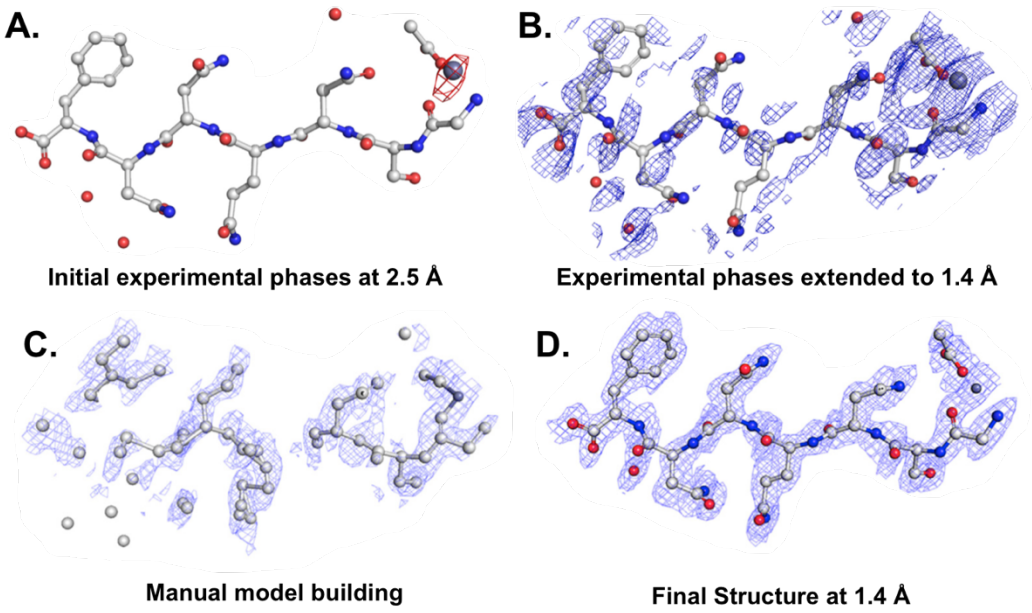

Figure 2.10. Identification of heavy metal site and model building. (A) Fourier difference maps between the damaged and undamaged structure of GSNQNNF using the phases of 6CLI at 2.5-A° resolution contoured at 3s level. (B) The map using the initial phases extended to 1.4-A° resolution. (C) Density maps at 1.0s contour for intermediate building steps. (D) The final structure. (All panels are reprint from reference [91]).

In conclusion, MicroED is a relatively young field of study within cryoEM. In less than a decade since the field started[135], more than 100 structures have been determined for proteins, protein complexes, natural products, peptides and small organic and inorganic molecules. As the method continues to be improved with better hardware, automation and software, the usefulness and broad applicability of MicroED will only increase.

References

1. Dubochet J, Booyl FP, Freeman R, Jones A V., Walter CA. Low temperature electron microscopy. *Ann Rev Biophys*. 1981;10. doi:10.1038/267312a0

2. Taylor KA, Glaeser RM. Electron Diffraction of Frozen, Hydrated Protein Crystals. *Science*. Published online 1974.

3. Wang L, Sigworth FJ. Cryo-EM and single particles. *Physiology*. 2006;21(1):13-18. doi:10.1152/physiol.00045.2005

4. Bai XC, Fernandez IS, McMullan G, Scheres SHW. Ribosome structures to near-atomic resolution from thirty thousand cryo-EM particles. *eLife*. 2013;2013(2):2-13. doi:10.7554/eLife.00461

5. Herzik MA, Wu M, Lander GC. Achieving better-than-3-Å resolution by single-particle cryo-EM at 200 keV. *Nature Methods*. 2017;14(11):1075-1078. doi:10.1038/nmeth.4461

6. Myasnikov A, Zheng S, Bulkley D, Cheng Y, Agard D. K3 - A First Look at The New Direct Electron Detection Camera from Gatan Company. *Microscopy and Microanalysis*. 2018;24(S1):890-891. doi:10.1017/s1431927618004944

7. Punjani A, Rubinstein JL, Fleet DJ, Brubaker MA. CryoSPARC: Algorithms for rapid unsupervised cryo-EM structure determination. *Nature Methods*. 2017;14(3):290-296. doi:10.1038/nmeth.4169

8. Tegunov D, Cramer P. Real-time cryo-electron microscopy data preprocessing with Warp. *Nature Methods*. 2019;16(11):1146-1152. doi:10.1038/s41592-019-0580-y

9. Wagner T, Merino F, Stabrin M, et al. SPHIRE-crYOLO is a fast and accurate fully automated particle picker for cryo-EM. *Communications Biology*. 2019;2(1):1-13. doi:10.1038/s42003-019-0437-z

10. Zivanov J, Nakane T, Forsberg BO, et al. New tools for automated high-resolution cryo-EM structure determination in RELION-3. *eLife*. 2018;7:1-22. doi:10.7554/eLife.42166

11. Thompson RF, Walker M, Siebert CA, Muench SP, Ranson NA. An introduction to sample preparation and imaging by cryo-electron microscopy for structural biology. *Methods*. 2016;100:3-15. doi:10.1016/j.ymeth.2016.02.017

12. McMullan G, Faruqi AR, Henderson R. *Direct Electron Detectors*. Vol 579. 1st ed. Elsevier Inc.; 2016. doi:10.1016/bs.mie.2016.05.056

13. Gonen T, Cheng Y, Sliz P, et al. Lipid-protein interactions in double-layered two-dimensional AQP0 crystals. *Nature*. 2005;438(7068):633-638. doi:10.1038/nature04321

14. Subramanian R, Mayor S, Vinothkumar KR. The resolution revolution reaches India. *Biophysical Reviews*. 2019;11(4):513-514. doi:10.1007/s12551-019-00558-7

15. Susannah S, Ando N. X-rays in the Cryo-EM Era: Structural Biology's Dynamic Future. *Biochemistry*. 2018;57(3):277-285. doi:10.1002/cncr.27633.Percutaneous

16. Shi D, Nannenga BL, Iadanza MG, Gonen T. Three-dimensional electron crystallography of protein microcrystals. *eLife*. 2013;2:1-17. doi:10.7554/elife.01345

17. DUBOCHET J, ADRIAN M, CHANG JJ, et al. Cryo-electron microscopy of vitrified specimens. *Quarterly Reviews of Biophysics*. 1988;21(2):129-228. doi:10.1017/S0033583500004297

18. Taylor DW, Zhu Y, Staals RHJ, et al. Structures of the CRISPR-Cmr complex reveal mode ofRNA target positioning. *Science*. 2015;348(6234):581-586. doi:10.1126/science.aaa4535

19. Cheng Y. Single-particle cryo-EM-How did it get here and where will it go. *Science*. 2018;361(6405):876-880. doi:10.1126/science.aat4346

20. Murphy GE, Jensen GJ. Electron cryotomography of the E. coli pyruvate and 2-oxoglutarate dehydrogenase complexes. *Structure*. 2005;13(12):1765-1773. doi:10.1016/j.str.2005.08.016

21. Komeili A, Li Z, Newman DK, Jensen GJ. Magnetosomes Are Cell Membrane Invaginations Organized by the Actin-Like Protein MamK. *Science*. 2006;311(January):242-246. doi:10.7551/mitpress/8876.003.0036

22. Oikonomou CM, Jensen GJ. Cellular Electron Cryotomography: Toward Structural Biology In Situ. *Annual Review of Biochemistry*. 2017;86(1):873-896. doi:10.1146/annurev-biochem-061516-044741

23. Henderson R, Baldwin JM, Ceska TA, Zemlin F, Beckmann E, Downing KH. Model for the structure of bacteriorhodopsin based on high-resolution electron cryo-microscopy. *Journal of Molecular Biology*. 1990;213(4):899-929. doi:10.1016/S0022-2836(05)80271-2

24. Schmidt-Krey I. Electron crystallography of membrane proteins: Two-dimensional crystallization and screening by electron microscopy. *Methods*. 2007;41(4):417-426. doi:10.1016/j.ymeth.2006.07.011

25. Mahamid J, Pfeffer S, Schaffer M, et al. Visualizing the molecular sociology at the HeLa cell nuclear periphery. *Science*. 2016;351(6276):969-972. doi:10.1126/science.aad8857

26. Wrapp D, Wang N, Corbett KS, et al. Cryo-EM structure of the 2019-nCoV spike in the prefusion conformation. *Science*. 2020;367(6483):1260-1263. doi:10.1126/science.aax0902

27. Wisedchaisri G, Reichow SL, Gonen T. Advances in structural and functional analysis of membrane proteins by electron crystallography. *Structure*. 2011;29(10):1381-1393. doi:10.1016/j.biotechadv.2011.08.021.Secreted

28. Nannenga BL, Shi D, Hattne J, Reyes FE, Gonen T. Structure of catalase determined by MicroED. *eLife*. 2014;3:e03600. doi:10.7554/eLife.03600

29. De Rosier DJ, Klug A. Reconstruction of three dimensional fiber structures from orthogonal projections. *Nature*. 1968;217:130-134.

30. Heel M Van. Use of multivariate statistics in analysing the images of biological macromolecules. *Ultramicroscopy*. 1981;6:187-194.

31. Frank J. The role of multivariate image analysis in solving the architecture of the limulus polyphemus hemocyanin molecule. *Ultramicroscopy*. 1984;13(1-2):153-164. doi:10.1016/0304-3991(84)90065-2

32. Frank J, Wagenknecht T, McEwen BF, Marko M, Hsieh CE, Mannella CA. Three-dimensional imaging of biological complexity. *J struct Biol*. Published online 2002.

33. Scheres SHW, Gao H, Valle M, et al. Disentangling conformational states of macromolecules in 3D-EM through likelihood optimization. *Nature Methods*. 2007;4(1):27-29. doi:10.1038/nmeth992

34. Frank J, Goldfarb W, Eisenberg D, Baker TS. Reconstruction of glutamine synthetase using computer averaging. *Ultramicroscopy*. 1978;3(C):283-290. doi:10.1016/S0304-3991(78)80038-2

35. Frank J. Intermediate states during mRNA-tRNA translocation. *Current Opinion in Structural Biology*. 2012;22(6):778-785. doi:10.1016/j.sbi.2012.08.001

36. Henderson R. The Potential and Limitations of Neutrons, Electrons and X-Rays for Atomic Resolution Microscopy of Unstained Biological Molecules. *Quarterly Reviews of Biophysics*. 1995;28(2):171-193. doi:10.1017/S003358350000305X

37. Herzik MA, Wu M, Lander GC. High-resolution structure determination of sub-100 kDa complexes using conventional cryo-EM. *Nature Communications*. 2019;10(1):1-9. doi:10.1038/s41467-019-08991-8

38. Lu C, Reedy M, Erickson HP. Straight and curved conformations of FtsZ are regulated by GTP hydrolysis. *Journal of Bacteriology*. 2000;182(1):164-170. doi:10.1128/JB.182.1.164-170.2000

39. Li Z, Trimble MJ, Brun Y V., Jensen GJ. The structure of FtsZ filaments in vivo suggests a force-generating role in cell division. *EMBO Journal*. 2007;26(22):4694-4708. doi:10.1038/sj.emboj.7601895

40. Komeili A, Li Z, Newman DK, Jensen GJ. Magnetosomes Are Cell Membrane Invaginations Organized by the Actin-Like Protein MamK. *Science*. 2006;311(January):242-246. doi:10.7551/mitpress/8053.003.0075

41. Medalia O, Weber I, Frangakis AS, Nicastro D, Gerisch G, Baumeister W. Macromolecular architecture in eukaryotic cells visualized by cryoelectron tomography. *Science*. 2002;298(5596):1209-1213. doi:10.1126/science.1076184

42. Jurgen A.W. Heymanna, Haylesb M, Gestmannb I, Giannuzzic LA, Lichb B, Subramaniam S. Site-specific 3D imaging of cells and tissues with a dual beam microscope. *J struct Biol*. 2006;155(1):63-73. doi:10.1038/jid.2014.371

43. Hsieh C, Schmelzer T, Kishchenko G, Wagenknecht T, Marko M. Practical workflow for cryo focused-ion-beam milling of tissues and cells for cryo-TEM tomography. *J struct Biol*. Published online 2014. doi:10.1038/jid.2014.371

44. Zachs T, Schertel A, Medeiros J, et al. Fully automated, sequential focused ion beam milling for cryo-electron tomography. *eLife*. 2020;9:1-14. doi:10.7554/eLife.52286

45. Hoppe W, Gassmann J, Hunsmann N, Schramm H, Sturn M. Three-dimensional reconstruction of individual negatively stained yeast fatty-acid synthetase molecules from tilt series in the electron microscope. *Physiol Chem*. 1974;355.

46. Okumura T, Shoji M, Hisada A, et al. Electron tomography of whole cultured cells using novel transmission electron imaging technique. *Micron*. 2018;104(July 2017):21-25. doi:10.1016/j.micron.2017.10.006

47. Irobalieva RN, Martins B, Medalia O. Cellular structural biology as revealed by cryo-electron tomography. *Journal of Cell Science*. 2016;129(3):469-476. doi:10.1242/jcs.171967

48. Doerr A. Cryo-electron tomography. *Nature Methods*. 2016;14(1):34. doi:10.1038/nmeth.4115

49. Henderson R, Unwin PNT. Three-dimensional model of purple membrane obtained by electron microscopy. *Nature*. 1975;257:28-32.

50. Mohraz M, Simpson M V., Smith PR. The three-dimensional structure of the Na,K-ATPase from electron microscopy. *The Journal of cell biology*. 1987;105(1):1-8. doi:10.1083/jcb.105.1.1

51. Hasler L, Heymann JB, Engel A, Kistler J, Walz T. 2D crystallization of membrane proteins: Rationales and examples. *Journal of Structural Biology*. 1998;121(2):162-171. doi:10.1006/jsbi.1998.3960

52. Lévy D, Mosser G, Lambert O, Moeck GS, Bald D, Rigaud JL. Two-dimensional crystallization on lipid layer: A successful approach for membrane proteins. *Journal of Structural Biology*. 1999;127(1):44-52. doi:10.1006/jsbi.1999.4155

53. Miyazawa A, Fujiyoshi Y, Unwin N. Structure and gating mechanism of the acetylcholine receptor pore. *Nature*. 2003;423(6943):949-955. doi:10.1038/nature01748

54. Unger VM, Kumar NM, Gilula NB, Yeager M. Expression, two-dimensional crystallization, and electron cryo- crystallography of recombinant gap junction membrane channels. *Journal of Structural Biology*. 1999;128(1):98-105. doi:10.1006/jsbi.1999.4184

55. Grigorieff N, Ceska TA, Downing KH, Baldwin JM, Henderson R. Electron-crystallographic refinement of the structure of bacteriorhodopsin. *Journal of Molecular Biology*. 1996;259(3):393-421. doi:10.1006/jmbi.1996.0328

56. Kiihlbrandt W, Neng D, Fujiyoshi Y. Atomic model of plant light-harvesting complex by electron crystallography. 1994;367(February):614-621.

57. Jones CG, Martynowycz MW, Hattne J, et al. The CryoEM Method MicroED as a Powerful Tool for Small Molecule Structure Determination. *ACS Central Science*. 2018;4(11):1587-1592. doi:10.1021/acscentsci.8b00760

58. Nannenga BL, Shi D, Leslie AGW, Gonen T. High-resolution structure determination by continuous rotation data collection in MicroED. *Nature Methods*. 2015;11(9):927-930. doi:10.1038/nmeth.3043.High-resolution

59. Martynowycz MW, Gonen T. From electron crystallography of 2D crystals to MicroED of 3D crystals. *Current Opinion in Colloid and Interface Science*. 2018;34:9-16. doi:10.1016/j.cocis.2018.01.010

60. Hattne J, Reyes FE, Nannenga BL, et al. MicroED data collection and processing. *Acta Crystallographica Section A: Foundations and Advances*. 2015;71:353-360. doi:10.1107/S2053273315010669

61. Hirai T, Mitsuoka K, Kidera A, Fujiyoshi Y. Simulation of charge effects on density maps obtained by high-resolution electron crystallography. *Journal of Electron Microscopy*. 2007;56(4):131-140. doi:10.1093/jmicro/dfm019

62. Liu S, Gonen T. MicroED structure of the NaK ion channel reveals a Na+ partition process into the selectivity filter. *Communications Biology*. 2018;1(1):1-6. doi:10.1038/s42003-018-0040-8

63. Yonekura K, Kato K, Ogasawara M, Tomita M, Toyoshima C. Electron crystallography of ultrathin 3D protein crystals: Atomic model with charges. *Proceedings of the National Academy of Sciences of the United States of America*. 2015;112(11):3368-3373. doi:10.1073/pnas.1500724112

64. Henderson R. The Potential and Limitations of Neutrons, Electrons and X-Rays for Atomic Resolution Microscopy of Unstained Biological Molecules. *Quarterly Reviews of Biophysics*. 1995;28(2):171-193. doi:10.1017/S003358350000305X

65. Rodriguez JA, Ivanova MI, Sawaya MR, et al. Structure of the toxic core of α-synuclein from invisible crystals. *Nature*. 2015;525(7570):486-490. doi:10.1038/nature15368.Structure

66. Kissick DJ, Wanapun D, Simpson GJ. Second-Order Nonlinear Optical Imaging of Chiral Crystals. *Annu Rev Anal Chem*. Published online 2011. doi:10.1038/jid.2014.371

67. Stevenson HP, Makhov AM, Calero M, et al. Use of transmission electron microscopy to identify nanocrystals of challenging protein targets. *Proceedings of the National Academy of Sciences of the United States of America*. 2014;111(23):8470-8475. doi:10.1073/pnas.1400240111

68. Gallagher-jones M, Glynn C, Boyer DR, et al. Sub-ångstrom cryo-EM structure of a prion protofibril reveals a polar clasp. *Nat Struct Mol Biol*. 2018;25(2):131-134. doi:10.1038/s41594-017-0018-0.Sub-

69. Hattne J, Shi D, Glynn C, et al. Analysis of Global and Site-Specific Radiation Damage in Cryo-EM. *Structure*. 2018;26(5):759-766.e4. doi:10.1016/j.str.2018.03.021

70. Jones CG, Asay M, Kim LJ, et al. Characterization of Reactive Organometallic Species via MicroED. *ACS Central Science*. 2019;5(9):1507-1513. doi:10.1021/acscentsci.9b00403

71. De La Cruz MJ, Hattne J, Shi D, et al. Atomic-resolution structures from fragmented protein crystals with the cryoEMEM method MicroED. *Nature Methods*. 2017;14(4):399-402. doi:10.1038/nmeth.4178

72. Martynowycz MW, Zhao W, Hattne J, et al. Collection of Continuous Rotation MicroED Data from Ion Beam- Milled Crystals of Any Size. *Structure*. 2019;27(3):545-548. doi:10.1016/j.str.2018.12.003.Collection

73. Duyvesteyn HME, Kotecha A, Ginn HM, et al. Machining protein microcrystals for structure determination by electron diffraction. *Proceedings of the National Academy of Sciences of the United States of America*. 2018;115(38):9569-9573. doi:10.1073/pnas.1809978115

74. Martynowycz MW, Zhao W, Hattne J, Jensen GJ, Gonen T. Qualitative Analyses of Polishing and Precoating FIB Milled Crystals for MicroED. *Structure*. 2019;27(10):1594-1600.e2. doi:10.1016/j.str.2019.07.004

75. Zhou H, Luo Z, Li X. Using focus ion beam to prepare crystal lamella for electron diffraction. *Journal of Structural Biology*. 2019;205(3):59-64. doi:10.1016/j.jsb.2019.02.004

76. Nannenga BL, Shi D, Leslie AGW, Gonen T. High-resolution structure determination by continuous-rotation data collection in MicroEDED. *Nature Methods*. 2014;11(9):927-930. doi:10.1038/nmeth.3043

77. de la Cruz MJ, Martynowycz MW, Hattne J, Gonen T. MicroED data collection with SerialEM. *Ultramicroscopy*. 2019;201(January):77-80. doi:10.1016/j.ultramic.2019.03.009

78. Martynowycz M, Glynn C, Miao J, et al. MicroED Structures from Micrometer Thick Protein Crystals. *bioRxiv*. Published online 2017:152504. doi:10.1101/152504

79. Shi D, Nannenga BL, de la Cruz MJ, et al. The collection of MicroED data for macromolecular crystallography. *Nat Protoc*. 2016;11(5):895-904. doi:10.1038/nprot.2016.46

80. Minor ZO and W. Processing of X-Ray Diffraction Data Collected in Oscillation Mode. *Methods in enzymology*. 1997;276(January 1993):306-315.

81. Kabsch W, T. BA, K. D, et al. *XDS*. *Acta Crystallographica Section D Biological Crystallography*. 2010;66(2):125-132. doi:10.1107/S0907444909047337

82. Battye TGG, Kontogiannis L, Johnson O, Powell HR, Leslie AGW. iMOSFLM: A new graphical interface for diffraction-image processing with MOSFLM. *Acta Crystallographica Section D: Biological Crystallography*. 2011;67(4):271-281. doi:10.1107/S0907444910048675

83. Parkhurst JM, Winter G, Waterman DG, et al. Robust background modelling in DIALS. *Journal of Applied Crystallography*. 2016;49(6):1912-1921. doi:10.1107/S1600576716013595

84. Sheldrick GM. SHELXT - Integrated space-group and crystal-structure determination. *Acta Crystallographica Section A: Foundations of Crystallography*. 2015;71(1):3-8. doi:10.1107/S2053273314026370

85. McCoy AJ, Grosse-Kunstleve RW, Adams PD, Winn MD, Storoni LC, Read RJ. Phaser crystallographic software. *Journal of Applied Crystallography*. 2007;40(4):658-674. doi:10.1107/S0021889807021206

86. Kamegawa A, Hiroaki Y, Tani K, Fujiyoshi Y. Two-dimensional crystal structure of aquaporin-4 bound to the inhibitor acetazolamide. *Microscopy (Oxford, England)*. 2016;65(2):177-184. doi:10.1093/jmicro/dfv368

87. Oshima A. Structure of an innexin gap junction channel and cryo-EM sample preparation. *Microscopy*. 2017;66(6):371-379. doi:10.1093/jmicro/dfx035

88. Nederlof I, Li YW, Van Heel M, Abrahams JP. Imaging protein three-dimensional nanocrystals with cryo-EM. *Acta Crystallographica Section D: Biological Crystallography*. 2013;69(5):852-859. doi:10.1107/S0907444913002734

89. van Genderen E, Li YW, Nederlof I, Abrahams JP. Lattice filter for processing image data of three-dimensional protein nanocrystals. *International Journal of Dermatology*. 2018;57(1):34-39. doi:10.1107/S205979831502149X

90. Rodríguez DD, Grosse C, Himmel S, et al. Crystallographic ab initio protein structure solution below atomic resolution. *Nature Methods*. 2009;6(9):651-653. doi:10.1038/nmeth.1365

91. Martynowycz MW, Hattne J, Gonen T. Experimental Phasing of MicroED Data Using Radiation Damage. *Structure*. 2020;28(4):458-464.e2. doi:10.1016/j.str.2020.01.008

92. Kupitz C, Grotjohann I, Conrad CE, Roy-Chowdhury S, Fromme R, Fromme P. Microcrystallization techniques for serial femtosecond crystallography using photosystem II from Thermosynechococcus elongatus as a model system. *Philosophical Transactions of the Royal Society B: Biological Sciences*. 2014;369(1647). doi:10.1098/rstb.2013.0316

93. Sawaya MR, Rodriguez J, Cascio D, et al. Ab initio structure determination from prion nanocrystals at atomic resolution by MicroED. *Proceedings of the National Academy of Sciences of the United States of America*. 2016;113(40):11232-11236. doi:10.1073/pnas.1606287113

94. Kunde T, Schmidt BM. Microcrystal Electron Diffraction (MicroED) for Small-Molecule Structure Determination. *Angewandte Chemie - International Edition*. 2019;58(3):666-668. doi:10.1002/anie.201813215

95. Gruene T, Wennmacher JTC, Zaubitzer C, et al. Rapid Structure Determination of Microcrystalline Molecular Compounds Using Electron Diffraction. *Angewandte Chemie - International Edition*. 2018;57(50):16313-16317. doi:10.1002/anie.201811318

96. van Genderen E, Clabbers MTB, Das PP, et al. Ab initio structure determination of nanocrystals of organic pharmaceutical compounds by electron diffraction at room

temperature using a Timepix quantum area direct electron detector (Acta Cryst., (2018), A72, (236–242), 10.1107/S2053273315022500). *Acta Crystallographica Section A: Foundations and Advances*. 2018;74(6):709. doi:10.1107/S2053273318014079

97. Matsufuji H, Ichiyama T, Isumi H, Furukawa S. Low-dose carbamazepine therapy for benign infantile convulsions. *Brain and Development*. 2005;27(8):554-557. doi:10.1016/j.braindev.2005.01.005

98. Hirschfeld RMA, Kasper S. A review of the evidence for carbamazepine and oxcarbazepine in the treatment of bipolar disorder. *International Journal of Neuropsychopharmacology*. 2004;7(4):507-522. doi:10.1017/S1461145704004651

99. Koytchev R, Vlahov V, Bacratcheva N, et al. Evaluation of the efficacy of a combined formulation (Grippostad®-C) in the therapy of symptoms of common cold: A randomized, double-blind, multicenter trial. *International Journal of Clinical Pharmacology and Therapeutics*. 2003;41(3):114-125. doi:10.5414/CPP41114

100. Li X, Zhang S, Zhang J, Sun F. In situ protein micro-crystal fabrication by cryo-FIB for electron diffraction. *Biophysics Reports*. 2018;4(6):339-347. doi:10.1007/s41048-018-0075-x

101. Zhou H, Luo Z, Li X. Using focus ion beam to prepare crystal lamella for electron diffraction. *Journal of Structural Biology*. 2019;205(3):59-64. doi:10.1016/j.jsb.2019.02.004

102. Beck T, Da Cunha CE, Sheldrick GM. How to get the magic triangle and the MAD triangle into your protein crystal. *Acta Crystallographica Section F: Structural Biology and Crystallization Communications*. 2009;65(10):1068-1070. doi:10.1107/S1744309109036884

103. Geremia S, Campagnolo M, Demitri N, Johnson LN. Simulation of diffusion time of small molecules in protein crystals. *Structure*. 2006;14(3):393-400. doi:10.1016/j.str.2005.12.007

104. Martynowycz MW, Gonen T. Efficient , high-throughput ligand incorporation into protein microcrystals by on-grid soaking. Published online 2020:1-27.

105. Gonen T, Sliz P, Kistler J, Cheng Y, Walz T. Aquaporin-0 membrane junctions reveal the structure of a closed water pore. *Nature*. 2004;429(6988):193-197. doi:10.1038/nature02503

106. Auluck PK, Caraveo G, Lindquist S. α-synuclein: Membrane interactions and toxicity in parkinson's disease. *Annual Review of Cell and Developmental Biology*. 2010;26:211-233. doi:10.1146/annurev.cellbio.042308.113313

107. Morikawa M, Derynck R, Miyazono K. TGF- β and the TGF-β family: Context-dependent roles in cell and tissue physiology. *Cold Spring Harbor Perspectives in Biology*. 2016;8(5). doi:10.1101/cshperspect.a021873

108. Purdy MD, Shi D, Chrustowicz J, Hattne J, Gonen T, Yeager M. MicroED structures of HIV-1 Gag CTD-SP1 reveal binding interactions with the maturation inhibitor bevirimat. *Proceedings of the National Academy of Sciences of the United States of America*. 2018;115(52):13258-13263. doi:10.1073/pnas.1806806115

109. Sundquist WI, Kra H georg. HIV-1 Assembly, Budding, and Maturation. Published online 2012:1-24.

110. Lee SK, Potempa M, Swanstrom R. The choreography of HIV-1 proteolytic processing and virion assembly. *Journal of Biological Chemistry*. 2012;287(49):40867-40874. doi:10.1074/jbc.R112.399444

111. Martin DE, Salzwedel K, Allaway GP. Bevirimat: A novel maturation inhibitor for the treatment of HIV-1 infection. *Antiviral Chemistry and Chemotherapy*. 2008;19(3):107-113. doi:10.1177/095632020801900301

112. Van Genderen E, Clabbers MTB, Das PP, et al. Ab initio structure determination of nanocrystals of organic pharmaceutical compounds by electron diffraction at room temperature using a Timepix quantum area direct electron detector. *Acta Crystallographica Section A: Foundations and Advances*. 2016;72:236-242. doi:10.1107/S2053273315022500

113. Wainwright M. Methylene blue derivatives - Suitable photoantimicrobials for blood product disinfection? *International Journal of Antimicrobial Agents*. 2000;16(4):381-394. doi:10.1016/S0924-8579(00)00207-7

114. Ting CP, Funk MA, Halaby SL, Zhang Z, Gonen T, Van Der Donk WA. Use of a scaffold peptide in the biosynthesis of amino acid-derived natural products. *Science*. 2019;365(6450):280-284. doi:10.1126/science.aau6232

115. Dick M, Sarai NS, Martynowycz MW, Gonen T, Arnold FH. Tailoring Tryptophan Synthase TrpB for Selective Quaternary Carbon Bond Formation. *Journal of the American Chemical Society*. 2019;141(50):19817-19822. doi:10.1021/jacs.9b09864

116. Qin J, Yang L, Sheng X, et al. Antitumor effects of brucine immuno-nanoparticles on hepatocellular carcinoma in vivo. *Oncology Letters*. 2018;15(5):6137-6146. doi:10.3892/ol.2018.8168

117. Paul G. Arnisona, Mervyn J. Bibbb, Gabriele Bierbaumc, Albert A. Bowersd, Tim S. Bugnie, Grzegorz Bulajf, Julio A. Camarerog, Dominic J. Campopianoh, Gregory L. Challisi, Jon Clardyj, Paul D. Cotterk, David J. Craikl, Michael Dawsonm, Elke Dittmannn, Stef RPR, 15. NPRepA manuscript; available in P 2014 M, 41 NPAMNPAMNPAMA et al. P, et al. Ribosomally synthesized and post-translationally modified peptide natural products: overview and recommendations for a universal nomenclature. *Natural Product Reports*. 2014;30(1):108-160. doi:10.1039/c2np20085f.Ribosomally

118. Kutscher AH, Seguin L, Zegarelli E V., Piro JD. Antimicrobial activity of thiostrepton: tube dilution studies. *Journal of the American Dental Association (1939)*. 1959;59(4):715-720. doi:10.14219/jada.archive.1959.0207

119. Anderson B, Hodgkin DC, Viswamitra MA. The structure of thiostrepton. *Nature*. 1970;225(5229):233-235. doi:10.1038/225233a0

120. Arrebola E, Cazorla FM, Perez-García A, de Vicente A. Chemical and metabolic aspects of antimetabolite toxins produced by Pseudomonas syringae pathovars. *Toxins*. 2011;3(9):1089-1110. doi:10.3390/toxins3091089

121. Garman EF, Weik M. X-ray radiation damage to biological macromolecules: Further insights. *Journal of Synchrotron Radiation*. 2017;24(1):1-6. doi:10.1107/S160057751602018X

122. Blake CCF, Phillips DC. Biological Effects of Ionizing Radiation at the Molecular Level. *Vienna: International Atomic Energy Agency*. Published online 1962:183-191.

123. Hendrickson WA. Radiation damage in protein crystallography. *Journal of Molecular Biology*. 1976;106(3):889-893. doi:10.1016/0022-2836(76)90271-0

124. Ravelli RBG, Theveneau P, McSweeney S, Caffrey M. Unit-cell volume change as a metric of radiation damage in crystals of macromolecules. *Journal of Synchrotron Radiation*. 2002;9(6):355-360. doi:10.1107/S0909049502014541

125. Kmetko J, Husseini NS, Naides M, Kalinin Y, Thorne RE. Quantifying X-ray radiation damage in protein crystals at cryogenic temperatures. *Acta Crystallographica Section D: Biological Crystallography*. 2006;62(9):1030-1038. doi:10.1107/S0907444906023869

126. Weik M, Ravelli RBG, Kryger G, et al. Specific chemical and structural damage to proteins produced by synchrotron radiation. *Proceedings of the National Academy of Sciences of the United States of America*. 2000;97(2):623-628. doi:10.1073/pnas.97.2.623

127. Karuppasamy M, Karimi Nejadasl F, Vulovic M, Koster AJ, Ravelli RBG. Radiation damage in single-particle cryo-electron microscopy: Effects of dose and dose rate. *Journal of Synchrotron Radiation*. 2011;18(3):398-412. doi:10.1107/S090904951100820X

128. Hattne J, Martynowycz MW, Penczek PA, Gonen T. MicroED with the Falcon III direct electron detector. *IUCrJ*. 2019;6:921-926. doi:10.1107/S2052252519010583

129. Taylor G. The phase problem. *Acta Crystallographica - Section D Biological Crystallography*. 2003;59(11):1881-1890. doi:10.1107/S0907444903017815

130. Evans P, McCoy A. An introduction to molecular replacement. *Acta Crystallographica Section D: Biological Crystallography*. 2007;64(1):1-10. doi:10.1107/S0907444907051554

131. Schenk H. An Introduction to Direct Methods . The Most Important Phase Relationships and their Application in Solving the Phase Problem. *IUCr Teaching pamphlet*. 1984;(i):1-27.

132. Zubeita C, Nanao M. Practical Radiation Damage-Induced Phasing.pdf. *Methods in Molecular Biology*. Published online 2016.

133. Drenth J. The Solution of the Phase Problem by the Isomorphous Replacement Method. *Principles in Protein X-ray Crystallography*. Published online 1994:129-179. doi:10.1007/978-1-4757-3092-0_7

134. Hendrickson WA. Anomalous diffraction in crystallographic phase evaluation. *Quarterly Reviews of Biophysics*. 2014;47(1):49-93. doi:10.1017/S0033583514000018

135. Shi D, Nannenga BL, Iadanza MG, Gonen T. Three-Dimensional Electron Crystallography of Protein Microcrystals. *Elife*. 2013;2(0):01345. doi:10.7554/elife.01345.

Chapter 3: A comprehensive protocol for MicroED sample preparation.

Authors

Cody Gillman[1,2*], Sara Weaver[1*], Max Clabbers[1,3], Anna Shiriaeva[1], Ampon Sae Her[1], Michael Martynowycz[1] and Tamir Gonen[1,2,3,4$]

[1.] Department of Biological Chemistry, University of California Los Angeles, Los Angeles, CA 90095 USA

[2.] Molecular Biology Institute, University of California, Los Angeles, Los Angeles, CA 90095 USA

[3.] Howard Hughes Medical Institute, University of California Los Angeles, Los Angeles, CA 90095 USA

[4.] Department of Physiology, University of California Los Angeles, Los Angeles, CA 90095 USA

* equal contribution

[$] to whom correspondence should be addressed T.G. tgonen@g.ucla.edu

Abstract

Since its advent in 2013, Microcrystal Electron Diffraction (MicroED) has revolutionized structural determination across a spectrum of samples, encompassing small organic molecules to proteins. A significant number of these were previously intractable using other existing structural methodologies. MicroED is a cryogenic transmission electron microscopy technique wherein small, three-dimensional crystals are continuously rotated in the electron beam, and diffraction data are collected as a movie using a fast camera. MicroED data can be processed with mainstream X-ray crystallographic software to solve

structures. In biology, the emergence of MicroED closed a crucial gap between the determination of structures from 2D crystals and 3D crystals, facilitating the study of small 3D crystals. In chemistry and material science, MicroED opened a new pathway for the routine and rapid determination of atomic resolution structures from complex small molecule mixtures without any necessary purification or crystallization assays. This comprehensive introduction to sample preparation methods for MicroED covers the most common methods used in the field. It should serve the growing community as a detailed guide for successful MicroED experiments.

Introduction

Development of Microcrystal Electron Diffraction (MicroED).

Microcrystal Electron Diffraction (MicroED) is a cryogenic transmission electron microscopy (cryoEM) technique used to solve structures from small, 3D crystals. Prior to the development of MicroED, electron crystallography methods were applied to 2D crystals to resolve proteins as small as 17 kDa to 3.5 Å and 28 kDa to 1.9 Å resolution[1,2], but 2D electron crystallography was largely abandoned as existing methods were complex, inefficient, and required a high level of expertise to perform. A few examples of 3D crystals that were only 2 or 3 layers thick were solved using 2D electron crystallography methods[2–5]. Electron diffraction data from small hydrated 2D and 3D crystals at room temperature was reported in the 1970s[6–10]. Electron diffraction data were also collected on sugar-embedded, dried samples[11,12]. Utilizing frozen samples in the electron microscope improved data quality. Electron diffraction for frozen-hydrated protein crystals was first reported in 1974 for thin crystals of catalase[13], and later for crotoxin[14]

and calcium-ATPase[15]. In these latter examples, hundreds of images were recorded from individual crystals, but structures were unsuccessful, probably due to indexing issues. Regardless, electron crystallography was not routinely applied to 3D crystals due to challenges related to radiation damage, diffraction pattern indexing[16] and suspected dynamicall scattering errors[14,15].

As electron crystallography remained a niche technique for decades, macromolecular structures were mainly solved using X-ray crystallography, and to a lesser extent, nuclear magnetic resonance (NMR) and neutron crystallography. More recently, single particle cryoEM has gained popularity as direct electron detectors became available. However, each of these methods has some specific drawbacks. Single particle cryoEM becomes increasingly more difficult as the molecular weight of the sample decreases, and for visualizing highly flexible domains. NMR is a powerful tool to probe dynamics of small molecules and small proteins, but poses challenges for structure determination of most proteins. X-ray crystallography requires large, well-ordered crystals to provide sufficient signal and resist radiation damage during synchrotron data collection[17–19]. Producing large, well-ordered crystals can be a challenging and time-consuming endeavor, especially for membrane proteins in a lipid-mimicking environment[20,21]. If there is an abundance of nanocrystals (5 to 30 μm), Serial Femtosecond x-ray crystallography (SFX) can be used, but access to the ultrafast x-ray Free Electron Laser (XFEL) required to perform SFX is limiting[22]. Neutron protein crystallography allows biochemists to visualize hydrogen atom positions within protein crystals but requires even larger protein crystals made from isotopically-substituted proteins[23].

While several methods were developed in electron diffraction over the years, none became as widely used as MicroED because data collection for MicroED is fast and can be seamlessly and routinely processed using existing powerful crystallographic software, and it is the only approach allowing structure solution for macromolecular samples like proteins that crystallize in three dimensions.[24–35].

The crystals used in MicroED are a billion times smaller than crystals routinely used for X-ray or neutron crystallography[36]. Using small crystals for electron diffraction is feasible because electrons interact more strongly with matter than X-rays[37]. Only elastically scattered X-rays and electrons productively contribute to the diffraction pattern. The ratio of elastic to inelastic scattering is much higher in electron diffraction (1:3) than in X-ray diffraction (1:10), so more useful information is gained per damaging event in electron diffraction[37]. As a result, a crystal in an X-ray diffraction experiment must withstand more damaging inelastic x-ray scattering to obtain the same amount of information as in an electron diffraction experiment.

In a MicroED experiment, crystals are applied to a transmission electron microscopy (TEM) grid and diffraction data are collected as a given crystal is continuously rotated in a parallel electron beam. The data are processed using common X-ray crystallographic software[25,38–49]. MicroED data have been phased using *ab initio* methods and molecular replacement[31,33,34,36,50,51]. Electrons can probe charge distribution in a sample and reveal atomistic details of amino acid side chains[27,34,52–59].

Preserving hydrated samples for TEM

The chamber of the transmission electron microscope is held under high vacuum, so samples must be preserved to withstand the vacuum. Environmental liquid cells were developed to facilitate the examination of wet samples within the electron microscope[6,7,60–62]. Liquid cell electron microscopy is more commonly used in materials science than biological TEM. Early reports using TEM for biological samples suggested preservation by fast cooling of the sample, treating the sample with a substance to slow its destruction, or encasing the sample in a stain[63–65]. One method to slow the destruction of the sample is sugar embedding. Sugar embedding was first presented in 1975 when Unwin and Henderson embedded crystals of bacteriorhodopsin in 1% glucose before drying and inserting into the TEM[11]. However, treatment of crystals with glucose can cause glycation of the proteins[66]. Subsequent sugar embedding protocols typically used trehalose as it is relatively inert[2,52,67–71]. Trehalose can act as a cryoprotectant and may reduce beam damage[68,72]. In later work, sugar embedding was used to protect crystals from dehydration before vitrification[66]. Crystals may also be sandwiched between carbon films to reduce dehydration during blotting[69,73].

Cryogenically-cooled TEM stages were developed so that frozen samples could be inserted into the vacuum of the electron microscope[74]. Maintaining samples at cryogenic temperatures significantly reduces radiation damage from the electron beam[75]. The first report of a frozen-hydrated biological specimen examined by TEM was electron diffraction of catalase crystals[13]. In the 1974 paper, catalase crystals were placed on a folding grid, blotted with filter paper, and frozen in liquid nitrogen[13]. This method of blotting and freezing was too slow to prevent the formation of crystalline ice[76], which can distort

biological specimens. However, when a thin layer of liquid is rapidly cooled, vitreous or amorphous ice can be obtained[77]. The first demonstration of vitrification for cryoEM sample preparation involved passing a grid through a jet of pure water droplets and then plunging it into the cryogen (liquids nitrogen, ethane or propane)[78–80]. As a result of these investigations, liquid ethane was selected as the most effective cryogen. Today, in addition to pure liquid ethane, samples can also be vitrified using a mixture of liquid ethane and liquid propane[81].

Experimental design for MicroED sample preparation.

CryoEM sample preparation is a critical step in any experiment. Several protocols describing aspects of MicroED sample preparation have been published[28,82–89], but none provide a comprehensive, detailed guide for sample preparation in MicroED.

This protocol provides a comprehensive guide to sample preparation for MicroED -- from proteins (Figures 3.4-3.6 and 3.8) to small molecules and peptides (Figure 3.5) using knowledge accumulated over the first decade of MicroED.

In a MicroED experiment, the sample can be applied to the TEM grid as a solid, liquid, or crystalline slurry. Application of a solid to the TEM grid typically occurs at room temperature. Liquid or slurry samples can be dried onto the TEM grid or vitrified onto the TEM grid. If the sample is susceptible to damage by dehydration, the sample should be vitrified and maintained at cryogenic temperatures. The ideal MicroED sample contains monodisperse crystals that are evenly distributed across an intact grid. Crystals should be far enough apart that diffraction is collected from a single crystal without interference

from neighboring crystals. The crystals should also adopt random orientations to avoid preferred orientation problems.

Optimal crystal size at different kV

In the TEM, high-energy electrons irradiate the sample[37]. A fraction of the incident electrons is scattered upon interaction with the sample[90]. In a MicroED experiment, the crystalline sample must be thin enough to allow high-quality data collection but thick enough to generate a significant signal. Electrons can scatter once (elastic scattering) or multiple times (inelastic scattering). In an inelastic scattering event, the incident electron loses energy. Inelastic scattering events can deposit energy within the sample, causing radiation damage. The inelastic mean free path (MFP) describes the distance an electron travels within a sample before an inelastic scattering event[91–95]. The MFP of a theoretical protein crystal can be calculated for a given TEM accelerating voltage. Recently, a MicroED study benchmarked the crystal thickness limit at accelerating voltages of 120, 200, and 300 kV[96]. Typical TEM accelerating voltages and the corresponding MFP are 120 kV and 214 nm, 200 kV and 272 nm, and 300 kV and 317 nm[96] (Table 3.1).

Table 3.1. Inelastic mean free path versus TEM accelerating voltage.

TEM Accelerating voltage	Inelastic mean free path
120 kV	214 nm
200 kV	272 nm
300 kV	317 nm

Proteinase K crystals were grown in batch, vitrified, and FIB milled into lamellae of different thicknesses (95 nm to 1650 nm thick). Data were collected at 120 kV, 200 kV, and 300 kV, and the processing statistics were compared to determine the optimal crystal thickness range at each accelerating voltage. Martynowycz et al. concluded that lamellae up to twice the mean free path for a given accelerating voltage produced high-quality MicroED data and facilitated structure determination. Crystals thicker than twice the MFP displayed some diffraction, but it was insufficient to solve the structure of Proteinase K.

Preparation and identification of microcrystals

For proteins, standard macromolecular crystallization methods are used to prepare crystals. MicroED has been performed using crystals from batch crystallization, vapor diffusion (hanging or sitting drop), liquid-liquid diffusion, crystallization in lipidic mesophases (lipidic cubic phase or LCP) in syringes, and bicelle crystallization.

Microcrystals can be identified in crystal screen drops using a various methods, including crossed polarizing microscopy, UV microscopy[97], transmission electron microscopy (TEM)[98–101], and second-order nonlinear optical imaging of chiral crystals (SONICC) [102]. Methods to identify microcrystals for MicroED were recently reviewed[103].

For some samples, like peptides and small molecules, crystals often form spontaneously when the sample is dried. If the sample is dissolved in a solvent, you may be able to crystallize it by evaporation using a lyophilizer, a rotary evaporator (rotovap), or under ambient conditions directly on to a TEM grid[104–108]. Dried samples can be ground into a fine powder before being applied to the TEM grid to increase the number of crystal sites available for data acquisition.

TEM grid basics

TEM grids must be robust enough to survive sample application and irradiation by the electron beam but also thin enough to allow transmission without degrading data quality[109]. TEM grids are made of a metal mesh base, which is approximately 3 mm in diameter (Figure 3.1a). The grid mesh pitch is the number of grid squares per inch, and typical values for cryoEM applications are 200 to 400. Copper and gold are the most common grid mesh materials, though aluminum, molybdenum, nickel, silicon, titanium, tungsten, and others are also available. If the sample will be vitrified, materials with higher electric conduction and heat dissipation are preferred to facilitate

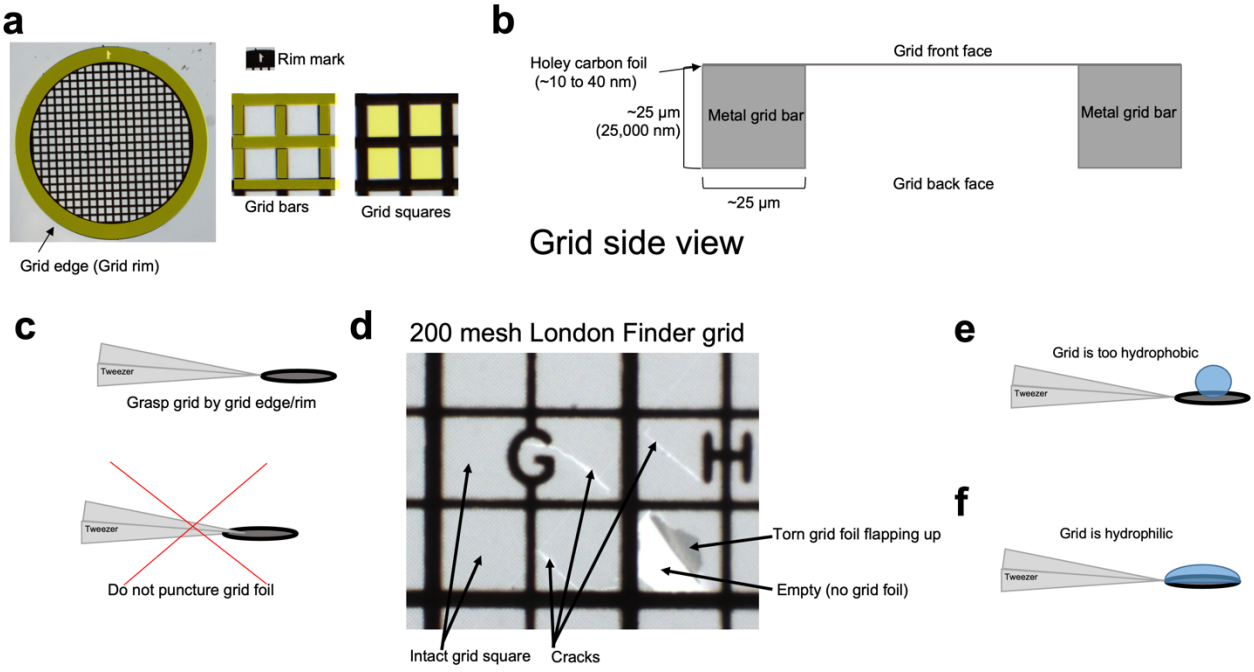

Figure 3.1. Overview of TEM grids. (a) The anatomy of the front face of a TEM grid. The holey carbon support foil is on the front face. (b) The anatomy of a TEM grid viewed from the edge. There is no carbon support foil applied to the back face. (c) How to grasp a TEM grid using tweezers. (d) Assessing the quality of the grid foil. (e) An aqueous sample will ball if the TEM grid is hydrophobic. (f) An aqueous sample will spread if the TEM grid is hydrophilic.

rapid cooling[110,111]. The TEM grid mesh is coated with a foil (often, but not limited to, amorphous carbon), which can be continuous[112] or perforated. The perforations in the foil may be irregularly sized and arranged (as in the case of some holey or lacey grids) or regularly sized (0.6 to 35 μm) and distributed (holey grids like Quantifoil or C-Flats)[109,113–118]. Grids with smaller holes show reduced stress upon irradiation with the electron beam[119]. The front face of the grid is the side that the grid foil was applied to while the back face is the opposite side (Figure 3.1b). For most applications, the front face of the grid is cleaned and used for sample application.

Grids should be stored in a clean, dry place that minimizes dust and oil contamination[120]. Grids should be handled carefully and minimally to keep them as flat as possible to avoid strain during plunging. The tweezers should grasp the grid by the outer rim to avoid disrupting the foil (Figure 3.1c-d). Grids should plunge into the cryogen perpendicular to the cryogen surface. If the grid enters the cryogen at a different angle, broken squares are more common, and the stability of the grid is reduced.

TEM grid selection

A variety of TEM grid types (continuous carbon, holey carbon, lacey carbon) have been successful for MicroED experiments. Grids with a higher mesh value have more grid bars and smaller grid squares, increasing their stability but reducing the usable area. Grids with holey or lacey carbon surfaces on 300 mesh grids are recommended for vitrified samples. If the sample will be FIB milled, 200 mesh grids should be used as they have a larger area accessible for milling with sufficient mechanical stability (Table 3.2). For dry powders and liquid/slurry samples dried onto the grid, grids with continuous carbon surfaces on 300 or 400 mesh are recommended (Table 3.2). The increased stability of continuous carbon is helpful in small molecule MicroED if the grid is dragged through a powder for sample application.

Table 3.2. Electron microscopy grid selection for MicroED.

Sample type	Foil	Grid mesh	Hole size (μm)	Hole spacing (μm)
Dry	Continuous carbon	300 or 400	n/a	n/a
Vitrified	Holey carbon	200 to 300	0.6 to 2	1 to 2
Vitrified for FIB milling	Holey carbon	200	2	2
Suspended drop	Support-free	50 to 150	n/a	n/a

Cleaning the TEM grid

The TEM grid's surface characteristics greatly influence the sample distribution across the grid. A freshly prepared carbon-coated TEM grid is hydrophilic, but environmental contamination can build up during storage, and grids become hydrophobic[121]. If a grid is hydrophobic, an aqueous sample will ball up on the surface (Figure 3.1e). If the grid is hydrophilic, an aqueous sample will spread out on the grid surface (Figure 3.1f). The degree of grid hydrophilicity required for your experiment will depend on the chemistry of your sample. While the hydrophobic character of the typical TEM grid can benefit some samples, most MicroED samples are prepared using a low-energy plasma to increase the hydrophilicity of the surface. Generating plasma in residual air (glow discharging) is most common, but plasmas generated from hydrogen, an argon:oxygen mixture, or amylamine are also popular in cryoEM[120]. If the grid is contaminated with a buildup of plastic components involved in the grid manufacturing process, it can be cleaned with acetone, chloroform, methanol, isopropanol, and/or water[120].

Applying the sample to the TEM grid

The sample can be applied to the front side, the back side, or both sides of the TEM grid. In some TEMs, the grid is loaded directly onto the stage, while other models require the user to secure the grid into a cartridge or autogrid, which is then loaded into the microscope and mounted onto the

stage. For solid state samples, clipping the TEM grid into an autogrid before applying the sample can be beneficial because clipped grids demonstrate increased stability during sample preparation, which is helpful for situations where the grid is dragged through powder. Clipping before sample application is optional and not required. For a liquid or slurry sample, the sample is typically applied to the front face of the grid and/or to the face that was glow discharged. Crystals can be pipetted from the crystal screen plate to the TEM grid, or one can touch the grid surface to the crystal drop. If the sample buffer contains high salt concentrations, as soon as the crystal tray seal is broken and the sample is exposed to air, these salts may precipitate. This can cause background signal and false positives during MicroED screening. Work as quickly as possible to reduce salt crystal contamination after opening the crystal tray drop. Other options include diluting the drop prior to applying it to the grid, performing sample preparation in a cold room, and rinsing the crystals in a low salt buffer prior to grid application[26].

Blotting method

Liquid or crystalline slurry samples are applied to a TEM grid and excess liquid is blotted away to leave crystals embedded in a thin film of liquid just before vitrification. The period between blotting and plunging is critical because evaporation of liquid off the crystal surface before vitrification can cause harmful changes to the temperature, osmolarity, pH and solute concentration of the crystal[122–124]. If sample preparation occurs under ambient conditions on the lab bench (20 °C and 40% relative humidity), the risk of evaporation is high. Maintaining relatively high humidity during blotting can slow evaporation and improves reproducibility during sample preparation[125].

The blotting duration and the number of blots influences the crystal distribution on the grid and the ice thickness. The sample can be blotted manually (by hand) or using an automated blotting machine. Manual blotting can occur on the bench top, in a humidified chamber, or in an automated blotting machine. The sample can be blotted from one face

of the grid or both faces simultaneously. If the sample is blotted from the same face it was applied to, there may be significant sample loss to the filter paper. Despite this disadvantage, blotting from the same face may give more uniform ice thickness across the grid. The blotting paper can graze the grid at an angle or can fully contact the grid during blotting. Blotting at an angle will result in an ice thickness gradient across the grid, which may help locate the ideal ice thickness for a given crystal. The sample can also be blotted using pressure-assisted back blotting[126]. The ice thickness can be related to the face of the grid the sample is applied to. When a liquid or slurry sample is applied to the back face of the grid, liquid can cling to the juncture between the grid foil and the grid bar, leading to thicker ice or a thicker deposit of sample upon evaporation.

Manual blotting

To improve reproducibility and control, many cryoEM practitioners prefer to blot grids manually over relying on automated vitrification machines. Manual blotting can be performed on the bench top by hand (Figure 3.2a), in the chamber of an automated vitrification machine (Figure 3.2b-c), or with a manual gravity plunger (Figure 3.2d)[124,125,127,128].

For manual blotting experiments, prepare strips of filter paper (approximately 0.5 cm by 2 cm) (Figure 3.2e). Use a flat tweezer to manipulate the blotting paper. Using a rubber O-ring to hold the tweezers closed is recommended, but this is optional. For manual blotting experiments, the blotting paper can be displayed on the tweezer in a variety of ways. For example, with the tweezer, grasp the two ends of the

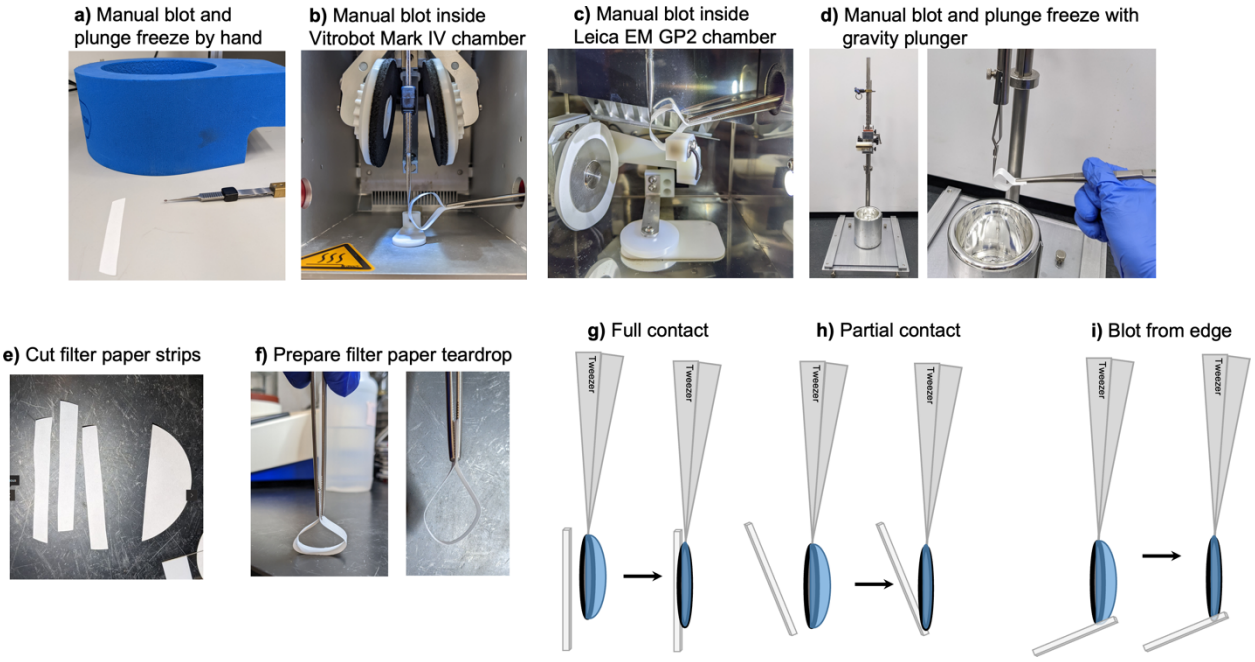

Figure 3.2. Manual blotting TEM grids for MicroED.

filter paper strip such that the paper forms a teardrop shape (Figure 3.2f). The flat expanse of filter paper can be directly applied to the grid surface. The edge of the filter paper can be dabbed on the grid surface. The edge of the filter paper can be used to blot from the side of the grid (Figure 3.2g-i). Gently push the filter paper through the side door of the plunging apparatus humidity chamber and press it against the face of the grid. Try not to agitate the grid as you blot. The sample liquid will spread out on the filter paper as you blot and eventually the wet spot will appear to stop growing. Watch that the wet spot has stopped growing, then count for an additional 3 to 5 seconds before carefully pulling the filter paper back in one motion.

Fragmenting crystals

MicroED data can be collected and phased for protein crystals that are less than twice the inelastic mean free path (MFP) (see Table 3.1)[96]. Large crystals may be composed of mosaic blocks that have varying unit cell parameters or are misaligned, leading to complex diffraction patterns[129,130]. In some cases, smaller crystals may display less mosaicity[131]. However, small crystals may clump together, yielding overlapping diffraction patterns (Figure 3.3, left). If clumped crystals are observed on the grid, crystals can be fragmented before grid preparation.

Crystals can be separated and fragmented using various methods, including water bath sonication, pipetting, vortexing, and mechanical probing[28]. Crystal fragments are

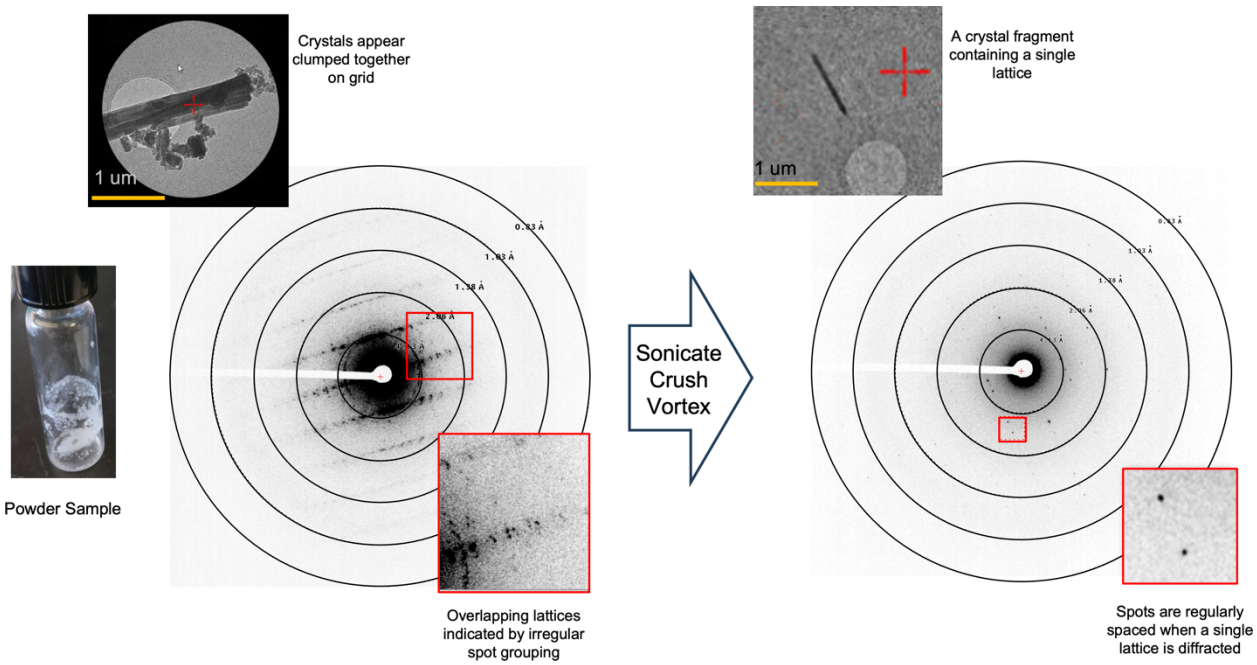

Figure 3.3. Crystal fragmentation as a strategy to prevent overlapping crystal lattices in MicroED datasets.

more likely to contain a single lattice for diffraction (Figure 3.3, right). Some fragmentation methods are too harsh for a given crystal and destroy the lattice, while sometimes they are too gentle to reduce crystal size and/or clumping. The progress of crystal fragmentation can be monitored using a light microscope. If mechanical disruption methods do not yield appropriately sized crystals or if they damage fragile crystals, FIB milling can be used.

Milling membrane protein crystals in LCP

Membrane protein crystals in LCP tend to be small and well-ordered, but the samples have the consistency of a thick paste, which can be challenging for cryoEM sample preparation[132–136]. Despite extensive blotting, crystals embedded in LCP often form a thick layer on the grid, which makes the sample too thick for MicroED. Membrane protein crystals grown in LCP plates can be transferred to a grid using a crystallographic loop, vitrified, and then thinned for MicroED using FIB milling[135,136] (Figure 3.4). Frozen LCP is a difficult target for FIB milling, and accessing the embedded crystals after vitrification may be problematic[135,136]. To reduce the viscosity of crystals in LCP and make the samples accessible by FIB milling, the LCP can be converted to sponge phase or dissolved before the application of sample to the grid (Figure 3.4 and 3.6). The additives that can convert the phase from LCP to sponge are 2-Methyl-2,4- pentanediol (MPD), PEG400, PEG200, Jeffamine M600, t-butanol, ethylene glycol, and 1,4-butanediol. In experiments with LCP-embedded Proteinase K crystals, MPD showed the best results[134].

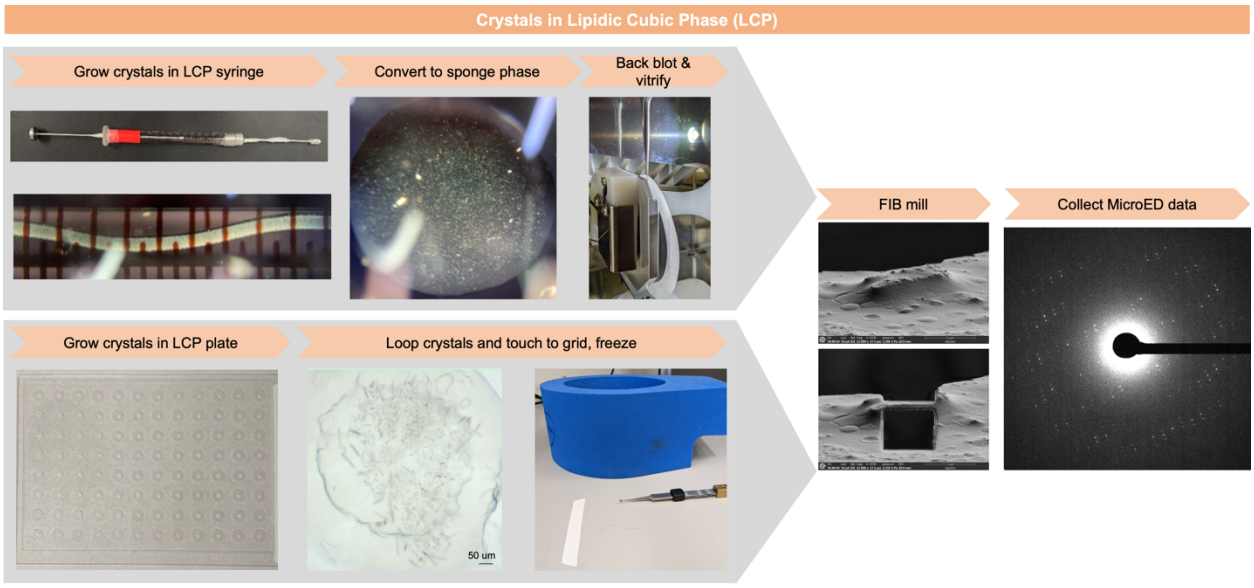

Figure 3.4. Preparation of LCP samples for MicroED. Crystals can be grown either in a syringe or LCP plate. When grown in a syringe, the LCP is converted to the sponge phase to reduce sample viscosity and allow for back blotting. In contrast, when LCP crystals are in a plate, they can be harvested directly using a crystal loop. Because it is difficult to sufficiently blot LCP samples, FIB milling is typically used to access LCP crystals embedded in crystallization media.

Martynowycz et al. converted crystals in LCP to the sponge phase and solved the structure of the human adenosine receptor by MicroED[136]. Once in the sponge phase, the crystals can flow out of a syringe needle and onto the TEM grid, which is then blotted inside a high-humidity chamber. Removing surrounding media allows crystal topological features to be distinguished in the FIB/SEM instrument and accurately targeted for milling. However, conversion to sponge phase is not always successful and blotting can still be difficult as the samples tend to be rather viscous. If blotting is weak due to sample viscosity, it may be possible to observe inconspicuous bumps at the surface of the sample in the FIB/SEM, which could be crystal sites worth milling[137].

A novel methodology was recently demonstrated that eliminates the need to separate integral membrane protein crystals away from the surrounding LCP matrix[138,139] (Figures 3.10-3.12). In these studies, the protein of interest was labeled with a fluorescent dye prior to LCP crystallization. Once inside the FIB milling instrument, fluorescent crystals were detected using an integrated fluorescence light microscope (iFLM). Correlative light microscopy (CLEM) techniques were applied to accurately align a plasma beam FIB (pFIB) for crystal milling. Employing this experimental approach, conversion of the LCP to the sponge phase and blotting, as previously demonstrated[136], was unnecessary. A similar CLEM-based workflow was also applied in the first demonstration of "suspended drop crystallization" for MicroED[140].

Suspended drop crystallization

Difficulties associated with crystal transfer and blotting can introduce significant bottlenecks during MicroED sample preparation. Crystals that are particularly sensitive to physical manipulation can be damaged while pipetting, and a large portion of crystals can be lost inside the pipet tip and to the blotting filter paper. Overblotting the TEM grid can cause dehydration of crystals, whereas underblotting results in crystals being encased in excessively thick media. Troublesome blotting issues are exacerbated when working with highly viscous samples. Lastly, the morphology of some crystals causes them to adopt a preferential orientation on the TEM grid support layer. If the preferential orientation is systematic, obtaining sufficient dataset completeness for structure determination can become challenging.

A novel method for crystallization named “suspended drop crystallization” was recently demonstrated[140]. Suspended drop crystallization overcomes many challenges associated with MicroED sample preparation as it provides an alternative workflow for crystals embedded in viscous media, sensitive to mechanical stress, and/or suffering from preferred orientation on TEM grids. Here, crystals are grown directly on a support-free TEM grid without any support film (Figure 3.8). The support film is not necessary because the liquid surface tension of the crystal drop allows it to be retained by the grid bars alone. The crystal drop is considered “suspended” because vapor diffusion occurs uniformly from all sides of the drop. Growing crystals directly on the grid allows one to bypass both crystal transfer and blotting during sample preparation. The suspended drop containing crystals is used directly for MicroED data collection. In a recent study it was demonstrated that with this approach the missing cone was eliminated for two samples that typically adopted a preferred orientation.

Vitrification method

MicroED samples are preserved by vitrification – a critical step for most protein samples and one that can be highly beneficial for small molecules[141]. When biological samples are frozen in crystalline ice, the formation of ice crystals may distort and damage the crystal lattice. If liquid water is cooled sufficiently fast (10^5 to 10^6 K/s)[142,143], water molecules are locked in place before they have time to rearrange into a crystalline lattice [144]. This amorphous (or vitreous) ice cryofixes the sample without damaging it. To form vitreous ice, a droplet of crystal sample is applied to a TEM grid and blotted so that only a thin aqueous film coats the sample. The TEM grid is then rapidly plunged into a cryogen with a high heat capacity and thermal conductivity. The bulk cryogen in typical cryoEM experiments is liquid nitrogen because it is inexpensive and readily

available. Most samples for modern cryoEM are vitrified using liquid ethane or a mixture of liquid ethane and liquid propane[81,143].

Vitrification can be performed using a manual gravity plunger[124,125,127,128] or a commercially available automated vitrification machine (e.g., Thermo Fisher Scientific Vitrobot, Leica Microsystems EM GP/GP2, Gatan CryoPlunge3). This protocol described the vitrification procedure using a Leica GP2 punge-freezer. The Leica GP2 is designed to blot from behind the TEM grid only, which is preferred for crystal samples applied to the opposite side of the grid.

For some applications, grids can be frozen by hand at the bench (Figure 3.2) in a method similar to flash-cooling (shock-cooling) crystals mounted in loops for x-ray diffraction experiments[145,146]. If this method is used, aim to keep the grid perpendicular to the surface of the cryogen during plunging. However, the time between blotting and plunging may be too slow for some sensitive samples when performed by hand. Ideal blotting creates a thin buffer layer containing the crystals of interest on the TEM grid. If the time between blotting and vitrification is too long, the buffer can evaporate and dehydrate the sample[136] (see Table 3 for sample preparation troubleshooting tips).

Materials

Reagents

- Proteinase K from *Engyodontium album* (previously called *Tritirachium album*) (Sigma-Aldrich Catalog P2308, storage -20°C
- 2-(N-morpholino)ethanesulfonic acid (MES) sodium hydroxide, pH 6.5

- Proteinase K crystallization buffer: 0.1 M MES-sodium hydroxide pH 6.5, 0.5 M sodium nitrate, 0.1 M calcium chloride
- 100% Polyethylene glycol 400 (PEG400), Hampton Research Catalog HR2-603
- 100 µL Gas-tight syringes with removable needle (Hamilton, Cat. No. 81065)
- Syringe coupler (Formulatrix, SKU 209526)

Equipment

- PELCO easiGlow glow discharge apparatus
- Leica Microsystems EM GP2 plunge-freezer
- Glass petri dish for grid transportation
- Glass slide for glow-discharging
- Hampton Research Micro-Brush (HR4-845)
- Glass microscope slide to grind powder samples (like Fisher Scientific Catalog No. 12-544-4)
- Kimtech Science™ Kimwipes™ Delicate Task Wipes, Kimberly-Clark Professional #34120
- Whatman® qualitative filter paper, Grade 1, 90 mm circle, #WHA1001090
- Tungsten carbide glass cutter
- Removable flat-tipped needle for loading samples into LCP-injector (1 inch, point style 3, gauge 22, small hub; Hamilton, Cat. No. 7804-01)
- LCP Sandwich Set – Hampton Research item HR3-151
- MiTeGen loops, size 50-100um
- Ted Pella Carbon Type-B, 300 mesh Copper grids #01813

- Quantifoil R2/2 Holey carbon grid copper 200 mesh, Quantifoil
- Ted Pella Gilder Grids, 150 mesh Gold (Cat. No. G150G)
- Liquid nitrogen
    - Caution: Working with liquid nitrogen necessitates appropriate safety equipment (safety glasses, face shield, cryo gloves) and sufficient ventilation.
- Cryogen for vitrifying grids (liquid ethane or a 50%/50% (v/v) mixture of ethane and propane)
    - Caution: Ethane and propane are flammable

Reagent set up

Batch crystallization of proteinase K

Prepare Proteinase K crystals in a cold room, or on ice[34,147].

1. In an Eppendorf tube, resuspend 20 mg Proteinase K from *Engyodontium album* in 0.5 mL 0.02 M 2-(N-morpholino)ethanesulfonic acid (MES) sodium hydroxide pH 6.5 buffer
2. Add 0.5 mL ice cold Proteinase K crystallization buffer
3. Vortex for 1 minute or until the solution appears clear.
4. Incubate at 4°C overnight

Procedure

Prepare TEM grids for MicroED

5. Examine the TEM grids under a low magnification light microscope before use to identify any potential defects (Figure 3.1d). If grids are slightly bent or damaged, the integrity may be compromised and the usable area of the grid will be reduced.
6. Use a PELCO easiGlow machine with residual air and a negative charge to remove contamination from the grid surface and to generate a hydrophilic, negatively charged surface. Refer to the manufacturer's manual for the glow discharge apparatus for startup instructions.
7. Inspect the rim of the glass bell jar for defects, chips, or cracks. If there are cracks, the vacuum may not seal. Only touch the inside of the bell jar area with gloves on to avoid contaminating the system.
8. Run an initial cycle with an empty chamber (0.3 mBar, 60 seconds process time, 10 seconds hold time, 15 mAmp current and negative charge) to confirm that the machine reaches your desired vacuum and current.
9. Wrap a glass slide with parafilm to support the grids during glow discharging to make manipulation of the grids easier. Place the grids on the parafilm (front face up) without overlaps. Place the glass slide on the chamber's metal platform and center it. Replace the bell jar with care to maintain the O-ring position.
10. Run the glow discharge process. After the vacuum is achieved, a purple glow indicates that ionization is occurring.
11. Once the chamber has returned to atmospheric pressure, gently remove the glass bell jar. Remove the grids from the chamber and replace the bell jar. Store the

grids in a glass petri dish until ready to use. Grids should be used within 30 minutes of glow discharging. Grids can be glow discharged a second time if more than 30 minutes have passed or if the grids appear to have lost their hydrophilic character (Figure 3.1e, f).

Preserve the crystals on the TEM grid

Select the appropriate option (A-E) depending on the type of sample. Options A and B describe vitrifying protein crystals (Option A, Figure 3.5) and crystals in LCP sponge phase (Option B, Figures 3.4 and 3.6). Options C and D describe preparing dry grids. Option C describes starting from a solid (Figure 3.7, Top) while Option D describes starting from a crystalline slurry (Figure 3.7, Bottom). Option E describes growing crystals directly on the grid as suspended drops (Figure 3.5). Option F describes thinning membrane protein crystals embedded in LCP matrix (Figures 3.4, 3.10-3.12).

Option A: Vitrifying crystals

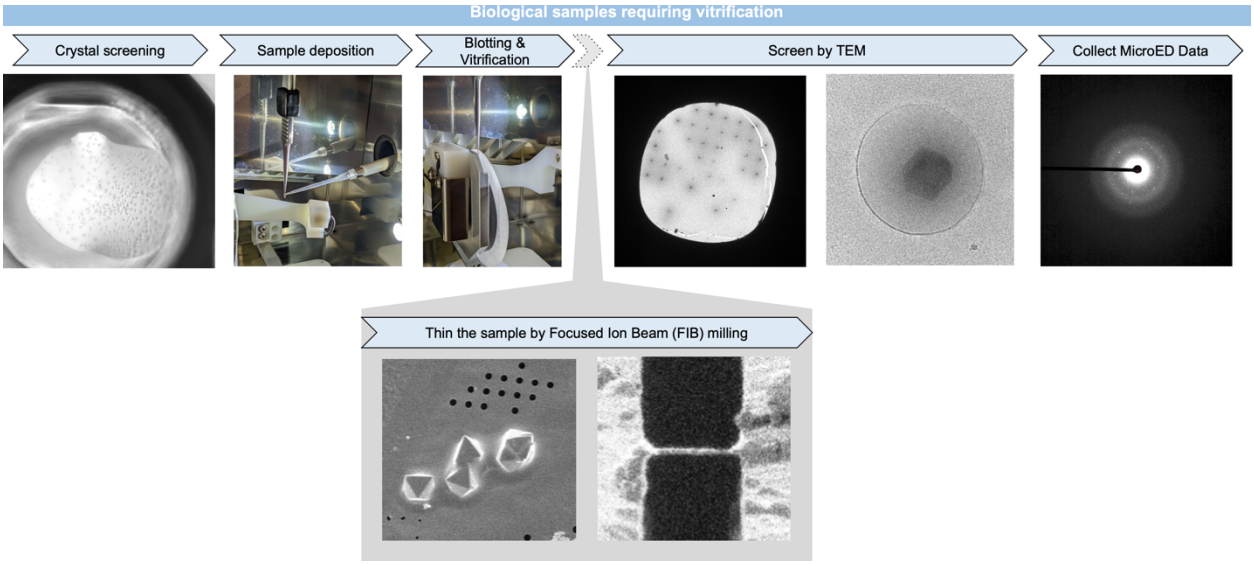

Figure 3.5. Outline of MicroED sample preparation steps for biological samples.

12. Set up the Leica EM GP2 according to manufacturer specifications.
    a. Input the blot time and number of blots. Blots can be triggered manually or automatically. For routine protein crystals, blot once for 3 to 10 seconds.
    b. Calibrate the blotting position such that the grid just begins to deflect from the tweezers when it is in contact with the filter paper.
    c. Refill the humidifier and set the humidity and temperature. Allow at least 30 minutes for equilibration to 95% relative humidity and 4°C.
    d. Assemble the plunging dewar and cool it with liquid nitrogen. Condense the cryogen into the plunging dewar cup. Ensure that the cryogen is at the correct temperature.
    e. Prepare a fresh piece of filter paper for blotting. The filter paper can be placed just before vitrification or first allowed to equilibrate to the temperature and humidity of the experiment.
13. (Optional) Fragment the crystals (see Info box on Crystal fragmentation)
14. Load the grid onto the tweezers by the outer rim (edge) (Figure 3.1a, c).
15. Pipet 2 µL of sample to the front face of the grid (Figure 3.5).
16. (Optional) The sample can be incubated on the grid (0 to 60 seconds) to improve the association of the crystals with the grid.
17. Blot away excess liquid using filter paper once for 10 seconds (Figure 3.5).
18. (Optional) If the sample concentration is low, crystals can be pipetted directly onto the grid one or more times. Sometimes, the sample is applied to the grid, blotted, and then applied again.

19. (Optional) Crystals can be washed on the grid if the mother liquor is expected to interfere with data collection. After applying the sample to one face of the grid, blot excess liquid from the opposite face. Apply a wash solution and optionally incubate for 30 to 60 seconds. Blot the sample again to complete the wash cycle.
20. (Optional) On-grid ligand soaking
    a. Apply the sample to the front face of the grid and optionally incubate to allow the crystals to associate with the grid.
    b. Blot the sample from the back to minimize crystal association with the filter paper.
    c. Immediately apply the ligand solution to the front face of the grid and incubate (typically 20 seconds). The time between the initial blot and the application of the ligand solution should be minimized so that the crystals do not dry out.
    d. After ligand incubation, remove excess ligand solution by back blotting.
21. Immediately after blotting, plunge the grid into the cryogen. In the Leica, plunging can be triggered manually or automatically.
22. After plunging the grid into the cryogen, it can be transferred to a storage box or loaded into a microscope. Grids can be stored indefinitely. However, ice contamination can build up over time in the dewar.
23. If the crystals will be thinned by FIB milling prior to MicroED, refer to the previously published general protocol for blotting, freezing, and milling crystals on TEM grids using a FIB equipped with a gallium source[82].

Option B: Conversion of Lipidic Cubic Phase (LCP) to sponge phase.

If crystals were grown in Lipidic Cubic Phase (LCP) in a glass plate or within a glass syringe [148,149], the following protocol can be used to convert the LCP to sponge phase to blot the grids for MicroED[135,136]. A general protocol for blotting, freezing, and milling crystals on TEM grids using a FIB equipped with a gallium source was previously published[82].

24. Equilibrate the Leica chamber to 90% relative humidity and 20°C.
25. If the sample was crystallized in a glass plate, use a glass cutter to carefully remove the glass from the drop. Transfer the grid to the blotting chamber.
26. If samples were crystallized in syringes (Figure 3.6a), remove the liquid media from the syringes (Figure 3.6b), leaving only LCP with the crystals (4-5 µL).

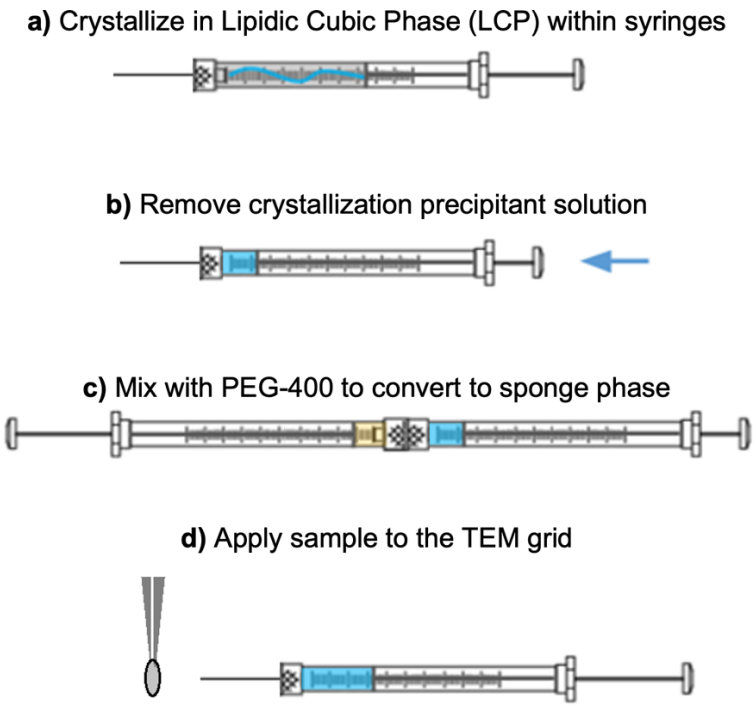

Figure 3.6. Workflow for LCP to sponge phase transition to prepare MicroED sample.

27. Convert the LCP to sponge phase to decrease the viscosity of the sample and facilitate blotting. Mix the crystals in LCP with small portions (1-2 μL) of 100% PEG400 using a syringe coupler, until the sponge phase is achieved (Figure 3.6c).

    (CRITICAL STEP) This step should be done as quickly as possible. If the LCP contains cholesterol, cholesterol crystals can form in excess PEG400. If protein crystals are large, they will be fragmented by mixing at this step.

28. Attach a 50 mm needle to the syringe and eject a small drop (0.5-2 μl) of the sample onto the cover glass. The sample should come out without additional force. Analyze the size, density, and quality of crystals by cross-polarized microscopy. Eject a drop of the sample (0.5-1 μL) from the syringe onto the grid inside of the blotting chamber (Figure 3.6d).
29. For all samples, blot the grid from the front and the back for 3 seconds each. The blotting time can be optimized for each sample. Exposure of the crystals to the air should be minimized as dehydration can damage the crystals.
30. If the density of crystals is low, apply the sample to the grid and blot multiple times.
31. Plunge the grid into liquid ethane.
32. Transfer the grid to the box and store it under cryogenic conditions until the microscope session. To thin crystals by FIB milling, refer to the previously published general protocol for blotting, freezing, and milling crystals on TEM grids using a FIB equipped with a gallium source[82].

Option C: Drying crystals from a solid-state sample

Many solid chemicals contain microcrystalline particles that work well for MicroED[150–152]. Liquid samples can be dried to produce microcrystals for MicroED[104,106,150,153].

33. Prepare a clean workspace under ambient conditions, in a fume hood, in a temperature and humidity-controlled box, or in a glove box as required for the sample.
34. (Optional) If the microscope has an Autoloader, the grid can be clipped prior to sample application to increase its stability.
35. Grind the sample into a fine powder between two glass slides. Set one glass slide down on a piece of clean filter paper and apply sample to the top of the glass slide. Place the other glass slide directly on top to sandwich the sample between the glass slides (Figure 3.7, Top). Pick up the slide/sample sandwich and gently move the slides against each other to grind the powder. Alternatively, a mortar and pestle could be used to grind the sample.
36. Gently set the grid onto the pile of powder sample (foil side down). The TEM grid can be flipped over a few times to coat both sides in sample. Try to avoid bending the grid or damaging the grid foil during this process.
37. To remove loosely associated sample, grasp the grid in tweezers and hold it 1 to 6 inches above a piece of filter paper. Drop the grid. Repeat 1 to 3 times. This can be done before or after clipping the grid if an autogrid will be used.

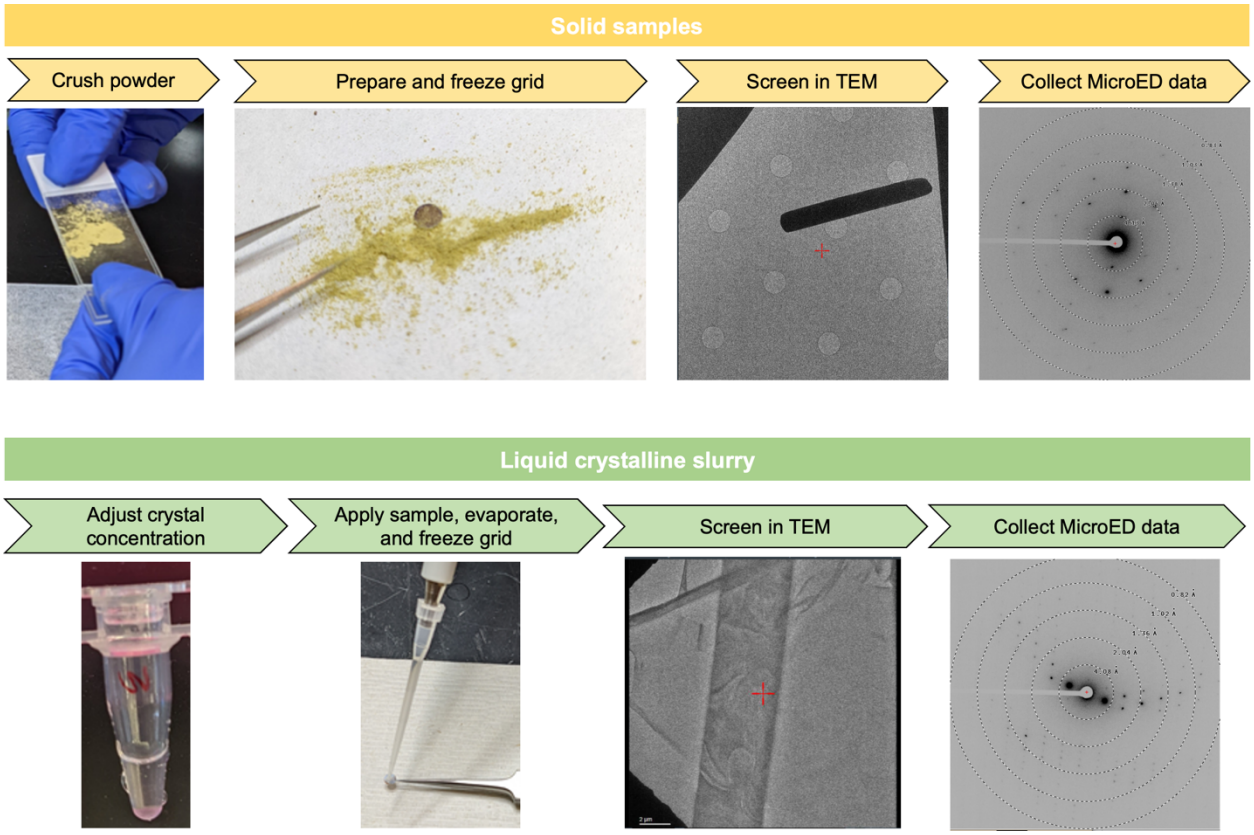

Figure 3.7. Preparation of dry samples for MicroED. Top) For solid samples, the powder is crushed until fine and the TEM grid is coated. Bottom) If starting from a crystalline slurry, the sample is applied to the grid and crystallization media is allowed to evaporate.

Option D: Drying crystals from a crystalline slurry sample

If the sample is a slurry of crystals suspended in the solvent and the crystals will not be damaged by dehydration, a dry sample can be prepared for MicroED (Figure 3.7, Bottom). The goal is to get the crystals on the grid while minimizing the amount of solvent that crystallizes as the sample dries.

38. Grasp the edge of the grid in a pair of reverse action tweezers or tweezers that can be held shut with an O-ring. Balance the tweezers on an elevated surface, like a tube rack.

39. Pipet 1 to 5 µL of sample onto the front face of the grid.
40. (Optional) Incubate the sample on the grid for 0 to 60 seconds.
41. Allow the sample to dry. Excess liquid can be blotted away using filter paper, or the sample can evaporate on its own. Buffer components may also crystallize depending on the composition and purity of the sample. The grid can be moved so that evaporation occurs on the benchtop, in a desiccator, under vacuum, or in an inert atmosphere as necessary. Let the sample dry completely before use or storage.
42. Dry small molecule solid state samples can be used immediately or stored prior to MicroED data collection. Grids can be stored under ambient laboratory conditions or in a controlled environment like a dry box or desiccator.
43. Dry solid state samples can be directly loaded into the microscope without prior cooling, or the grid can be plunged into liquid nitrogen before loading into a cooled autoloader. If excess solvent remains, the sample grid can be incubated in a vacuum desiccator or a vacuum oven (~40°C) for 15 to 30 minutes before loading into the microscope[154].

Option E: Grow crystals on the grid as suspended drops

Physically transferring the crystal sample to the grid and blotting using conventional MicroED sample preparation protocols can be difficult steps and may introduce significant bottlenecks in the workflow. This is especially true for highly viscous crystal drops. Moreover, crystals sensitive to stress may be damaged and certain crystals may exhibit a preferred orientation on the grid support surface, limiting the amount of reciprocal space available for data collection. In suspended drop crystallization[140], the crystal transfer and blotting steps in the workflow can be bypassed. Here, the crystallization drop is incubated on a low mesh count grid with no additional sample

support layers (support-free grids). The crystals are finally frozen on the support-free grid for subsequent FIB milling and MicroED **(Figure 3.8)**.

44. Clip a low mesh count (50-150 mesh) support-free gold gilder grid into an autogrid cartridge (Thermo Fisher) and glow discharge to clean the surface (see above *Prepare TEM grids for MicroED*). Gold grids are preferred because they are chemically inert. Lower mesh grids make it easier to visualize crystals by light or UV microscopy, and crystals are less likely to be obstructed by grid bars during subsequent FIB filling.
45. Mount the cartridge into a cartridge holder tool. Dispense the sample and crystallization mother liquor onto the support-free grid (Figure 3.8). It is important to make the drop small enough so that it does not touch the inner wall of the autogrid cartridge to avoid copper ion contamination. A final drop volume of 0.2 – 0.5 μL is suitable.

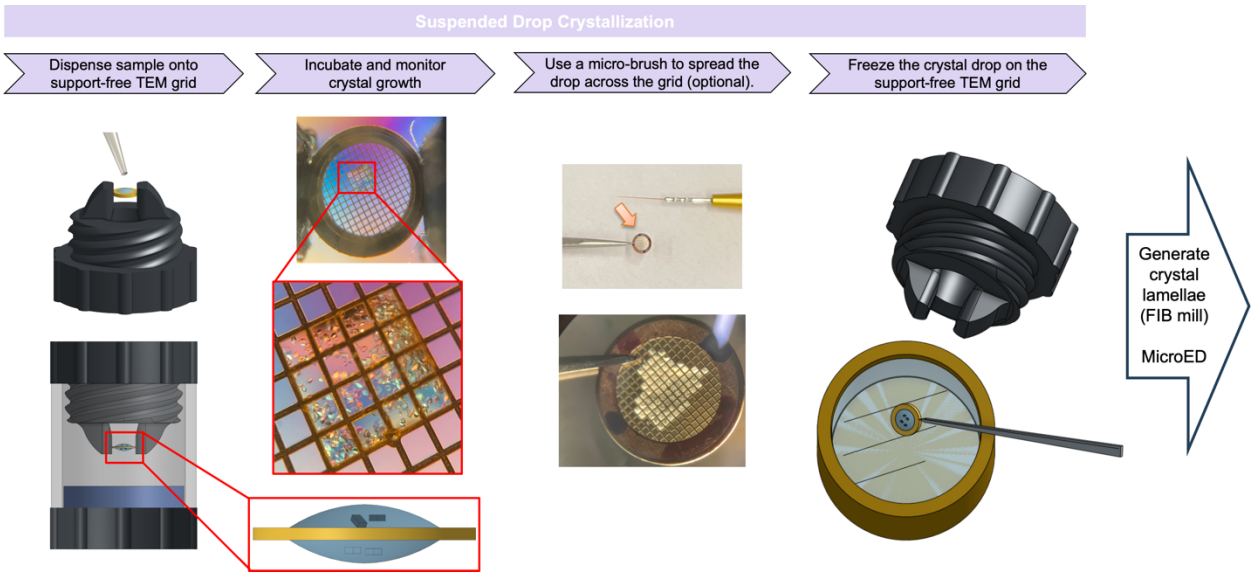

Figure 3.8. Growing crystals on the TEM grid by suspended drop crystallization. An autogrid cartridge containing a support-free grid is mounted in the autogrid mounting tool and sample is dispensed onto the grid surface. The suspended drop is incubated in a mother liquor well for vapor diffusion to occur. To thin the sample prior to freezing, use a micro-brush tool to spread the crystal drop across the surface. Cryo-preserve by rapidly plunging into liquid nitrogen or ethane prior to FIB milling and MicroED[140].

46. (Optional) If dispensing small volumes of sample onto the grid is problematic, the crystal drop can be transferred to the gold gilder grid by touching the grid with the surface of the drop. Prepare a 0.5 – 1 μL crystal drop on a clear glass slide. Use tweezers to grasp the rim of the autogrid and gently touch the gold gilder grid to the top of the drop while avoiding contact with the autogrid. A small amount of the drop will transfer to the grid when contact is broken. Another option is to touch the end of a pipet tip containing sample to the grid and a minimal amount will be transferred.
47. Immediately seal the mounted autogrid into a crystallization well containing mother liquor and incubate (Figure 3.8). Monitor for crystal growth by light or UV microscopy.
48. Retrieve the autogrid cartridge containing crystals using tweezers.
49. (Optional) To make the sample thinner, spread the drop across the grid surface to cover more area. Grasp the edge of the grid using reverse action tweezers. Under a light microscope, use a micro-brush tool to push the drop around (Figure 3.8).
50. Rapidly plunge-freeze into liquid nitrogen or ethane (Figure 3.8). Store
51. Proceed to step 60 to perform FIB milling to generate crystal lamellae that access crystals through the surrounding crystallization media Also refer to the FIB milling procedures described in other publications for targeted milling of deeply submerged crystals using an integrated fluorescence light microscope[138,140].

Option F: Thinning membrane protein crystals embedded in LCP using a plasma focused ion beam (pFIB).

Pairing FIB milling to generate thin crystal lamella with MicroED has unlocked many new avenues for MicroED[155]. It is possible to collect MicroED data even from macromolecules like proteins to sub-atomic resolution (better than 1 Å) using FIB-milled crystals[156]. If the crystallization media can flow, crystal samples can be applied to a TEM grid and blotted as normal before FIB milling (Figure 3.5)[32,35,82,96,135,155,157–160]. For crystal samples

amenable to blotting, gallium ion FIBs have been used to successfully prepare sample lamellae for the subsequent MicroED structure determination of soluble proteins[140,156] and membrane proteins in LCP sponge phase[161] and bicelle media[137]. In these works, crystal topological features and grid bars could be observed using the FIB and SEM modes of imaging in the milling instrument, which is necessary for crystal targeting. In the protocol published by Martynowycz and Gonen in 2021, a standard workflow for generating crystal lamellae using FIB-SEMs equipped with a gallium ion source is described[82]. In contrast, membrane protein crystals embedded in the lipidic cubic phase (LCP) are highly viscuous and cannot be blotted. The deposited LCP preparations can be several hundred microns in thickness and somewhere inside nanocrystals could be buried. We have found that milling through this large amount LCP using a gallium ion FIB is ineffective as the LCP appears to deform and melt, destroying the sample in the process.

To prepare sample lamellae that expose crystals deeply embedded in LCP matrix for MicroED, we developed a correlative light-EM and milling procedure that implements a plasma beam FIB (pFIB), which is more rapid and less damaging than gallium ion FIBs[138,162]. The pFIB/SEM milling instrument employed for these experiments is the cryogenically cooled Helios Hydra 5 CX dual-beam (Thermo Fisher) instrument equipped with Argon, Xenon, Oxygen, and Nitrogen plasma ion sources. We showed that the Argon and Xenon ion sources can mill through large amounts of LCP material efficiently without compromising the integrity of the sample[138]. Because the deposited LCP crystals are submerged below the surface of the sample, it is necessary to label the protein of interest with a fluorescent marker that can be detected by an integrated fluorescent light microscope (iFLM)[163] installed on the Hydra. Labeling with a fluorescent dye prior to

crystallization in LCP and using the iFLM has enabled us to target submerged crystals with the pFIB and collect MicroED data to determine high-resolution structures of membrane proteins preserved in that were previously unattainable[138,139]. A similar workflow was adapted for the development of suspended drop crystallization[140], wherein crystal samples are grown on a support-free TEM grid and blotting of the sample prior to freezing is bypassed.

Here, we outline a detailed procedure for targeted pFIB milling of membrane protein crystals embedded in LCP matrix using a Helios Hydra 5 CX pFIB/SEM equipped with an iFLM for MicroED data acquisition.

52. Label the membrane protein of interest with a fluorescent dye prior to LCP crystallization. Labeling the protein will make it possible to detect crystals using the iFLM. The iFLM operates in either reflective mode or fluorescent mode. There are four different wavelengths to choose from in fluorescent mode (λ = 385, 470, 565, 625 nm). Highly reactive *N*-hydroxysuccinimide (NHS) esters have been used for labeling LCP crystals before crystallization and lamella milling for MicroED[138,139,164]. However, the most suitable dye for the protein of interest may need to be empirically determined.

    (Tip) In some cases, it may be possible to detect crystals by fluorescence without labeling. Imaging trials may be performed to determine if the unlabeled crystals emit a strong enough signal to be detected using the iFLM at different excitation wavelengths.

53. Crystallize the labeled membrane protein of interest. The protocol for LCP crystallization by Caffrey and Cherezov, 2009, may be referenced[165].

54. Prepare the sample preparation workstation: crystals in LCP are highly susceptible to dehydration damage. It is critical for LCP crystal sample looping and transfer to happen in a highly humidified environment. Place a humidifier next to the light microscope that will be used during sample preparation and direct a steady flow of water vapor at the LCP plate.

    We always prepare LCP samples with two people. One person holds the clipped grid with autogrid tweezers while the other works under the light microscope to transfer the LCP sample from the sandwich plate to the grid. Working quickly and efficiently to minimize environmental exposure of the LCP sample is essential.

55. Clip the grids into autogrid clips that have one permanent marker dot on the rim (Figure 3.9b). This marking is used when loading the pFIB/SEM and the TEM to ensure the lamellae will be at the proper orientation relative to the TEM stage tilt axis. The C ring will be clipped on the copper/back face of the grid. The front face of the grid should be facing down when clipping the grids**.** Optionally apply more distinguishable dots along the rim of the autogrid at the 3, 6, and/or 9 o'clock positions. This may be helpful if the dots fade after repeated use in the microscopes.

    Most Thermo Fisher cryogenic milling instruments use grids clipped into autogrids (Figure 3.9a). Specialized autogrid clips have been designed to mill at shallow angles for tomography experiments. Crystals for MicroED can be milled at high or shallow angles using standard or specialized autogrid clips, respectively.

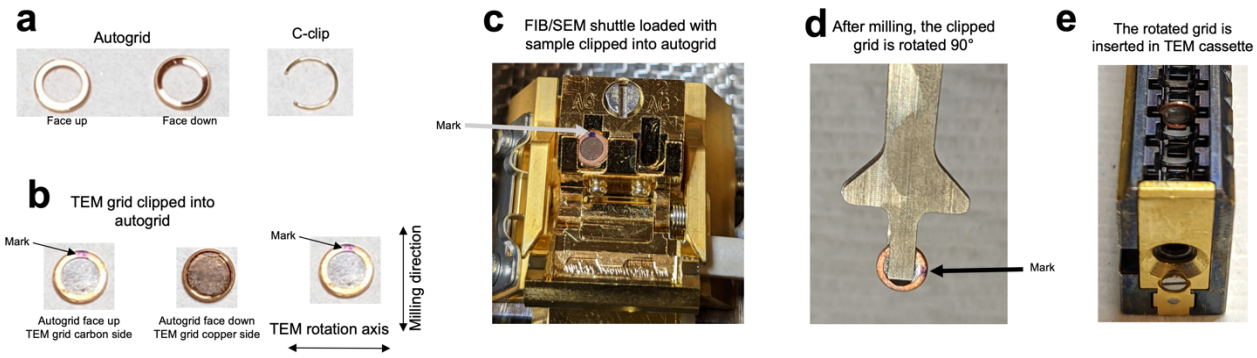

Figure 3.9. How to handle TEM grids when FIB milling crystals. (a) The TEM grid is placed inside an autogrid. A C-clip is inserted inside the autogrid to sandwich and retain the grid. (b) The flat face of the autogrid is marked to indicate the FIB milling direction, which is perpendicular to the TEM rotation axis. (c) The autogrid is placed inside the FIB/SEM transfer shuttle with mark facing up. The shuttle is then loaded inside the FIB/SEM instrument. (d) Post-milling, autogrid tweezers are used to rotate the autogrid 90 degrees under cryogenic conditions. The rotation degree is indicated by the mark. After rotating, the autogrid is inserted directly into the TEM cassette (e).

Grid bars can obstruct potential crystal targets. Unlike the gallium ion FIB, it is possible to mill through grid bars to expose the bottom of the lamella using high milling currents. However, it is preferable to avoid depositing extra energy into the sample for this purpose. We recommended using 200 mesh holey carbon grids to reduce the chances of grid bar interference.

56. Glow discharge the clipped grids for 30 s at 15 mA on the negative setting immediately before sample preparation.
57. Place the LCP glass sandwich plate under the light microscope.
58. Use a tungsten carbide pen to etch a square around the drop of interest and carefully cut through the top piece of the sandwich plate using a razor blade. Lift the glass

square open using the edge of the razor blade. If the square is not completely separated from the plate, rest the razor blade on the square after flipping it over to hold it down (Figure 3.10a).

59. Loop the LCP-crystal glob from the LCP sandwich plate using a 50 – 100 µm nylon crystallography loop or a similarly sized MiTeGen dual thickness micro mount (Figure 3.10b).
60. Plunge the grid into liquid nitrogen or ethane. We typically use liquid nitrogen when manually plunging the sample because it is easier and safer to work with. Store the sample under liquid nitrogen prior to further experiments (Figure 3.10c).

-Pause point-

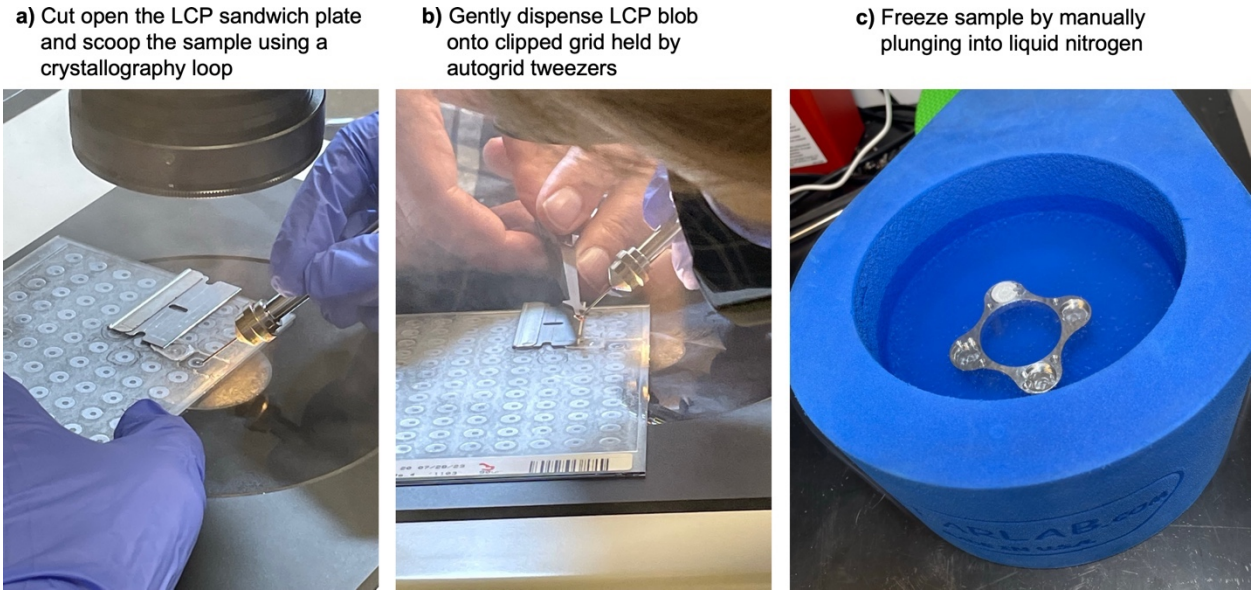

Figure 3.10. LCP crystal sample preparation.

61. (optional) Screen the grids using a Thunder cryogenic light microscope (Leica Microsystems) to identify grids suitable for milling (Figure 3.11a). In the ideal sample, the height of the LCP glob will not exceed 100 µm and there will be many fluorescently labeled crystals in clear view and away from grid bars. Milling through more than 100 µm height of material is time-consuming, and crystal targeting is less accurate. While it is possible to mill crystals directly over grid bars with the pFIB (procedure described below), it is advisable to avoid grid bar milling if possible. Record the X-Y positions of regions of interest for subsequent targeting on favorited grids.

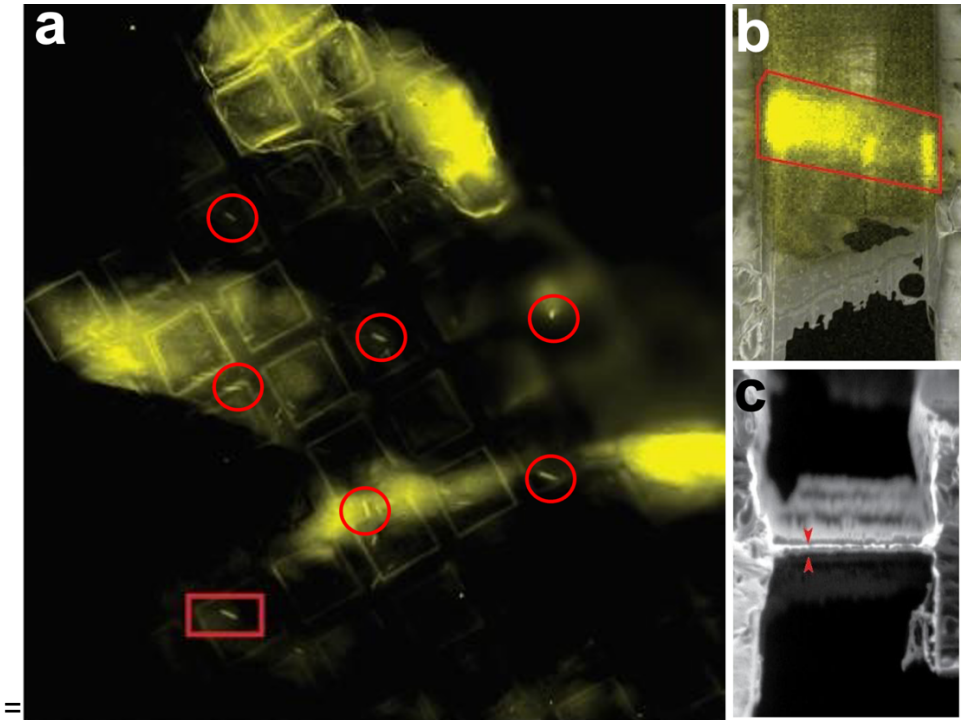

Figure 3.11. LCP crystal lamella targeting. (a) A whole-grid fluorescent map of the LCP glob on the TEM grid was acquired in a Thunder imager to determine where fluorescently labeled membrane protein crystals (red circles) are located. A crystal that emits strong signal and located in the center of a grid square is targeted for pFIB milling (red square). (b) iFLM image of the final milled lamella confirms the targeted crystal is present. (c) The milled lamella (red arrows) imaged from the pFIB milling angle.

62. Prepare, pre-cool and align the pFIB/SEM following manufacturer instructions.
63. Load the grids into the Hydra pFIB/SEM transfer shuttle following manufacturer instructions.
    a. Use liquid nitrogen to cool the transfer shuttle transfer station.
    b. Loosen the screw on the pFIB/SEM transfer shuttle that locks the grids in place.
    c. The pFIB/SEM transfer shuttle can accommodate two grids. Slide the clipped grid into a grid slot with the front face of the grid (where the sample was applied) facing out (Figure 3.9c). If necessary, rotate the grid in the shuttle so the permanent marker dot is in the 12 o'clock position.
    d. Load a second grid if desired.
    e. Tighten the screw to lock the shuttle.
64. Follow manufacturer instructions to load the shuttle into the microscope. Allow the vacuum and temperature to stabilize after loading.
65. Apply a protective coat of platinum to the crystal sample to limit damage during the milling process. The LCP glob is coated with a layer of a volatile carbon-rich platinum using the gas injection system (GIS) prior to pFIB milling. To apply a GIS platinum coating, move to the mapping position with a 12 mm working distance and deposit platinum over 30 seconds to yield approximately 1 μm of GIS coating. The SEM can be used to monitor the thickness of the GIS coating.
66. The GIS protective layer is an insulator, and over the course of milling will likely become charged. This results in imaging artifacts that make distinguishing features of the lamellae being milled difficult because there is little to no contrast. Our current

strategy for mitigating platinum charging effects is exposing the milling site and surrounding GIS layer with the pFIB set to ~0.5 nA until the contrast flips. The GIS layer will protect the sample during this process.

67. (optional) In addition to GIS, the milling instrument may also be equipped with a sputter coater that deposits grains of platinum. The protective platinum is applied in a series of steps, starting with sputter coating a fine and then a rough layer[82]. Aim for a 50 - 350 nm thick layer and deposit it first as a fine coat (1 kV 7 mA 30-60 seconds) then as a rough coat (1 kV 30 mA 30-60 seconds).

    While applying a combination of sputter coating and GIS will increase milling time, the stability of the sample will be enhanced.[166,167]. Moreover, the platinum sputter coating will make the sample conductive, reduce charging effects caused by the GIS, reduce the formation of curtains during milling, and increase the structural integrity of the grid[166–169].

(Caution) Both the GIS and sputter coating processes can increase the stage temperature, leading to sample de-vitrification. To counteract this increase, increase the flow of the nitrogen gas that cools the stage protective layer application.

68. Find the rough eucentric height of the sample. Center the SEM on a feature at the surface, such as ice, and tilt the stage 5°. Adjust the Z height of the sample until the feature is centered again. Continue tilting in 5° increments and adjusting the Z height until the feature stays centered at various tilt angles.
69. Evaluate the grid by taking an atlas using the SEM using the latest version of MAPS software (Thermo Fisher). Crystals are typically submerged in the LCP glob, and it is

impossible to observe crystal topological features at the glob surface. Use MAPS software to refine the eucentric height of the sample.

70. Identify LCP crystal targets using the iFLM to determine x,y and z positions for milling. Set the iFLM to the proper fluorescence excitation wavelength for the protein label used. Scan the sample with the iFLM in live mode until a crystal region has been identified. Center the crystal and switch to the iFLM reflective cube. Adjust the Z height of the iFLM to determine the approximate top and bottom Z-dimensions of the LCP blob, indicated by grid bars and the glob surface coming into focus, respectively. Use these Z-dimensions to acquire a stack at 1μm Z-steps. Repeat the Z-stack acquisition using the fluorescent cube. The depth of the crystal below the surface of the glob is determined by identifying where in the Z-stack the crystal comes into focus. Use this information for subsequent pFIB targeting.

Although it is possible to mill through grid bars using a pFIB (described below) it is recommended to aim for targets close to the center of a grid square to avoid complications related to grid bar removal.

71. Plan out the milling session.

    f. Contamination and ice will build up on the sample while it is in the pFIB/SEM instrument, so the total experiment time should be minimized. The rate of ice buildup should be assessed for the instrument and influences the total length of the microscope session. In our Hydra milling instrument, operating at optimal vacuum and temperature, ice builds up about 2-10 nm/hr.

g. Consider how many putative crystals to target over the session. Fully preparing one lamella through LCP can take 4-8 hours, depending on the thickness of the sample and how difficult targeting is (e.g., for smaller crystals).

h. Smaller crystals require more careful monitoring and can take additional time to finish.

i. Determine the appropriate milling angle for your sample. Using standard autogrid clips, the milling angle will be high. For a given target, higher milling angles lead to shorter lamellae, while shallower milling angles lead to longer lamellae. The dimensions of the target also influence the possible lamellae lengths. A typical milling angle for MicroED is 18°.

j. Determine the appropriate lamella width for your sample. Wider lamellae provide a larger field of view in subsequent TEM, but are more likely to break or distort during transfer to the TEM.

k. Each lamella can be fully milled, or different milling stages can be batched together. For batching, first perform rough milling for each target, then fine milling, and finally polishing for each lamella. Batching requires more user effort and can reduce contamination.

72. Return to the x, y, z coordinates of the crystal. Confirm that the pFIB and SEM beams are properly aligned by comparing if they are centered on the same area when imaging. If they are not properly aligned, refine the eucentric height manually and/or repeat the eucentric height calculation in MAPS software.

73. See Figure 3.12 for an overview of the steps to take for LCP crystal milling. Also in Figure 3.12, the settings to use for both Xenon and Argon plasma ion beams at different milling stages are listed and strategic considerations are indicated.
74. Start lamella production by milling a trench that will remove both the surface of the LCP glob and material above the crystal. For this, draw a milling box 10 to 30 µm thick and 10 to 20 µm wide and use rough milling settings at a high ion-beam current (Figure 3.12, step 1). Monitor the milling progress by periodically pausing the milling current

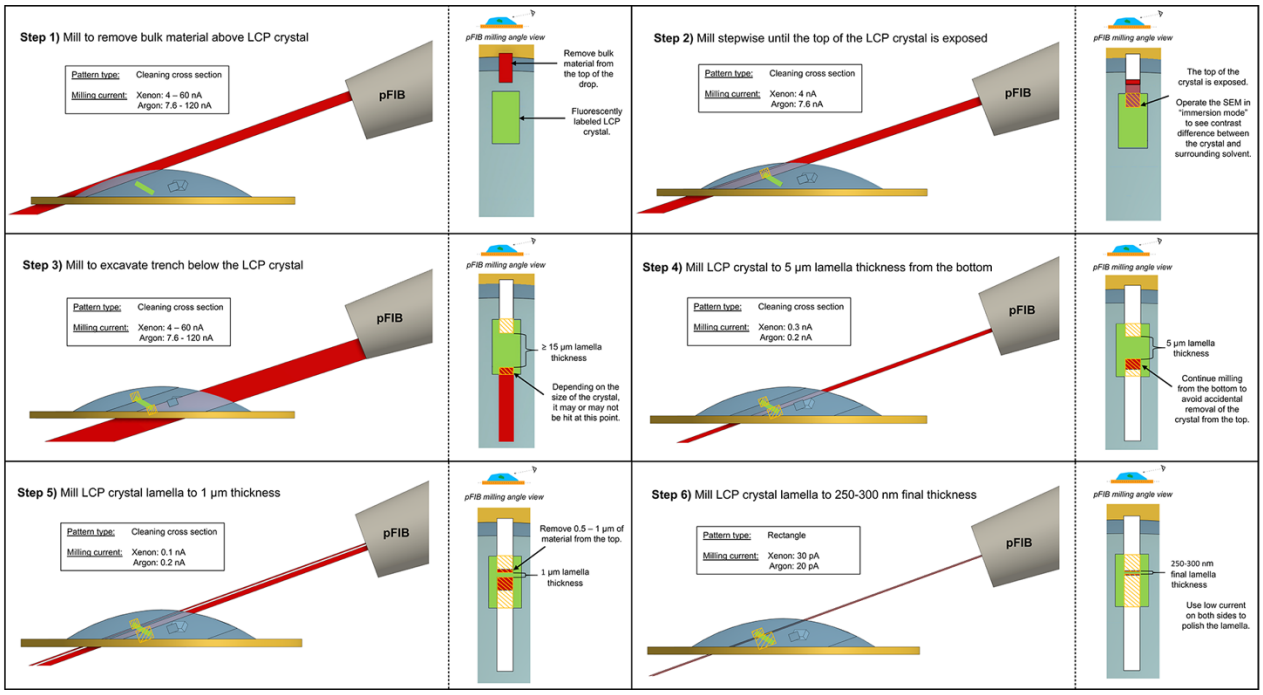

Figure 3.12. Strategy and pFIB beam settings to use for milling LCP crystals. In each panel, the drop (blue) is viewed parallel to the grid support surface (gold) and from the pFIB milling angle view. The size of the crystal (green) is exaggerated in the models. The portions of the crystal that are milled away by the pFIB beam (red) during each step are indicated (orange boxes with diagonal hatching).

and imaging with the SEM. After the initial rough mill is complete, proceed by stepping down the topside milling box in increments while gradually reducing the milling current to prevent depositing damaging energy into the approaching crystal (Figure 3.12, step 2).

(Critical step) Frequently image the top of the lamella using low voltage SEM (0.9 - 1.2 kV) with the through lens detector (TLD). These settings define the “Immersion mode” preset. With these settings applied, it is possible to observe the contrast difference between the crystal and the surrounding LCP media. Note that SEM alignment needs to be redone when switching to the TLD and immersion mode. Also, image the lamella between mills using the iFLM. The crystal fluorescent signal will become significantly stronger when it is finally exposed from the top.

(Caution) Some sample drift can occur during milling. Realign as necessary between milling steps.

75. Once the crystal target is finally exposed from the top, stop milling from the top and begin excavating the bottom lamella trench using rough milling settings and boxes sized similar to those used for the top of the lamella in the previous step (Figure 3.12, step 3).

If it is not possible to avoid grid bars, apply the following procedure: Draw as small of a box as possible to dig a trench beneath the crystal that goes through the grid bar and set the milling distance in the z direction to 300 μm deep and milling current to >100 nA. Keep the high current beam as far away from the crystal as possible and focus on only the removal of the bar.

(Caution) Do not image with the pFIB at >100 nA, as it will damage the detector. Turn off the live update and in-box imaging while using these currents. The drawn milling box must be overlaid on an image taken at a lower ion current. Because shifts can sometimes occur when shifting from low to high currents, this procedure may sometimes fail as the box drifts away from the target.

76. After the rough mill of the bottom lamella trench is complete, continue stepping the bottom milling pattern up while gradually reducing the milling current to reduce the thickness of the lamella further (Figure 3.12, steps 4-5). Since the location of the crystal in the lamella is known at this point, optionally reduce the size of the milling box to make the lamella narrower.
77. Use the rectangle milling pattern function with a low ion-beam current (1.5-30 pA) to polish the fine lamella to the desired final dimensions (Figure 3.12, step 6). With the rectangle pattern, a live view of the milling progress can be observed. Monitor the progress carefully and immediately stop the milling current once all material inside the box has been remove. The lamella is especially sensitive at this stage and milling time should be minimized. To optimize the quality of the MicroED data obtained from crystal lamellae, the ideal sample thickness for macromolecular protein samples has been determined[96]. Crystal lamellae are typically milled ~300 nm thick before performing MicroED.
78. (Optional) Image the final lamella with the iFLM to confirm the crystal is still present (Figure 3.11b).
79. Confirm the polishing results and measure the resulting lamella thickness to confirm it is the desired thickness. Use the ion beam at 1.5 pA to examine the final lamella

(Figure 3.11c). Imaging with a lower current at the final stage is recommended as the thin lamella is sensitive to damage.

80. Unload the grids and transfer them to a TEM to collect diffraction data. The autogrid should have a mark indicating the direction of the ion beam. When loading the autogrid into the TEM, the grid should be rotated such that the lamellae are oriented perpendicular to the TEM rotation axis; on our instrument, this requires a 90° rotation of the grid (Figure 3.9c-e).

Collect MicroED Data

After sample preparation, grids are loaded into a TEM for examination. A low magnification atlas is used to identify promising grid squares with putative crystals. The eucentric height is determined for each putative crystal, and a still diffraction image is collected to assess diffraction quality. A movie of MicroED diffraction data is collected for promising crystals. The stage is limited to a -70° to +70° sweep on most standard TEMs. After collecting the data, the images are converted into a compatible format and processed using standard X-ray crystallography software. Data collection and processing is described in several papers[44,45,85,86,154,157–162]

Troubleshooting

Common MicroED sample preparation issues and potential solutions are summarized in Table 3.3.

Anticipated results

Optimal grids for MicroED should contain multiple crystals in various orientations and be frozen in a thin layer of vitreous ice. If a dried sample is prepared, the crystals should be in multiple orientations and not obscured by solvent crystals. Crystals should be readily distinguished from the background. If the crystals are in thick ice, the contrast will be reduced. Crystals could be

diluted before freezing, or additional blotting time could be added. If the sample is too thick, it can be dealt with by diluting it, blotting longer, fragmenting the crystals, or preparing a thin lamella using FIB milling.

There should be enough space between crystals that a dataset can be collected for a given crystal without the interference of the diffraction pattern of a nearby crystal. Crystals that are clumped can be disrupted by fragmentation or dilution (Figure 3.3).

Crystals should displace discrete, symmetric spots when diffraction data is collected. If crystals are imperfect, disordered, defective, impure, or damaged, they can display streaky, smeared, or split reflections[176]. Crystals may be twinned, or multiple crystals may be diffracting.

With these strategies, high-quality MicroED data can be collected and used to solve high-resolution structures of a variety of macromolecules and small molecules.

Acknowledgments

We thank William Nicolas (HHMI) for useful discussions. This study was supported by the National Institutes of Health P41GM136508 and the Department of Defense HDTRA1-21-1-0004. CG was funded by NIH-NIAMS T32AR065972.The Gonen laboratory is supported by funds from the Howard Hughes Medical Institute.

Table 3.3. Troubleshooting MicroED Sample Preparation.

Steps	Problem	Possible Reason	Solution
14-18	No crystals on grid	Low crystal concentration in the sample	Apply sample multiple times Concentrate sample
		Crystals adhere to the screening plate and/or the pipet tip inner surface	Pipet larger volume to grid Grow crystals on grid as suspended drop
16	Crystals are dry	Blotting is to aggressive	Blot for less time or fewer blots Sugar embedding with trehalose can be used to preserve delicate crystals by reducing dehydration and acting as a cryoprotectant[2,11,52,66–72] Crystals may be sandwiched between carbon films to reduce dehydration during blotting[69,73] Grow crystals on grid as suspended drop
18	Overlapping diffraction patterns	Crowded crystals on grid	Fragment crystals (see Info box of Fragmenting crystals) Dilute crystals during grid preparation Pipet less volume to grid

14-15	Thick ice prevents electron transmission	Insufficient blotting	Blot more (duration or number of blots) Dilute sample during grid preparation Pipet less volume to grid Blot from both front and back faces Perform manual blotting (see Info box on Manual blotting) FIB mill
25, 32	Thick crystals prevent electron transmission	Crystals were allowed to grow to a thickness that is greater than the mean free path of electrons[162,179–183]	Fragment crystals FIB mill
18, 38	Buffer components crystallize	Buffer concentration too high Crystals are grown in a high salt condition	Wash crystals on grid Dilute sample Pressure-assisted blotting[127]
30-34	Contamination from previous experiments	Poor workspace cleanliness Loosely associated powders fall off during grid transfer If using a microscope with an autoloader,	Work with a minimal amount of sample Wipe tools with ethanol and kimwipe after handling the sample Clean the microscope cassette according to manufacturer instructions

		powders may fall off and accumulate in the cassette.	
13, 15, 26	Crystals are damaged	Pipetting and/or fragmentation disrupted crystal integrity	FIB mill instead of fragment Touch grid to crystal drop instead of pipetting drop onto grid Grow crystals on grid as suspended drop
22	Ice contamination on grid	Breathing onto the sample Allowing the sample to sit outside storage containers too long Liquid nitrogen storage contaminated	Wear a mask during grid prep Minimize time in transfer and loading station Minimize time in storage dewar
33	Smeared or split reflections in the diffraction pattern	Crystals are imperfectly ordered or damaged	Fragment imperfect crystals Screen additional crystallization conditions
51	Crystals destroyed by FIB	The protective layer of platinum is too thin	Deposit a thicker platinum coating prior to milling
6, 15-16	The grid is too hydrophobic (Figure 5e, f)	Insufficient glow discharging	Vary the process time (typically ranging from 15 to 120 seconds) and the current (typically 15 to 60 mA)
17, 28	The grid is bent	Grid was damage during preparation	Decrease the blotting force

			Avoid applying excessive force to the grid during sample application
27	LCP crystals are not distinguishable in the drop when using a cross-polarized light microscope.	The LCP phase converted to the lamellar phase that gives a bright cross-polarized signal	Make sure that the relative humidity is above 85% whenever working with LCP samples Check that the lipid mixture is dry and does not have a trace of solvent PEG400 can dilute the lamellar phase and convert it into the sponge phase[163,184]
26	After the addition of PEG400, cholesterol crystals appear.	The concentration of cholesterol is too high	Freeze within 3 min after mixing with PEG-400 before cholesterol crystals can form Carry out the sample preparation procedure at 17-20°C Use a lipid mixture with lower cholesterol content (5-8%) for crystallization

References

1. Kuang, Q. *et al.* Dead-end complex, lipid interactions and catalytic mechanism of microsomal glutathione transferase 1, an electron crystallography and mutagenesis investigation. *Sci. Rep.* **7**, 7897 (2017).
2. Gonen, T. *et al.* Lipid-protein interactions in double-layered two-dimensional AQP0 crystals. *Nature* **438**, 633–638 (2005).
3. Hiroaki, Y. *et al.* Implications of the aquaporin-4 structure on array formation and cell adhesion. *J. Mol. Biol.* **355**, 628–639 (2006).
4. Oshima, A., Tani, K., Hiroaki, Y., Fujiyoshi, Y. & Sosinsky, G. E. Three-dimensional structure of a human connexin26 gap junction channel reveals a plug in the vestibule. *Proc. Natl. Acad. Sci.* **104**, 10034–10039 (2007).
5. Oshima, A. *et al.* Asymmetric configurations and N-terminal rearrangements in connexin26 gap junction channels. *J. Mol. Biol.* **405**, 724–735 (2011).
6. Matricardi, V. R., Moretz, R. C. & Parsons, D. F. Electron Diffraction of Wet Proteins: Catalase. *Science* **177**, 268–270 (1972).
7. Hui, S. W. & Parsons, D. F. Electron diffraction of wet biological membranes. *Science* **184**, 77–78 (1974).
8. Dorset, D. L. & Parsons, D. F. Electron diffraction from single, fully-hydrated, ox-liver catalase microcrystals. *Acta Crystallogr. Sect. A* **31**, 210–215 (1975).
9. Dorset, D. L. *Structural Electron Crystallography*. (Springer US, 1995). doi:10.1007/978-1-4757-6621-9.
10. Dorset, D. L. & Gilmore, C. J. Direct methods in protein electron crystallography – beef liver catalase in its fully hydrated form at room temperature. *Acta Crystallogr. A* **55**, 448–456 (1999).
11. Unwin, P. N. & Henderson, R. Molecular structure determination by electron microscopy of unstained crystalline specimens. *J. Mol. Biol.* **94**, 425–440 (1975).
12. Henderson, R. *et al.* Model for the structure of bacteriorhodopsin based on high-resolution electron cryo-microscopy. *J. Mol. Biol.* **213**, 899–929 (1990).

13. Taylor, K. A. & Glaeser, R. M. Electron Diffraction of Frozen, Hydrated Protein Crystals. *Science* **186**, 1036–1037 (1974).

14. Jeng, T.-W. & Chiu, W. Experimental strategy in three-dimensional structure determination of crotoxin complex thin crystal. *Ultramicroscopy* **13**, 27–34 (1984).

15. Stokes, D. L. & Green, M. N. Structure of CaATPase: Electron microscopy of frozen-hydrated crystals at 6 Å resolution in projection. *J Mol Biol* **213**, 529–538 (1990).

16. Martynowycz, M. W. & Gonen, T. From electron crystallography of 2D crystals to MicroED of 3D crystals. *Curr. Opin. Colloid Interface Sci.* **34**, 9–16 (2018).

17. Garman, E. F. & Weik, M. Radiation Damage in Macromolecular Crystallography. *Methods Mol. Biol. Clifton NJ* **1607**, 467–489 (2017).

18. Holton, J. M. & Frankel, K. A. The minimum crystal size needed for a complete diffraction data set. *Acta Crystallogr. D Biol. Crystallogr.* **66**, 393–408 (2010).

19. Sanishvili, R. *et al.* Radiation damage in protein crystals is reduced with a micron-sized X-ray beam. *Proc. Natl. Acad. Sci.* **108**, 6127–6132 (2011).

20. Terwilliger, T. C., Stuart, D. & Yokoyama, S. Lessons from structural genomics. *Annu. Rev. Biophys.* **38**, 371–383 (2009).

21. Carpenter, E. P., Beis, K., Cameron, A. D. & Iwata, S. Overcoming the challenges of membrane protein crystallography. *Curr. Opin. Struct. Biol.* **18**, 581–586 (2008).

22. Zatsepin, N. A., Li, C., Colasurd, P. & Nannenga, B. L. The complementarity of serial femtosecond crystallography and MicroED for structure determination from microcrystals. *Curr. Opin. Struct. Biol.* (2019) doi:10.1016/j.sbi.2019.06.004.

23. O'Dell, W. B., Bodenheimer, A. M. & Meilleur, F. Neutron protein crystallography: A complementary tool for locating hydrogens in proteins. *Arch. Biochem. Biophys.* **602**, 48–60 (2016).

24. Shi, D., Nannenga, B. L., Iadanza, M. G. & Gonen, T. Three-dimensional electron crystallography of protein microcrystals. *Elife* **2**, e01345 (2013).

25. Nannenga, B. L., Shi, D., Leslie, A. G. W. & Gonen, T. High-resolution structure determination by continuous-rotation data collection in MicroED. *Nat. Methods* **11**, 927–930 (2014).

26. Nannenga, B. L., Shi, D., Hattne, J., Reyes, F. E. & Gonen, T. Structure of catalase determined by MicroED. *eLife* **3**, e03600 (2014).

27. Yonekura, K., Kato, K., Ogasawara, M., Tomita, M. & Toyoshima, C. Electron crystallography of ultrathin 3D protein crystals: Atomic model with charges. *Proc. Natl. Acad. Sci.* **112**, 3368–3373 (2015).

28. de la Cruz, M. J. *et al.* Atomic-resolution structures from fragmented protein crystals with the cryoEM method MicroED. *Nat. Methods* **14**, 399–402 (2017).

29. Clabbers, M. T. B. *et al.* Protein structure determination by electron diffraction using a single three-dimensional nanocrystal. *Acta Crystallogr. Sect. Struct. Biol.* **73**, 738–748 (2017).

30. Zhou, H. *et al.* Programming Conventional Electron Microscopes for Solving Ultrahigh-Resolution Structures of Small and Macro-Molecules. *Anal. Chem.* **91**, 10996–11003 (2019).

31. Xu, H. *et al.* Solving a new R2lox protein structure by microcrystal electron diffraction. *Sci. Adv.* **5**, eaax4621 (2019).

32. Beale, E. V. *et al.* A Workflow for Protein Structure Determination From Thin Crystal Lamella by Micro-Electron Diffraction. *Front. Mol. Biosci.* **7**, 179 (2020).

33. Clabbers, M. T. B. *et al.* MyD88 TIR domain higher-order assembly interactions revealed by microcrystal electron diffraction and serial femtosecond crystallography. *Nat. Commun.* **12**, 2578 (2021).

34. Martynowycz, M. W., Clabbers, M. T. B., Hattne, J. & Gonen, T. Ab initio phasing macromolecular structures using electron-counted MicroED data. *bioRxiv* (2021) doi:10.1101/2021.10.16.464672.

35. Zhou, H., Luo, Z. & Li, X. Using focus ion beam to prepare crystal lamella for electron diffraction. *J. Struct. Biol.* **205**, 59–64 (2019).

36. Nannenga, B. L. & Gonen, T. The cryo-EM method microcrystal electron diffraction (MicroED). *Nat. Methods* **16**, 369–379 (2019).

37. Henderson, R. The potential and limitations of neutrons, electrons and X-rays for atomic resolution microscopy of unstained biological molecules. **28**, 171–93 (1995).

38. Leslie, A. G. W. The integration of macromolecular diffraction data. *Acta Crystallogr. D Biol. Crystallogr.* **62**, 48–57 (2006).

39. Kabsch, W. Integration, scaling, space-group assignment and post-refinement. *Acta Crystallogr. D Biol. Crystallogr.* **66**, 133–144 (2010).

40. Kabsch, W. XDS. *Acta Crystallogr. D Biol. Crystallogr.* **66**, 125–132 (2010).

41. Sheldrick, G. M. A short history of *SHELX*. *Acta Crystallogr. A* **64**, 112–122 (2008).

42. Adams, P. D. *et al.* PHENIX: a comprehensive Python-based system for macromolecular structure solution. *Acta Crystallogr. D Biol. Crystallogr.* **66**, 213–221 (2010).

43. Winn, M. D. *et al.* Overview of the CCP4 suite and current developments. *Acta Crystallogr. D Biol. Crystallogr.* **67**, 235–242 (2011).

44. Hattne, J. *et al.* MicroED data collection and processing. *Acta Crystallogr. Sect. Found. Adv.* **71**, 353–360 (2015).

45. Clabbers, M. T. B., Gruene, T., Parkhurst, J. M., Abrahams, J. P. & Waterman, D. G. Electron diffraction data processing with DIALS. *Acta Crystallogr. Sect. Struct. Biol.* **74**, 506–518 (2018).

46. Winter, G. *et al.* DIALS: implementation and evaluation of a new integration package. *Acta Crystallogr. Sect. Struct. Biol.* **74**, 85–97 (2018).

47. Iadanza, M. G. & Gonen, T. A suite of software for processing MicroED data of extremely small protein crystals. *J. Appl. Crystallogr.* **47**, 1140–1145 (2014).

48. Battye, T. G. G., Kontogiannis, L., Johnson, O., Powell, H. R. & Leslie, A. G. W. iMOSFLM: a new graphical interface for diffraction-image processing with MOSFLM. *Acta Crystallogr. D Biol. Crystallogr.* **67**, 271–281 (2011).

49. Leslie, A. G. W. & Powell, H. R. Processing diffraction data with mosflm. in *Evolving Methods for Macromolecular Crystallography* (eds. Read, R. J. & Sussman, J. L.) vol. 245 41–51 (Springer Netherlands, 2007).

50. Sawaya, M. R. *et al.* Ab initio structure determination from prion nanocrystals at atomic resolution by MicroED. *Proc. Natl. Acad. Sci. U. S. A.* **113**, 11232–11236 (2016).

51. Richards, L. S. *et al.* Fragment-based determination of a proteinase K structure from MicroED data using ARCIMBOLDO_SHREDDER. *Acta Crystallogr. Sect. Struct. Biol.* **76**, 703–712 (2020).

52. Kimura, Y. *et al.* Surface of bacteriorhodopsin revealed by high-resolution electron crystallography. *Nature* **389**, 206–211 (1997).

53. Mitsuoka, K. *et al.* The structure of bacteriorhodopsin at 3.0 A resolution based on electron crystallography: implication of the charge distribution. *J. Mol. Biol.* **286**, 861–882 (1999).

54. Marques, M. A., Purdy, M. D. & Yeager, M. CryoEM maps are full of potential. *Curr. Opin. Struct. Biol.* **58**, 214–223 (2019).

55. Yonekura, K. *et al.* Ionic scattering factors of atoms that compose biological molecules. *IUCrJ* **5**, 348–353 (2018).

56. Yonekura, K. & Maki-Yonekura, S. Refinement of cryo-EM structures using scattering factors of charged atoms. *J. Appl. Crystallogr.* **49**, 1517–1523 (2016).

57. Blum, T. B. *et al.* Statistically correcting dynamical electron scattering improves the refinement of protein nanocrystals, including charge refinement of coordinated metals. *Acta Crystallogr. Sect. Struct. Biol.* **77**, 75–85 (2021).

58. Wu, J. S. & Spence, J. C. H. Structure and bonding in α-copper phthalocyanine by electron diffraction. *Acta Crystallogr. A* **59**, 495–505 (2003).

59. Zuo, J. M., Kim, M., O'Keeffe, M. & Spence, J. C. H. Direct observation of d-orbital holes and Cu–Cu bonding in Cu2O. *Nature* **401**, 49–52 (1999).

60. Abrams, I. M. & McBain, J. W. A Closed Cell for Electron Microscopy. *Science* **100**, 273–274 (1944).

61. Turner, J. N., See, C. W., Ratkowski, A. J., Chang, B. B. & Parsons, D. F. Design and operation of a differentially pumped environmental chamber for the HVEM. *Ultramicroscopy* **6**, 267–279 (1981).

62. Ross, F. M. Opportunities and challenges in liquid cell electron microscopy. *Science* **350**, aaa9886 (2015).

63. Marton, L. Electron Microscopy of Biological Objects. *Nature* **133**, 911–911 (1934).

64. Marton, L. Electron Microscopy of Biological Objects. *Phys. Rev.* **46**, 527–528 (1934).

65. Marton, L. Early application of electron microscopy to biology. *Ultramicroscopy* **1**, 281–296 (1976).

66. Chiu, P.-L., Kelly, D. F. & Walz, T. The use of trehalose in the preparation of specimens for molecular electron microscopy. *Micron Oxf. Engl. 1993* **42**, 762–772 (2011).

67. Jap, B. K., Downing, K. H. & Walian, P. J. Structure of PhoE porin in projection at 3.5 A resolution. *J. Struct. Biol.* **103**, 57–63 (1990).

68. Hirai, T., Murata, K., Mitsuoka, K., Kimura, Y. & Fujiyoshi, Y. Trehalose embedding technique for high-resolution electron crystallography: application to structural study on bacteriorhoposin. *J. Electron Microsc. (Tokyo)* **48**, 653–658 (1999).

69. Hite, R. K., Schenk, A. D., Li, Z., Cheng, Y. & Walz, T. Collecting electron crystallographic data of two-dimensional protein crystals. *Methods Enzymol.* **481**, 251–282 (2010).

70. Tani, K. *et al.* Mechanism of Aquaporin-4's Fast and Highly Selective Water Conduction and Proton Exclusion. *J. Mol. Biol.* **389**, 694–706 (2009).

71. Walian, P. J. & Jap, B. K. Three-dimensional electron diffraction of PhoE porin to 2.8 A resolution. *J. Mol. Biol.* **215**, 429–438 (1990).

72. De Carlo S, null, Adrian, null, Kälin, null, Mayer, null & Dubochet, null. Unexpected property of trehalose as observed by cryo-electron microscopy. *J. Microsc.* **196**, 40–45 (1999).

73. Gyobu, N. *et al.* Improved specimen preparation for cryo-electron microscopy using a symmetric carbon sandwich technique. *J. Struct. Biol.* **146**, 325–333 (2004).

74. Taylor, K. A. & Glaeser, R. M. Retrospective on the early development of cryoelectron microscopy of macromolecules and a prospective on opportunities for the future. *J. Struct. Biol.* **163**, 214–223 (2008).

75. Glaeser, R. M. & Taylor, K. A. Radiation damage relative to transmission electron microscopy of biological specimens at low temperature: a review. *J. Microsc.* **112**, 127–138 (1978).

76. Taylor, K. & Glaeser, R. Electron microscopy of frozen hydrated biological specimens. **55**, 448–56 (1976).

77. Brüggeller, P. & Mayer, E. Complete vitrification in pure liquid water and dilute aqueous solutions. *Nature* **288**, 569–571 (1980).

78. Dubochet, J. & McDowall, A. W. Vitrification of pure water for electron microscopy. *J. Microsc.* **124**, 3–4 (1981).

79. Dubochet, J., Lepault, J., Freeman, R., Berriman, J. & Homo, J. -C. Electron microscopy of frozen water and aqueous solutions. *J. Microsc.* **128**, 219–237 (1982).

80. Adrian, M., Dubochet, J., Lepault, J. & W, M., Alasdair. Cryo-electron microscopy of viruses. *Nature* **308**, 32–36 (1984).

81. Tivol, W. F., Briegel, A. & Jensen, G. J. An improved cryogen for plunge freezing. *Microsc. Microanal. Off. J. Microsc. Soc. Am. Microbeam Anal. Soc. Microsc. Soc. Can.* **14**, 375–379 (2008).

82. Martynowycz, M. W. & Gonen, T. Protocol for the use of focused ion-beam milling to prepare crystalline lamellae for microcrystal electron diffraction (MicroED). *STAR Protoc.* **2**, 100686 (2021).

83. Danelius, E. & Gonen, T. Protein and Small Molecule Structure Determination by the Cryo-EM Method MicroED. *Methods Mol. Biol. Clifton NJ* **2305**, 323–342 (2021).

84. Bu, G. & Nannenga, B. L. MicroED and Data Collection For Protein. in *cryoEM* (eds. Gonen, T. & Nannenga, B. L.) vol. 2215 287–297 (Springer US, 2021).

85. Shi, D. *et al.* The collection of MicroED data for macromolecular crystallography. *Nat. Protoc.* **11**, 895–904 (2016).

86. Martynowycz, M. W. & Gonen, T. Studying Membrane Protein Structures by MicroED. *Methods Mol. Biol. Clifton NJ* **2302**, 137–151 (2021).

87. Martynowycz, M. W. & Gonen, T. Microcrystal Electron Diffraction of Small Molecules. *J. Vis. Exp. JoVE* (2021) doi:10.3791/62313.

88. Newman, J. A. *et al.* From Powders to Single Crystals: A Crystallographer's Toolbox for Small-Molecule Structure Determination. *Mol. Pharm.* acs.molpharmaceut.2c00020 (2022) doi:10.1021/acs.molpharmaceut.2c00020.

89. Clabbers, M. T. B. & Xu, H. Macromolecular crystallography using microcrystal electron diffraction. *Acta Crystallogr. Sect. Struct. Biol.* **77**, 313–324 (2021).

90. Cowley, J. M. & Moodie, A. F. The scattering of electrons by atoms and crystals. I. A new theoretical approach. *Acta Crystallogr.* **10**, 609–619 (1957).

91. Feja, B. & Aebi, U. Determination of the inelastic mean free path of electrons in vitrified ice layers for on-line thickness measurements by zero-loss imaging. *J. Microsc.* **193**, 15–19 (1999).

92. Egerton, R. F. & Cheng, S. C. Measurement of local thickness by electron energy-loss spectroscopy. *Ultramicroscopy* **21**, 231–244 (1987).

93. Grimm, R., Typke, D., Bärmann, M. & Baumeister, W. Determination of the inelastic mean free path in ice by examination of tilted vesicles and automated most probable loss imaging. *Ultramicroscopy* **63**, 169–179 (1996).

94. Malis, T., Cheng, S. C. & Egerton, R. F. EELS log-ratio technique for specimen-thickness measurement in the TEM. *J. Electron Microsc. Tech.* **8**, 193–200 (1988).

95. Egerton, R. F. A data base for energy-loss cross-section and mean free path. *Fiftieth Annu. Proc. Electron Microoscopy Sciety Am.* 1264–1265 (1992).

96. Martynowycz, M. W., Clabbers, M. T. B., Unge, J., Hattne, J. & Gonen, T. Benchmarking the ideal sample thickness in cryo-EM. *Proc. Natl. Acad. Sci. U. S. A.* **118**, e2108884118 (2021).

97. Desbois, S., Seabrook, S. A. & Newman, J. Some practical guidelines for UV imaging in the protein crystallization laboratory. *Acta Crystallograph. Sect. F Struct. Biol. Cryst. Commun.* **69**, 201–208 (2013).

98. Stevenson, H. P. *et al.* Use of transmission electron microscopy to identify nanocrystals of challenging protein targets. *Proc. Natl. Acad. Sci.* **111**, 8470–8475 (2014).

99. Stevenson, H. P. *et al.* Transmission electron microscopy for the evaluation and optimization of crystal growth. *Acta Crystallogr. Sect. Struct. Biol.* **72**, 603–615 (2016).

100. Barnes, C. O. *et al.* Assessment of microcrystal quality by transmission electron microscopy for efficient serial femtosecond crystallography. *Arch. Biochem. Biophys.* **602**, 61–68 (2016).

101. Eddleston, M. D., Hejczyk, K. E., Bithell, E. G., Day, G. M. & Jones, W. Polymorph Identification and Crystal Structure Determination by a Combined Crystal Structure Prediction and Transmission Electron Microscopy Approach. *Chem. - Eur. J.* **19**, 7874–7882 (2013).

102. Kissick, D. J., Wanapun, D. & Simpson, G. J. Second-Order Nonlinear Optical Imaging of Chiral Crystals. *Annu. Rev. Anal. Chem.* **4**, 419–437 (2011).

103. Weiss, S., Vergara, S., Lin, G. & Calero, G. Detection of Microcrystals for CryoEM. in *cryoEM* (eds. Gonen, T. & Nannenga, B. L.) vol. 2215 299–307 (Springer US, 2021).

104. Go, E. B., Kim, L. J., Nelson, H. M., Ohashi, M. & Tang, Y. Biosynthesis of the Fusarium Mycotoxin (-)-Sambutoxin. *Org. Lett.* (2021) doi:10.1021/acs.orglett.1c02836.

105. Palatinus, L. *et al.* Hydrogen positions in single nanocrystals revealed by electron diffraction. *Science* **355**, 166–169 (2017).

106. Kim, L. J. *et al.* Structure Revision of the Lomaiviticins. *J. Am. Chem. Soc.* **143**, 6578–6585 (2021).

107. Samkian, A. E. *et al.* Elucidation of Diverse Solid-State Packing in a Family of Electron-Deficient Expanded Helicenes via Microcrystal Electron Diffraction (MicroED)*. *Angew. Chem. Int. Ed Engl.* **60**, 2493–2499 (2021).

108. Dick, M., Sarai, N. S., Martynowycz, M. W., Gonen, T. & Arnold, F. H. Tailoring Tryptophan Synthase TrpB for Selective Quaternary Carbon Bond Formation. *J. Am. Chem. Soc.* **141**, 19817–19822 (2019).

109. Russo, C. J. & Passmore, L. A. Progress towards an optimal specimen support for electron cryomicroscopy. *Curr. Opin. Struct. Biol.* **37**, 81–89 (2016).

110. Karuppasamy, M., Nejadasl, K. F., Vulovic, M., Koster, A. J. & Ravelli, R. B. G. Radiation damage in single-particle cryo-electron microscopy: effects of dose and dose rate. **18**, 398–412 (2011).

111. Weissenberger, G., Henderikx, R. J. M. & Peters, P. J. Understanding the invisible hands of sample preparation for cryo-EM. *Nat. Methods* **18**, 463–471 (2021).

112. Bradley, D. E. Evaporated carbon films for use in electron microscopy. *Br. J. Appl. Phys.* **5**, 65–66 (1954).

113. Fukami, A. & Adachi, K. A new method of preparation of a self-perforated micro plastic grid and its application. *J. Electron Microsc. (Tokyo)* **14**, 112–118 (1965).

114. Fukami, A., Adachi, K. & Katoh, M. Micro Grid Techniques (continued) and Their Contribution to Specimen Preparation Techniques for High Resolution Work. *J. Electron Microsc. (Tokyo)* **21**, 99–108 (1972).

115. Baumeister, W. & Seredynski, J. Preparation of performed films with predeterminable hole size distributions. *Micron 1969* **7**, 49–54 (1976).

116. Ermantraut, E., Wohlfart, K. & Tichelaar, W. Perforated support foils with pre-defined hole size, shape and arrangement. *Ultramicroscopy* **74**, 75–81 (1998).

117. Chester, D. W., Klemic, J. F., Stern, E., Sigworth, F. J. & Klemic, K. G. Holey carbon micro-arrays for transmission electron microscopy: A microcontact printing approach. *Ultramicroscopy* **107**, 685–691 (2007).

118. Quispe, J. *et al.* An Improved Holey Carbon Film for Cryo-Electron Microscopy. *Microsc. Microanal.* **13**, 365–371 (2007).

119. Naydenova, K., Jia, P. & Russo, C. J. Cryo-EM with sub–1 Å specimen movement. *Science* **370**, 223–226 (2020).

120. Passmore, L. A. & Russo, C. J. Methods in Enzymology. *Methods Enzymol.* **579**, 51–86 (2016).

121. Cheung, M. *et al.* A method to achieve homogeneous dispersion of large transmembrane complexes within the holes of carbon films for electron cryomicroscopy. *J. Struct. Biol.* **182**, 51–56 (2013).

122. Bellare, J. R., Davis, H. T., Scriven, L. E. & Talmon, Y. Controlled environment vitrification system: an improved sample preparation technique. *J. Electron Microsc. Tech.* **10**, 87–111 (1988).

123. Frederik, P. M. & Hubert, D. H. W. Cryoelectron Microscopy of Liposomes. in *Methods in Enzymology* vol. 391 431–448 (Elsevier, 2005).

124. Comolli, L. R. *et al.* A portable cryo-plunger for on-site intact cryogenic microscopy sample preparation in natural environments. *Microsc. Res. Tech.* **75**, 829–836 (2012).

125. Cyrklaff, M., Adrian, M. & Dubochet, J. Evaporation during preparation of unsupported thin vitrified aqueous layers for cryo-electron microscopy. *J. Electron Microsc. Tech.* **16**, 351–355 (1990).

126. Zhao, J. *et al.* A simple pressure-assisted method for MicroED specimen preparation. *Nat. Commun.* **12**, 5036 (2021).

127. Grassucci, R. A., Taylor, D. J. & Frank, J. Preparation of macromolecular complexes for cryo-electron microscopy. *Nat. Protoc.* **2**, 3239–3246 (2007).

128. *Single-particle Cryo-EM of Biological Macromolecules*. (IOP Publishing, 2021). doi:10.1088/978-0-7503-3039-8.

129. Darwin, C. G. XCII. The reflexion of X-rays from imperfect crystals. *Lond. Edinb. Dublin Philos. Mag. J. Sci.* **43**, 800–829 (1922).

130. Nave, C. A description of imperfections in protein crystals. *Acta Crystallogr. D Biol. Crystallogr.* **54**, 848–853 (1998).

131. Cusack, S. *et al.* Small is beautiful: protein micro-crystallography. *Nat. Struct. Biol.* **5**, 634–637 (1998).

132. Landau, E. M. & Rosenbusch, J. P. Lipidic cubic phases: a novel concept for the crystallization of membrane proteins. *Proc. Natl. Acad. Sci. U. S. A.* **93**, 14532–14535 (1996).

133. Perry, S. L., Roberts, G. W., Tice, J. D., Gennis, R. B. & Kenis, P. J. A. Microfluidic Generation of Lipidic Mesophases for Membrane Protein Crystallization. *Cryst. Growth Des.* **9**, 2566–2569 (2009).

134. Zhu, L. *et al.* Structure Determination from Lipidic Cubic Phase Embedded Microcrystals by MicroED. *Struct. Lond. Engl. 1993* **28**, 1149-1159.e4 (2020).

135. Polovinkin, V. *et al.* Demonstration of electron diffraction from membrane protein crystals grown in a lipidic mesophase after lamella preparation by focused ion beam milling at cryogenic temperatures. *J. Appl. Crystallogr.* **53**, 1416–1424 (2020).

136. Martynowycz, M. W. *et al.* MicroED structure of the human adenosine receptor determined from a single nanocrystal in LCP. *Proc. Natl. Acad. Sci. U. S. A.* **118**, e2106041118 (2021).

137. Martynowycz, M. W., Khan, F., Hattne, J., Abramson, J. & Gonen, T. MicroED Structure of Lipid-Embedded Mammalian Mitochondrial Voltage-Dependent Anion Channel. *Proc. Natl. Acad. Sci. U. S. A.* **117**, 32380–85 (2020).

138. Martynowycz, M. W. *et al.* A robust approach for MicroED sample preparation of lipidic cubic phase embedded membrane protein crystals. *Nat. Commun.* **14**, 1086 (2023).

139. Shiriaeva, A., Martynowycz, M. W., Nicolas, W. J., Cherezov, V. & Gonen, T. MicroED structure of the human vasopressin 1B receptor. *bioRxiv* 2023.07.05.547888 (2023) doi:10.1101/2023.07.05.547888.

140. Gillman, C., Nicolas, W. J., Martynowycz, M. W. & Gonen, T. Design and implementation of suspended drop crystallization. *Iucrj* **10**, (2023).

141. Christensen, J. *et al.* Radiation damage in Helena small-molecule crystallography: fact not fiction. *IUCrJ* **6**, 703–713 (2019).

142. Engstrom, T. *et al.* High-resolution single-particle cryo-EM of samples vitrified in boiling nitrogen. *IUCrJ* **8**, (2021).

143. Dobro, M. J., Melanson, L. A., Jensen, G. J. & McDowall, A. W. Plunge freezing for electron cryomicroscopy. *Methods Enzymol.* **481**, 63–82 (2010).

144. Dubochet, J. *et al.* Cryo-electron microscopy of vitrified specimens. *Q. Rev. Biophys.* **21**, 129–228 (1988).

145. Rodgers, D. W. [13] Practical cryocrystallography. in *Methods in Enzymology* vol. 276 183–203 (Elsevier, 1997).

146. Teng, T.-Y. Mounting of crystals for macromolecular crystallography in a free-standing thin film. *J. Appl. Crystallogr.* **23**, 387–391 (1990).

147. Masuda, T. *et al.* Atomic resolution structure of serine protease proteinase K at ambient temperature. *Sci. Rep.* **7**, 45604 (2017).

148. Caffrey, M. & Cherezov, V. Crystallizing membrane proteins using lipidic mesophases. *Nat. Protoc.* **4**, 706–731 (2009).

149. Liu, W., Ishchenko, A. & Cherezov, V. Preparation of microcrystals in lipidic cubic phase for serial femtosecond crystallography. *Nat. Protoc.* **9**, 2123–2134 (2014).

150. Jones, C. G. *et al.* The CryoEM Method MicroED as a Powerful Tool for Small Molecule Structure Determination. *ACS Cent. Sci.* **4**, 1587–1592 (2018).

151. Gruene, T. *et al.* Rapid Structure Determination of Microcrystalline Molecular Compounds Using Electron Diffraction. *Angew. Chem. Int. Ed Engl.* **57**, 16313–16317 (2018).

152. Gleason, P. R., Nannenga, B. L. & Mills, J. H. Rapid Structural Analysis of a Synthetic Non-canonical Amino Acid by Microcrystal Electron Diffraction. *Front. Mol. Biosci.* **7**, 609999 (2020).

153. Curtis, B. J. *et al.* Identification of Uric Acid Gluconucleoside-Ascaroside Conjugates in Caenorhabditis elegans by Combining Synthesis and MicroED. *Org. Lett.* **22**, 6724–6728 (2020).

154. Bruhn, J. F. *et al.* Small Molecule Microcrystal Electron Diffraction for the Pharmaceutical Industry–Lessons Learned From Examining Over Fifty Samples. *Front. Mol. Biosci.* **8**, 648603 (2021).

155. Martynowycz, M. W., Zhao, W., Hattne, J., Jensen, G. J. & Gonen, T. Collection of Continuous Rotation MicroED Data from Ion Beam-Milled Crystals of Any Size. *Struct. Lond. Engl. 1993* **27**, 545-548.e2 (2019).

156. Martynowycz, M. W., Clabbers, M. T. B., Hattne, J. & Gonen, T. Ab initio phasing macromolecular structures using electron-counted MicroED data. *Nat. Methods* **19**, 724–729 (2022).

157. Duyvesteyn, H. M. E. *et al.* Machining protein microcrystals for structure determination by electron diffraction. *Proc. Natl. Acad. Sci.* **115**, 9569–9573 (2018).

158. Li, X., Zhang, S., Zhang, J. & Sun, F. In situ protein micro-crystal fabrication by cryo-FIB for electron diffraction. *Biophys. Rep.* **4**, 339–347 (2018).

159. Martynowycz, M. W., Zhao, W., Hattne, J., Jensen, G. J. & Gonen, T. Qualitative Analyses of Polishing and Precoating FIB Milled Crystals for MicroED. *Struct. Lond. Engl. 1993* **27**, 1594-1600.e2 (2019).

160. Zhou, J. *et al.* Cryogenic Focused Ion Beam Enables Atomic-Resolution Imaging of Local Structures in Highly Sensitive Bulk Crystals and Devices. *J. Am. Chem. Soc.* **144**, 3182–3191 (2022).

161. Martynowycz, M. W. *et al.* MicroED Structure of the Human Adenosine Receptor Determined from a Single Nanocrystal in LCP. *Proc. Natl. Acad. Sci. U. S. A.* **118**, 2106041118 (2021).

162. Smith, N. S. *et al.* High brightness inductively coupled plasma source for high current focused ion beam applications. *J. Vac. Sci. Technol. B Microelectron. Nanometer Struct. Process. Meas. Phenom.* **24**, 2902–2906 (2006).

163. Sergey, G. *et al.* Oxygen plasma focused ion beam scanning electron microscopy for biological samples. *bioRxiv* 457820 (2018) doi:10.1101/457820.

164. Fenalti, G., Abola, E. E., Wang, C., Wu, B. & Cherezov, V. *Fluorescence Recovery After Photobleaching in Lipidic Cubic Phase (LCP-FRAP)*. *Membrane proteins.* vol. 557 (Elsevier/Academic Press, 2015).

165. Caffrey, M. & Cherezov, V. Crystallizing Membrane Proteins Using Lipidic Mesophases. *Nat. Protoc.* **4**, 706–31 (2009).

166. Schaffer, M. *et al.* Optimized cryo-focused ion beam sample preparation aimed at in situ structural studies of membrane proteins. *J. Struct. Biol.* **197**, 73–82 (2017).

167. Marko, M., Hsieh, C., Schalek, R., Frank, J. & Mannella, C. Focused-ion-beam thinning of frozen-hydrated biological specimens for cryo-electron microscopy. *Nat. Methods* **4**, 215–217 (2007).

168. Wagner, F. R. *et al.* Preparing samples from whole cells using focused-ion-beam milling for cryo-electron tomography. *Nat. Protoc.* **15**, 2041–2070 (2020).

169. Wnuk, J. D. *et al.* Electron Induced Surface Reactions of the Organometallic Precursor Trimethyl(methylcyclopentadienyl)platinum(IV). *J. Phys. Chem. C* **113**, 2487–2496 (2009).

170. de la Cruz, M. J., Martynowycz, M. W., Hattne, J. & Gonen, T. MicroED data collection with SerialEM. *Ultramicroscopy* **201**, 77–80 (2019).

171. Hattne, J. Low-Dose Data Collection and Radiation Damage in MicroED. *Methods Mol. Biol. Clifton NJ* **2215**, 309–319 (2021).

172. Nannenga, B. L. MicroED methodology and development. *Struct. Dyn.* **7**, 014304 (2020).

173. Bücker, R. *et al.* Serial protein crystallography in an electron microscope. *Nat. Commun.* **11**, 996 (2020).

174. Wang, B., Zou, X. & Smeets, S. Automated serial rotation electron diffraction combined with cluster analysis: an efficient multi-crystal workflow for structure determination. *IUCrJ* **6**, 854–867 (2019).

175. Gruene, T. & Mugnaioli, E. 3D Electron Diffraction for Chemical Analysis: Instrumentation Developments and Innovative Applications. *Chem. Rev.* **121**, 11823–11834 (2021).

176. Lovelace, J. J. & Borgstahl, G. E. O. Characterizing pathological imperfections in macromolecular crystals: lattice disorders and modulations. *Crystallogr. Rev.* **26**, 3–50 (2020).

Chapter 4: Design and implementation of suspended drop crystallization

Authors

Cody Gillman[1,2], William J. Nicolas[1,3], Michael W. Martynowycz[1], Tamir Gonen[1,2,3*]

Affiliations

[1] Departments of Biological Chemistry and Physiology, University of California, Los Angeles CA, USA

[2] Molecular Biology Institute, University of California, Los Angeles, Los Angeles, CA 90095, USA

[3] Howard Hughes Medical Institute, University of California, Los Angeles CA, USA

* To whom correspondence should be sent T.G. tgonen@g.ucla.edu

Abstract

We have developed a novel crystal growth method known as suspended drop crystallization. Unlike traditional methods, this technique involves mixing protein and precipitant directly on an electron microscopy grid without any additional support layers. The grid is then suspended within a crystallization chamber which we designedthis , allowing for vapor diffusion to occur from both sides of the drop. A UV transparent window above and below the grid enables the monitoring of crystal growth via light, UV, or fluorescence microscopy. Once crystals have formed, the grid can be removed and utilized for x-ray crystallography or microcrystal electron diffraction (MicroED) directly without having to manipulate the crystals. To demonstrate the efficacy of this method, we

grew crystals of the enzyme proteinase K and determined its structure by MicroED following FIB/SEM milling to render the sample thin enough for cryoEM. Suspended drop crystallization overcomes many of the challenges associated with sample preparation, providing an alternative workflow for crystals embedded in viscous media, sensitive to mechanical stress, and/or suffering from preferred orientation on EM grids.

Introduction

Crystallography is a widely used technique for determining the structures of both small and large molecules such as proteins[1]. Crystals, which possess repetitive structural patterns, are utilized in this approach[2]. When a coherent beam of x-rays or electrons is directed at a crystal, it is scattered in predictable ways that provide information about the underlying structure of the molecule in the crystal[3]. Over the past century, a number of crystal growth methods have been developed and refined, including liquid-liquid diffusion[4], vapor diffusion using hanging or sitting drops[5], and lipidic cubic phase (LCP)[6]. Additionally, two-dimensional crystallization utilizing dialysis and growth through evaporation and concentration has also been explored and documented[7–9].

Vapor diffusion is the most commonly employed method for protein crystallization[10]. In this method, the protein of interest is mixed with a mother liquor and placed either in a small well or on a glass support that hangs above the solution. The mixture is then sealed in a chamber with additional crystallization solution to allow for vapor diffusion. As the vapors form, the effective concentration of the protein increases, causing the drop to shrink. Under certain conditions, crystals may form, which are then

detected using light, UV, or fluorescence. Several automated instruments have been developed for crystal detection. Hanging drops are typically used for soluble proteins in aqueous solution, while sitting drops are preferred for membrane proteins that may be in a solution with detergent and lipids [11]. Various conditions are tested to optimize crystal growth, including pH, temperature, precipitants, and additives.

MicroED is a cryogenic electron microscopy (CryoEM) technique that utilizes electron diffraction to determine the three-dimensional structure of proteins, peptides, and small molecules in cryogenic conditions[12–16]. This method is suitable for crystals that are extremely small and typically invisible to the naked eye, with a size a billionth that required for x-ray crystallography [17,18]. Once a crystal is obtained, it is transferred onto an electron microscopy grid using a pipette and rapidly frozen in liquid ethane. The sample is then placed in an electron microscope operating at liquid nitrogen temperatures to minimize radiation damage. The electron beam is focused in diffraction mode onto the crystal when it is identified, and MicroED data is collected on a fast camera while the stage is continuously rotating. X-ray data reduction software is utilized to process the MicroED data, and established procedures are employed to determine the structures[19].

Recent studies have demonstrated successful determination of structures for membrane proteins embedded in lipids using a novel approach for sample preparation[20–22]. The method utilizes a scanning electron microscope coupled with a focused ion beam (FIB/SEM) for sample preparation. In one example, the human adenosine receptor ($A2_AAR$) was crystallized in LCP, and the crystal drop was transferred to an electron microscopy grid by blotting and rapid freezing in liquid ethane. The sample was too thick

for visualization by a transmission electron microscope, so fluorescence was used to locate the nanocrystals within the lipid matrix. Correlative light-EM was then utilized to expose the crystals with the FIB for MicroED analyses, resulting in a high-resolution (2.0 Å) structure of the human receptor[22]. A similar approach was also used to determine the structure of a functional mutant of the mammalian voltage-dependent anion channel VDAC[21].

In certain cases, it is advisable to avoid transferring crystals onto an electron microscopy grid. Some protein crystals may be too delicate and have a large solvent fraction, which can result in damage during the transfer process and render them unsuitable for MicroED. Additionally, membrane protein crystals embedded in lipids, such as those formed through lipidic cubic phase crystallization, are highly susceptible to damage from physical manipulation. For these sensitive samples, new sample preparation techniques must be developed and optimized to ensure their suitability for MicroED.

Although the aforementioned sample preparation methods have been successful, they rely on the assumption that crystals are not damaged during the physical manipulation and transfer onto an electron microscopy grid. Additionally, certain crystals, especially those that resemble sheets, may exhibit a preferred orientation on the grid carbon support, which can limit the reciprocal space available for sampling. Given these challenges, there is a need to develop alternative approaches for sample preparation for MicroED, as well as for other imaging applications such as x-ray crystallography.

Here we used conceptual design and 3D printing to create a suspended drop crystallization setup. This is a novel approach for sample preparation for MicroED that eliminates the need for crystal transfer and physical manipulation, offering an alternative to traditional crystallization methods. The method involves allowing crystallization to occur directly on an EM grid without support, enabling both sides of the drop to be exposed for uniform vapor diffusion. The absence of support film on the grid eliminates preferred crystal orientations and enables complete reciprocal lattice sampling. Crystal growth can be monitored visually, and the entire crystallization drop can be plunge-frozen directly on the EM grid. The method was successfully demonstrated on proteinase K crystals, resulting in a 2.1 Å resolution structure. This approach may have potential for other imaging applications beyond MicroED.

Results

The 3D printed suspended drop screening tool.

The suspended drop crystallization screening tool is a screw cap that can mount pre-clipped EM grids and suspend them over a well reservoir. The screw and mounting arms are made of a flexible rubber material made of thermoplastic polyurethane (TPU) that applies gentle pressure on the clipped EM grid without the risk of bending (Figure 4.1a). The screw also incorporates a clear glass coverslip that is securely tightened by a 3D printed plastic screw to create a viewing window. After dispensing sample onto a support-free EM grid, the suspended drop is sealed into an incubation chamber containing mother liquor (Figure 4.1b). Suspended crystallization drops can be monitored through the viewing window using light and fluorescent microscopy.

A screening tray was also been designed and 3D printed, which can accommodate multiple incubation chambers for larger screening experiments (Figure 1C). When suspended drop crystals are identified, the screening tool is unscrewed from the well, tweezers are used to retrieve the grid, and the grid is rapidly plunged into liquid nitrogen or ethane without blotting (Figure 4.1d). We do not blot the support-free grids prior to vitrification because the crystals would likely be lost to the filter paper as there is no holey carbon support film to capture the crystals. Furthermore, blotting on grids with a support film would allow crystals prone to preferred orientation to become oriented on the film, which we want to avoid. The suspended crystallization drops we froze were on average 100 μm thick, while vitrification at atmospheric pressure is effective for samples 10 – 20 μm thick[23].

Although we plunged our suspended drops in liquid ethane, it is likely that the crystals were surrounded by some crystalline ice. Importantly, we observed no crystalline ice diffraction when the beam was focused on the lamella crystal site. For MicroED, FIB/SEM milling is performed prior to TEM imaging (Figure 4.1e). The suspended drop crystallization method can also be used directly for x-ray analysis by mounting the grid directly onto the goniometer.

Protein crystals grown by suspended drop crystallization.

We hypothesized that support-free gold gilder grids with a low mesh count (50-200 mesh) could be used to suspend crystallization drops during long incubation periods. Experimental results confirmed that suspended crystallization drops could be stably

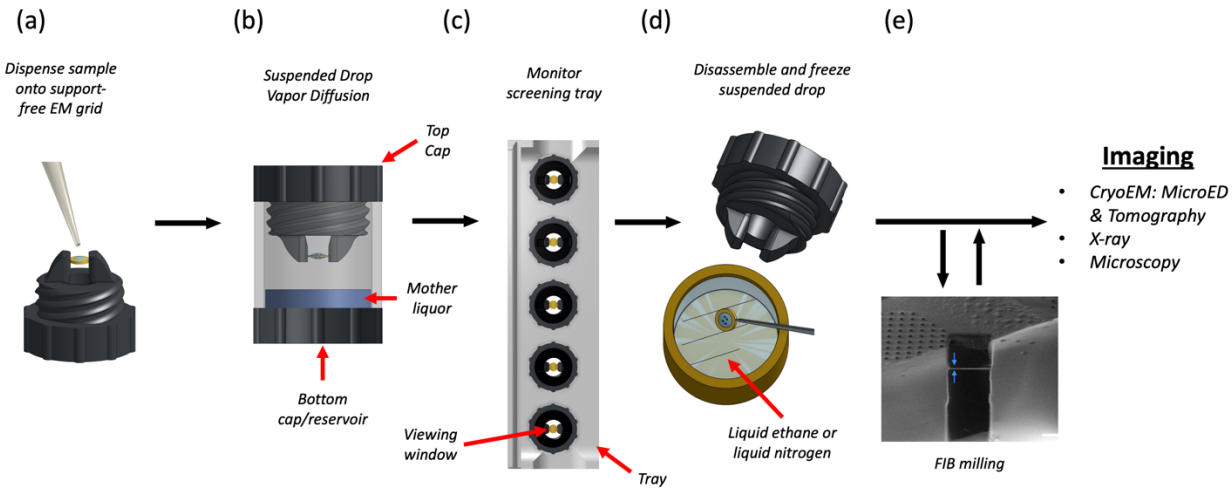

Figure 4.1. Suspended drop crystallization. (a) A support-free EM grid is clipped into an autogrid cartridge and mounted between the arms of the suspended drop screening tool. The sample and crystallization solution are dispensed onto the grid. (b) The chamber is immediately sealed to allow vapor diffusion. (b) The incubation chambers are inserted into a screening tray for efficient storing and monitoring of crystallization progress by light, fluorescence and UV microscopy. (d) EM grids containing crystals are retrieved from the screening tool and frozen. (e) The specimen is then interrogated by MicroED or other methods such as tomography, x-ray crystallography, or general microscopy. FIB milling is optional depending on the application.

retained by such grids. Gold grids were chosen because gold is chemically inert as opposed to common copper grids. However, since the Thermo-Fisher autogrid cartrides we used do contain copper, the suspended drops we prepared were intentionally made small enough so that they would not touch the inner wall of the autogrid cartridge.

To prepare the grids, 3 mm diameter gold gilder grids were clipped into autogrid cartridges for stability and rigidity, and glow-discharged before being mounted horizontally between the mounting arms of the screw cap. Proteinase K sample was mixed with

mother liquor directly on the EM grid and the screening tool was tightened into the well of a crystallization tray for incubation (Figure 4.2a). Light microscopy and UV fluorescence was used to monitor the crystal growth through the coverslip at the top of the screening tool (Figure 4.2b, c).

Machining crystal lamella.

Grids containing suspended proteinase K crystallization drops were retrieved from the screening apparatus and immediately plunged into liquid ethane. The grids were loaded into a plasma beam FIB/SEM equipped with an integrated fluorescence microscope (iFLM) at cryogenic conditions. The surface of the crystallization drop appeared smooth in the SEM and crystal features could not be observed (Figure 4.2d). To visualize crystals below the surface of the drop, the iFLM was used to detect crystal fluorescence (Figure 4.2e). A series of images was acquired at different focal points between the grid bars and the surface of the drop, and the depth at which the crystal appeared most in focus was taken to be the true depth of the crystal. The stack of reflective images was correlated to the X-Y plane of the SEM images and a three-dimensional representation of crystal locations inside the drop was generated.

The targeted crystal and surrounding media were milled into a thin lamella using a xenon plasma beam (Figure 4.2f). We used the xenon plasma beam because it is the fastest and most gentle option for milling crystals that are deeply embedded in solvent [22]. The final lamella was ~7 µm wide and 300 nm thick.

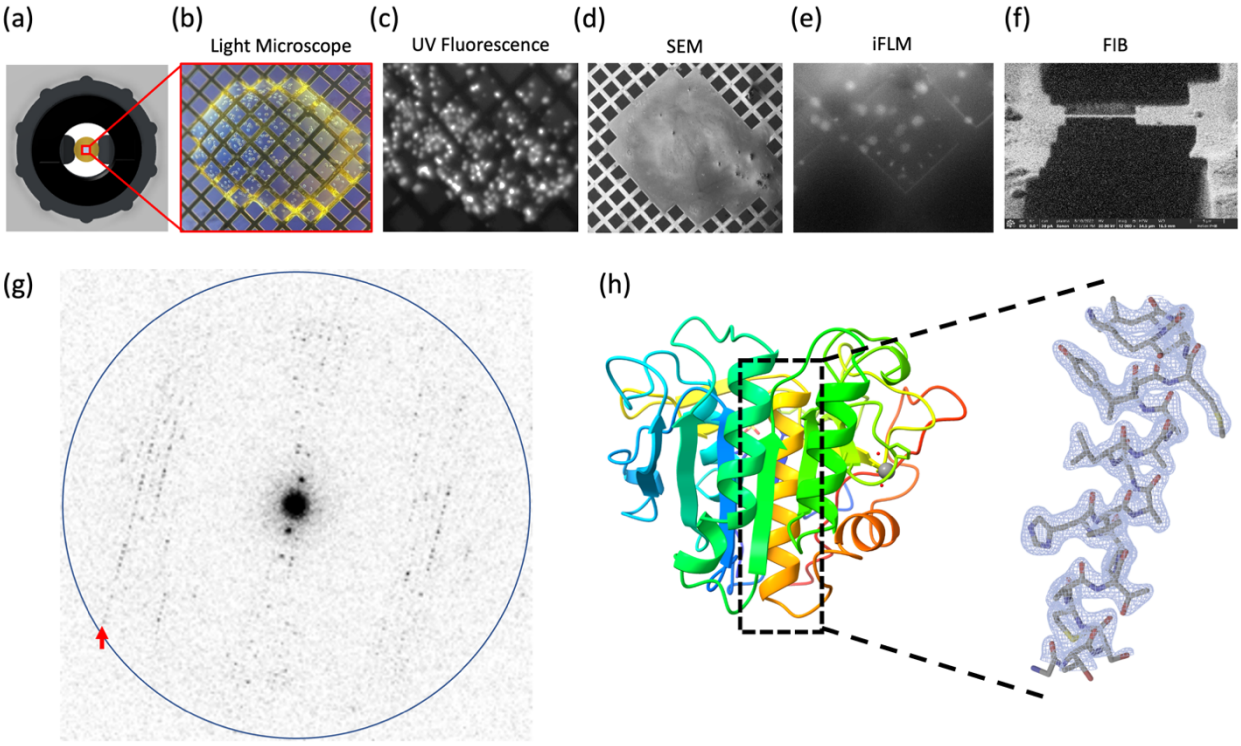

Figure 4.2. MicroED structure of suspended drop Proteinase K. (a) The suspended drop viewed from the top and imaged by (b) Light microscopy or (c) UV. A frozen suspended drop specimen was loaded into the FIB/SEM and imaged normal to the grid surface by (d) SEM and (e) iFLM with the 385 nm LED to locate submerged crystals. (f) The targeted crystal site was milled into a 300 nm thick lamella. (g) Example of MicroED data acquired from the crystal lamella. The highest resolution reflections visible to 2.1 Å (red arrow). Resolution ring is shown at 2.0 Å (blue). (H) Cartoon representation of the Proteinase K colored by rainbow with blue N terminus and red C terminus. The 2mFo–DFc map of a selected alpha-helix is highlighted, which was contoured at 1.5 σ with a 2-Å carve.

MicroED analyses of suspended drop crystals.

The grid containing the crystal lamella was transferred to a cryogenically cooled Titan Krios electron microscope operating at 300 kV. The lamella site was identified with low magnification imaging and brought to eucentric height. A diffraction preview of the lamella was acquired to confirm that it would diffract to high-resolution (Figure 4.2g). Continuous rotation MicroED data was collected on a real space wedge from -40° to +40° tilt using a Falcon4 direct electron detector set to counting mode. Data was collected with a selected area aperture to reduce background dose. Strong and sharp reflections were visible to 2.1 Å resolution and a clear lattice was visible.

MicroED data were converted to standard crystallographic formats using our online tools which are freely available (https://cryoem.ucla.edu/microed). The data were indexed and integrated in XDS to 2.1 Å resolution. Phases for the MicroED reflections were determined by molecular replacement. The space group was determined to be P $4_3 2_1 2$ with a unit cell of (a, b, c) (Å) = (68.26, 68.26, 101.95) and (α, β, γ) (°) = (90, 90, 90). The structure was refined using electron scattering factors (Table 1). The structure of proteinase K that was determined matches other MicroED structures of this protein that determined from crystals that were handled using traditional MicroED sample preparation protocols (Figure 4.2h).

Table 4.1. MicroED structure statistics of proteinase K crystallized by suspended drop.

Data	Parameter	Measure
Data Collection	accelerating voltage (kV)	300
	wavelength (Å)	0.019687
	electron source	field emission gun
	total accumulated exposure ($e^-/Å^2$)	0.64
	no. of crystals	1
	microscope	Thermo Fisher Titan Krios
	camera	Falcon 4 electron counting
	rotation rate (deg/sec)	0.2
Data analysis	resolution range (A)	30.42-2.10
	space group	$P4_32_12$
	a, c, c (Å)	68.26, 68.26, 101.95
	α, β, Y (°)	90, 90, 90
	reflections, total/unique	56301/12774
	multiplicity	4.41
	completeness (%)	87.0
	mean I/Iσ(I)	2.82
	CC1/2	92.5
	Rwork	0.2442
	Rfree	0.2917

Discussion

In this study, we utilized suspended drop crystallization to grow crystals of a protein, and subsequently determined its structure by MicroED. To optimize the conditions for suspended drop crystallization, we developed a screening tool that features a screw cap with two extended arms for clamping an EM grid and a clear glass coverslip that creates a viewing window (see Figure 4.2a). Once the sample was dispensed onto a support-free EM grid, the suspended drop was sealed into an incubation chamber with mother liquor (see Figure 4.2b), and its growth could be monitored using light and fluorescent microscopy. To harvest the crystals, the screening tool was unscrewed from the

incubation well, and the grid was retrieved with tweezers and rapidly frozen in liquid nitrogen or ethane for cryo-preservation.

The process for preparing MicroED samples is akin to the standard procedure followed in other cryoEM techniques like single particle analysis (SPA) and tomography. The sample is usually dispensed onto an EM grid, excess solvent is blotted, and the grid is vitrified by immersing it in liquid ethane[24]. However, enhancing the preparation of samples for MicroED experiments using this method can be challenging because of limited options for improving crystal transfer and blotting conditions, which could cause damage to fragile crystals. Nevertheless, suspended drop crystallization offers an alternative specimen preparation method that eliminates the need for crystal transfer and blotting. This technique presents a promising solution for crystallographers dealing with challenging crystals that are embedded in viscous buffer (e.g., membrane proteins or crystals in high precipitant conditions), prone to mechanical stress, toxic, volatile, or limited in number in the drop. We envisage that suspended drop crystallization will be valuable in the preparation of recalcitrant crystals for MicroED experiments.

Crystals that adopt a preferred orientation on EM grids with carbon support can lead to incomplete sampling of the reciprocal space, limiting the accuracy of structural determination. This is especially common in plate-like sheet crystals, such as those of Catalase and Calcium-ATPase[25,26]. However, growing crystals using the support-free suspended grid method can avoid preferred orientation. As there is no support film, crystals cannot align themselves in a specific orientation, allowing for 100% sampling of the reciprocal space for any crystal morphology and symmetry by merging data from several crystals. It is possible that grids containing a higher number of grid bars could

allow crystals to adopt preferred orientation. It is important to use grids with a low mesh count to grow crystals that nucleate within a window of the grid and away from grid bars. Using a 100 mesh count gilder grid, we were able to obtain many crystals that nucleated near the center of the windows (see Figure 4.2c, e). This approach is particularly useful for crystallographers working with challenging samples, enabling high-quality data collection and accurate structural determination.

The modular design of the suspended drop crystallization tools described in this study enable crystal growth to be efficiently assayed in a sparse matrix screen directly on grids without support. While others have demonstrated crystal growth directly on grids, they used grids with carbon support and did not demonstrate sparse matrix screening[27]. We found that gold grids were the most inert and produced the most consistent results, as copper grids tend to oxidize and prevent crystal growth, and holey carbon grids can make it difficult to monitor crystal growth. Using support-free gold grids with a lower mesh count allows for easier monitoring of crystal growth, reduces the amount of material in contact with the sample, and decreases the likelihood of obstruction by grid bars, which is important for subsequent FIB milling. Additionally, because no blotting is required with this setup, the initial position of the crystals remains unchanged after freezing, which facilitates targeting and FIB milling.

Using a support-free grid and a sparse matrix approach, the suspended drop method allows for easier monitoring of crystal growth and eliminates physical contact with the sample. Additionally, the use of a cryogenic plasma beam FIB/SEM enables efficient generation of sample lamellae, while cryogenic TEM allows for high-quality MicroED data collection. One major advantage of this approach is its potential applicability to membrane

proteins, which are notoriously difficult to crystallize due to their softness and fragility. Furthermore, the use of automation and robotics could further streamline the process and make it more accessible to structural biologists. Overall, the suspended drop crystallization method has the potential to become a routine approach in structural biology and although not demonstrated in this study, suspended drop crystallization could be employed in x-ray crystallography, as well as other microscopy and cryoEM applications.

Methods and Materials

Materials

Proteinase K from *Tritirachium album* was purchased from Fisher BioReagents (Hillsborough, OR) and used without further purification. Ammonium sulfate and Tris buffer were purchased from Sigma-Aldrich (St. Louis, MO). All reagents were made with MilliQ water. The Ultimaker S5 3D printer and all filaments were purchased from MatterHackers (Lake Forest, CA). Glass coverslips were purchased from Ted Pella (Redding, CA). The gold gilder grids were purchased from Electron Microscopy Sciences (Hatfield, PA). The 100 nm fluorescent TetraSpeck Microspheres were purchased from Thermo-Fisher.

Object design and 3D printing

All components of the screening tool were designed in the cloud-based CAD program Onshape.com and exported in STL file format. To generate GCODE files for 3D printing, the STL files were imported into the slicer program Ultimaker Cura 5.0 and default Ultimaker material profiles were used. All objects were printed at 0.1 mm layer height and 40 mm/sec print speed. All 3D printing was performed on an Ultimaker S5 3D printer equipped with a 0.4 mm diameter nozzle and a glass build surface with a layer of glue

applied. The main body of the screening tool and the cover slip gasket were printed in thermoplastic polyurethane (TPU). The cover slip retaining screw was printed in co-polyester (CPE). A single on-grid screening tool takes approximately 1.5 hrs to print.

Suspended drop crystallization

Proteinase K was dissolved in 0.1 M Tris-HCl pH 8.0 at 25 mg/ml. A support-free gold gilder grid was clipped into an autogrid cartridge, negatively glow-discharged for 1 min at 15 mA, and mounted in the screening tool. Equal volumes of proteinase K and 1.5 M ammonium sulfate were mixed dispensed on the mounted grid (~0.3 μL final drop volume). The screening tool (with mounted grid and crystallization drop) was immediately screwed into a well of the crystallization tray containing 300 μL of 1.5 M ammonium sulfate in the reservoir. Within 48 hrs, crystals of Proteinase K were observed in the hanging crystal drops.

Sample preparation and cryo-preservation

The EM grids supporting crystal drops were carefully removed from the screening tool with tweezers and rapidly plunged into liquid ethane. The grids were stored in liquid nitrogen until use.

Machining proteinase K crystal lamellae using the plasma beam FIB/SEM.

The vitrified EM grid was loaded into a Thermo-Fisher Helios Hydra dual-beam plasma beam FIB/SEM operating at cryogenic temperature. A whole-grid atlas of the drop was acquired by the SEM operating at an accelerating voltage of 0.5 kV and beam current of 13 pA using the MAPS v3.19 software (Thermo-Fisher). The crystal drop was coated with platinum by beam-assisted (argon beam at 4 nA, 5 kV) GIS coating for 1 min to protect

the sample from ion and electron beams. The drop was then inspected using the iFLM with the 385 nm LED to locate crystals inside the drop at various Z dimensions. The 385 nm LED was used because it is the only option available in our current system that is near the standard excitation wavelengths for protein aromatic residues. We were able to detect protein crystal fluorescence using the 385 nm LED. The sample was presented normal to the FIB beam and small holes were milled straight down the sample, around the crystal of interest, with the Xenon beam at 4nA for use as “fiducials” for the later correlation step. A comprehensive fluorescence stack of the crystals of interest was acquired with a binning of 2 (pixel size of 240 nm) and a step of 0.5 um (Figure 3B, top panel). This stack was deconvolved using the DeconvolveLab Fiji plugin [28]. An experimental Point Spread Function (PSF) was measured using sub-resolution 100nm TetraSpeck microspheres. The processed PSF used for deconvolution was generated with the Huygens software (https://svi.nl/Huygens-Software). Further preprocessing using the 3D-Correlation Tool (3DCT) [29] was performed: 1- stack reslicing in order to output isometric voxels 240 x 240 x 240 nm, and 2- intensity normalization. Low current FIB (10pA) and low voltage SEM (2 kV) images were acquired at grazing incidence (milling angle 11°) and were used to correlate against the fluorescent stack. 3DCT was used to correlate the SEM/FIB views with the fluorescence images. To do so, the milled holes were located in 2D in the SEM/FIB image and in 3D in the fluorescent stack. In the latter, the crystals of interest were located by delineating them with markers. In our hands, as low as 6 fiducial holes, both visible in fluorescence and SEM/FIB, were enough to correlate the two modalities with an error no less than 5 pixels.

This correlation process was performed during the milling procedure to make sure the final lamellae were on target. During the final steps of milling (when the lamella was a 2-3 µm thick), the correlation precision in Z was no longer enough. Milling was performed from top to bottom and the stage was brought back normal to the E-beam for checking the presence of the crystal at the surface of the lamella. To do so, SEM settings were set to 1.2 kV, 13 pA. These settings allowed scattering contrast between the crystal and the surrounding aqueous solvent. When the contours of the crystal were visible, milling was performed from bottom to top until the final thickness of 300 nm was reached. The xenon plasma beam (30 kV) was used for lamella milling at an angle of 11°. For the first milling step, two boxes (20 x 35 µm) separated by 5 µm 4 nA,. Second milling step a current of 1 nA was used to thin down the lamella to 3.5 µm. Third milling step a current of 0.3 nA was used to narrow the lamella to 10 µm wide (X dimension of the milling boxes) and thin it down to 2 um. Fourth milling step a current of 0.1 nA was used to thin down to 1 µm. Final milling step a current of 30 pA was used to generate a 300 nm thick lamella. The final lamella was 10 µm wide, 20 µm long, and 200 nm thick.

MicroED Data Collection

Grids with milled lamellae were transferred to a cryogenically cooled Thermo-Fisher Scientific Titan Krios G3i TEM. The Krios was equipped with a field emission gun and a Falcon4 direct electron detector, and was operated at an accelerating voltage of 300 kV. A low magnification atlas of the grid was acquired using EPU (Thermo-Fisher) to locate milled lamellae. The stage was translated to the lamellae position and the eucentric height was set. The 100 µm selected area aperture was inserted and centered on the crystal to block background reflections. In diffraction mode, the beam was defined using a 50 µm

C2 aperture, a spotsize of 11, and a beam diameter of 20 μm. MicroED data were collected by continuously rotating the stage at 0.2 ° / s for 400 s, resulting in a rotation range of 80°.

MicroED data processing.

Movies in MRC format were converted to SMV format using MicroED tools [30,31]. The diffraction dataset was indexed and integrated in *XDS* [32]. Integrated intensities from a single crystal were scaled and merged in *XSCALE* [33].

Structure solution and refinement.

Phases for the MicroED reflections were determined by molecular replacement in PHASER using Protein Data Bank (PDB) 6CL7 as the search model [34,35]. The solution was space group $P4_32_12$ and unit cell dimensions 68.26, 68.26, 101.95 (a, b, c) (Å) and 90, 90, 90 (α, β, γ) (°). The first refinement was performed with Coot and phenix.refine [36] using isotropic B-factors, automatic water picking, and electron scattering factors. Occupancies were refined for alternative side chain conformations and SO_4 and calcium were placed in coordination sites. The final refinement used anisotropic B-factors, automatic water picking, and electron scattering factors and resulted in Rwork/Rfree = 0.2442/0.2917 and resolution of 2.1 Å.

References

1. McPherson, A. & Gavira, J. A. Introduction to protein crystallization. *Acta Crystallogr F Struct Biol Commun* **70**, 2–20 (2014).

2. McPherson, A. [5]Crystallization of macromolecules: General principles. *Methods Enzymol* **114**, 112–120 (1985).

3. Bragg, W. H. X-rays and crystals. *Nature* **90**, 219 (1912).

4. Salemme, F. R. A Free Interface Diffusion Technique for the Crystallization of Proteins for X-Ray Crystallography. *Arch. Biochem. Biophys* **151**, 533–539 (1972).

5. McPherson, A. *Preparation and analysis of protein crystals*. (Krieger Publishing Company, 1989).

6. Landau, E. M. & Rosenbusch, J. P. Lipidic cubic phases: A novel concept for the crystallization of membrane proteins. *Proc Natl Acad Sci U S A* **93**, 14532–14535 (1996).

7. Gonen, T. *et al.* Lipid–protein interactions in double-layered two-dimensional AQP0 crystals. *Nature* **438**, 633–638 (2005).

8. Henderson, R. & Unwin, P. N. T. Three-dimensional model of purple membrane obtained by electron microscopy. *Nature* **257**, 28–32 (1975).

9. Schmidt-Krey, I. Electron crystallography of membrane proteins: Two-dimensional crystallization and screening by electron microscopy. *Methods* **41**, 417–426 (2007).

10. Chayen, N. E. & Saridakis, E. Protein crystallization: From purified protein to diffraction-quality crystal. *Nat Methods* **5**, 147–153 (2008).

11. Delmar, J. A., Bolla, J. R., Su, C.-C. & Yu, E. W. Chapter Eighteen Crystallization of Membrane Proteins by Vapor Diffusion. *Methods Enzymol* **557**, 363–392 (2015).

12. Shi, D., Nannenga, B. L., Iadanza, M. G. & Gonen, T. Three-dimensional electron crystallography of protein microcrystals. *Elife* **2**, e01345 (2013).

13. Jones, C. G. *et al.* The CryoEM Method MicroED as a Powerful Tool for Small Molecule Structure Determination. *ACS Cent Sci* **4**, 1587–1592 (2018).

14. Sawaya, M. R. *et al.* Ab initio structure determination from prion nanocrystals at atomic resolution by MicroED. *Proceedings of the National Academy of Sciences* **113**, 11232–11236 (2016).

15. Xu, H. *et al.* Solving a new R2lox protein structure by microcrystal electron diffraction. *Sci Adv* **5**, eaax4621 (2019).

16. Gruene, T. *et al.* Rapid Structure Determination of Microcrystalline Molecular Compounds Using Electron Diffraction. *Angewandte Chemie International Edition* **57**, 16313–16317 (2018).

17. Mu, X., Gillman, C., Nguyen, C. & Gonen, T. An Overview of Microcrystal Electron Diffraction (MicroED). *Annu Rev Biochem* **90**, 431–450 (2021).

18. Nannenga, B. L. & Gonen, T. The cryo-EM method microcrystal electron diffraction (MicroED). *Nat Methods* **16**, 369–379 (2019).

19. Hattne, J. *et al.* MicroED data collection and processing. *Acta Crystallogr A Found Adv* **71**, 353–360 (2015).

20. Martynowycz, M. W. *et al.* MicroED structure of the human adenosine receptor determined from a single nanocrystal in LCP. *Proc Natl Acad Sci U S A* **118**, 1–5 (2021).

21. Martynowycz, M. W., Khan, F., Hattne, J., Abramson, J. & Gonen, T. MicroED structure of lipid-embedded mammalian mitochondrial voltage-dependent anion channel. *Proc Natl Acad Sci U S A* **117**, 32380–32385 (2020).

22. Martynowycz, M. W. *et al.* A robust approach for MicroED sample preparation of lipidic cubic phase embedded membrane protein crystals. *Nat Commun* **14**, 1086 (2023).

23. Sartori, N., Richter, K. & Dubochet, J. Vitrification depth can be increased more than 10-fold by high-pressure freezing. *J Microsc* **172**, 55–61 (1993).

24. Nannenga, B. L. & Gonen, T. The cryo-EM method microcrystal electron diffraction (MicroED). *Nat Methods* **16**, 369–379 (2019).

25. Nannenga, B. L., Shi, D., Hattne, J., Reyes, F. E. & Gonen, T. Structure of catalase determined by MicroED. *Elife* **3**, e03600 (2014).

26. Yonekura, K., Kato, K., Ogasawara, M., Tomita, M. & Toyoshima, C. Electron crystallography of ultrathin 3D protein crystals: Atomic model with charges. *Proceedings of the National Academy of Sciences* **112**, 3368–3373 (2015).

27. Li, X., Zhang, S., Zhang, J. & Sun, F. In situ protein micro-crystal fabrication by cryo-FIB for electron diffraction. *Biophys Rep* **4**, 339–347 (2018).

28. Sage, D. *et al.* DeconvolutionLab2: An open-source software for deconvolution microscopy. *Methods* **115**, 28–41 (2017).

29. Heymann, J. A. W. *et al.* Site-specific 3D imaging of cells and tissues with a dual beam microscope. *J Struct Biol* **155**, 63–73 (2006).

30. Martynowycz, M. W., Zhao, W., Hattne, J., Jensen, G. J. & Gonen, T. Collection of Continuous Rotation MicroED Data from Ion Beam-Milled Crystals of Any Size. *Structure* **27**, 545-548.e2 (2019).

31. Hattne, J. *et al.* MicroED data collection and processing. *Acta Crystallogr A Found Adv* **71**, 353–360 (2015).

32. Kabsch, W. XDS. *Acta Crystallogr D Biol Crystallogr* **66**, 125–132 (2010).

33. Kabsch, W. Integration, scaling, space-group assignment and post-refinement. *Acta Crystallogr D Biol Crystallogr* **66**, 133–144 (2010).

34. McCoy, A. J. *et al.* Phaser crystallographic software. *J Appl Crystallogr* **40**, 658–674 (2007).

35. Hattne, J. *et al.* Analysis of Global and Site-Specific Radiation Damage in Cryo-EM. *Structure* **26**, 759--766.e4 (2018).

36. Afonine, P. V. *et al.* Towards automated crystallographic structure refinement with phenix.refine. *Acta Crystallogr D Biol Crystallogr* **68**, 352–367 (2012).

Chapter 5: Eliminating the missing cone challenge through innovative approaches

Authors

Cody Gillman[1,2], Guanhong Bu[1], Emma Danelius[1], Johan Hattne[1], Brent Nannenga[3,4], Tamir Gonen[1,2, 5]

Affiliations

[1] Departments of Biological Chemistry and Physiology, University of California, Los Angeles, CA, USA.

[2] Molecular Biology Institute, University of California, Los Angeles, Los Angeles, CA 90095, USA.

[3]Chemical Engineering, School for Engineering of Matter, Transport and Energy, Arizona State University, Tempe, AZ, USA.

[4]Center for Applied Structural Discovery, Biodesign Institute, Arizona State University, Tempe, AZ, USA. brent.nannenga@asu.edu.

[5] Howard Hughes Medical Institute, University of California, Los Angeles CA, USA.

* To whom correspondence should be sent T.G. tgonen@g.ucla.edu

Keywords

Microcrystal electron diffraction, MicroED, CryoEM, FIB milling, cryogenic freezing, plasma FIB/SEM, pFIB, suspended drop crystallization, membrane protein, missing conve

Abstract

Microcrystal electron diffraction (MicroED) has emerged as a powerful technique for unraveling molecular structures from microcrystals too small for X-ray diffraction. However, a significant hurdle arises when plate-like crystals are obtained and consistently orient themselves flat on the electron microscopy grid, systematically limiting data acquisition and resulting in what is known as a missing cone of information. We recently introduced a novel crystallization strategy called suspended drop crystallization, and proposed that this method could effectively address the challenge of preferred crystal orientation. Here we demonstrate the success of the suspended drop crystallization approach in eliminating the missing cone in a sample known to suffer from preferred orientation: the COVID-19 protease MPro. This innovative solution proves indispensable for crystals experiencing preferred orientations, unlocking new possibilities for structure determination in MicroED workflows.

Introduction

Microcrystal electron diffraction (MicroED) is a cryogenic electron microscopy (CryoEM) method in which vanishingly small crystals are used for structure determination by electron diffraction (Shi *et al.*, 2013). With this method, data are collected on a fast camera as a movie while the sample is continuously rotated (Nannenga *et al.*). This in turn allows the data to be processed using standard crystallographic software. MicroED has been applied to small molecules, natural products, materials as well as soluble and membrane proteins and is growing in its popularity and applications in various scientific fields (Mu *et al.*, 2021). However, certain crystal morphologies pose a specific challenge: when crystals

are flat and assume a preferred orientation, it leads to the occurrence of a missing cone of information irrespective of the number of data sets merged. This challenge is not exclusive to MicroED; it also manifests in cryotomography. It is a well-known issue in transmission electron microscopy, attributed to the experimental design of the stage with the sample in relation to the incoming electrons.

The missing cone can be eliminated if crystals are randomly oriented on the grid. The first demonstration was reported in 2013 (Shi *et al.*). In that example, data sets from 3 crystals were combined to achieve 100% completeness with high redundancy. The high symmetry of the lysozyme packing of course helped but ultimately no single crystal delivered 100% complete data and instead 3 data sets were merged. In later examples using several different proteins with varying symmetries showed that even a single crystal can yield 100% completeness as for example in the case of proteinase K (Martynowycz *et al.*, 2023) and the Adenosine A2a receptor (Martynowycz *et al.*, 2023). When the symmetry is low, for example P1, many more data sets need to be merged. In the case of neurodegenerative peptoid crystals sometimes up to 16 data sets were merged(Griner *et al.*, 2019; Gallagher-Jones *et al.*, 2018). In the case of triclinic lysozyme similarly 16 crystals were merged (Clabbers *et al.*, 2022) and in the case of the human G-protein coupled receptor the vasopressin receptor, also crystallized in P1, 16 data sets had to be merged to yield high completeness(Shiriaeva *et al.*, 2023).

Some crystals adopt a preferred orientation on the grid where one crystallographic axis is always oriented the same with respect to the electron beam. Under such circumstances, no matter the number of data sets merged and no matter the crystal symmetry one always ends up with a systematic missing cone of data. All examples of

2D crystals are included in this example because all 2D crystals adopt a preferred orientation on the EM grid. And indeed for such samples the maximum achievable completeness is ~86%. Some 3D crystals display similar behavior such as the Calcium ATPase (Yonekura *et al.*, 2015), HIV Gag (Purdy *et al.*, 2018) and perhaps the most famous example being Catalase (Matricardi *et al.*). Catalase was the second protein determined by MicroED and reported back in 2014 (Nannenga *et al.*, 2014). A single crystal yielded high completeness but even merging data from 5 additional crystals could not eliminate the missing cone. That's because catalase, like the other examples above, forms rectangular crystals that adopt a preferred orientation on the grid with the c* axis always being parallel to the electron beam. A severe missing cone typically results in elongated densities along the c* axis or in missing or disjoined density which cannot be recovered.

Recently, we reported a new method for crystal growth called suspended drop crystallization (Gillman *et al.*, 2023). With this approach crystals grow in suspension directly on an EM grid without any support film. Because no support film is present, we postulated that crystals would no longer be able to adopt a preferred orientation and therefore this approach could eliminate the missing cone problem. Consistent with the above postulate, we now show that indeed the missing cone can be eliminated, and a complete data set can be obtained with a suspended drop crystallization approach. We demonstrate this using a sample that is known to adopt preferential orientations, namely the COVID-19 main protease MPro.

Methods and Materials

Design of Mpro expression construct

The gene encoding the full-length SARS-COV-2 Mpro was cloned into the pGEX-6P-1 vector. The construct fused with an N-terminal self-cleaving GST tag and a C-terminal His affinity tag downstream of a precission protease cleavage site.

Protein expression and purification of Mpro

The *E. coli* strain Rosetta2 (DE3) was transformed with the expression plasmid for protein expression. An overnight culture was grown in terrific broth (TB) at 37 ˚C and used for inoculating 1 L of Terrific Broth. The culture was incubated at 37 ˚C and 225 rpm. Protein expression was induced by 0.5 mM isopropyl β-d-1-thiogalactopyranoside (IPTG) when the OD_{600} reached 0.7. Expression was allowed for 16 h at 18 ˚C and 225 rpm. The cell pellet was harvested at 8,000 x g and kept at -20 ˚C until use. The frozen cell pellet was thawed at 4 ˚C in lysis buffer (50 mM HEPES-NaOH pH 7.5, 2 mM DTT, 2 mM EDTA, 2 mM EGTA, 0.1 mg/mL lysozyme and 0.1 mg/mL DNase I). Cells were lysed by sonication at 70% amplitude for 5 min. The cell debris and unbroken cells were removed by centrifuging at 12,000 x g and 4 ˚C. The supernatant was directly loaded into a gravity column filled with 1 mL TALON resin (TaKaRa) pre-equilibrated with the binding buffer (20 mM HEPES-NaOH pH 7.5, 100 mM NaCl and 1 mM DTT). The column was washed with 25 mL wash buffer (20 mM HEPES-NaOH pH 7.5, 100 mM NaCl, 1 mM DTT and 10 mM imidazole), then washed with 10 mL precission protease cleavage buffer (50 mM Tris-HCl pH 8.2, 150 mM NaCl and 1 mM DTT). Approximately 0.2 mg precission protease in 3 mL cleavage buffer was directly added into the TALON resin slurry. The resin slurry was incubated at 4 ˚C for over 16 h with gentle shaking. The tag-cleaved Mpro was collected

in fractions while flowing off the resin. The purified protein was concentrated to 0.6 mL using a 10 kD cut-off Amicon Ultra centrifugal filter (Millipore). Precipitation was removed by centrifuging at 20,000 x g. Sample was then loaded into a Superdex 200 Increase 10/300 GL column (Cytiva) pre-equilibrated with the SEC buffer (20 mM HEPES-NaOH pH 7.8, 100 mM NaCl, 1 mM DTT and 1 mM EDTA). Peak fractions were pooled, concentrated using an Amicon Ultra centrifugal filter with 10 kD cut-off (Millipore), and stored at -80 ˚C until use.

EM sample preparation of MPro crystals

For crystals in the preferred orientation, EM samples were prepared following previously published protocol (Martynowycz *et al.*, 2021). Typically, carbon-coated (Quantifoil R 2/2) 200-mesh copper grids (Electron Microscopy Sciences) were negatively glowed discharged at 15 mA for 45 s using a PELCO easiGlow (Ted Pella). The grids were then loaded into a Leica EM GP2 plunge freezer (Leica Microsystems) set to 20 ˚C and 95% humidity. Using a micropipette, 2 µL of the crystal drop was transferred to the grid, which was then blotted for 20 s, and finally plunged into liquid ethane.

For the suspended-drop grids, the crystal slurry was added directly to a 150 mesh count support-free gold gilder grid (Ted Pella) that was clipped into an autogrid cartridge (Thermo-Fisher). To transfer a minimal amount of sample to the grid, the sample was first aspirated into a pipet tip and the tip was gently applied and dragged across the surface of the grid. Sample transferred to the grid bars and was retained by surface tension. The grid was finally plunged into liquid ethane and stored under liquid nitrogen until further use.The grids supporting the suspended crystal drops were blotted with filter paper from

the edge for 2 s before manually plunging into liquid ethane. All grids were stored under liquid nitrogen until use.

Generating lamellae of Mpro blotted crystals and suspended crystals

The vitrified grids were transferred into a Thermo-Fisher Aquilos FIB/SEM instrument operating at cryogenic temperature. Whole-grid atlases were recorded with the SEM at 5 kV and 1.6 pA using MAPS software. To protect the samples from the damaging ion and electron beams, the grids were coated with platinum by sputter coating (Martynowycz *et al.*, 2019*b*). Individual crystals from blotted grids and suspended drops were respectively identified and aligned to eucentric height using MAPS software. FIB milling proceeded as described (Martynowycz *et al.*, 2019*b*,*a*).

A typical crystal identified on the blotted grids was tilted to a milling angle of 33°. Rough milling used an ion beam current of 300 pA to produce a 4 µm thick and 5 µm wide lamella. For fine milling, a FIB current of 100 pA was used to reduce the thickness of lamella to 3 µm. Polishing proceeded at an ion beam current of 50 pA until the thickness reached approximately 350 nm. The final lamella was approximately 3 µm wide. Milling suspended drop samples was similar to the previously mentioned steps with slight modification: the sample was tilted to a milling angle of 20°, and the ion beam current for rough, fine, and final millingwas set to 3 nA, 500 pA, and 100 pA, respectively.

MicroED data collection

The grid hosting the milled lamellae were rotated 90° and transferred to a cryogenically cooled Thermo-Fisher Scientific Titan Krios G3i TEM. The Krios was equipped with a field emission gun operating at an accelerating voltage of 300 kV, a Falcon4i direct electron detector, and a Selectris energy filter (Thermo-Fisher). A low magnification atlas of the

grid was acquired using EPU (Thermo-Fisher) to locate all milled lamellae. The stage was moved to the lamella position and while in the “View” settings (SA 3,600x) of SerialEM (Mastronarde, 2003), the eucentric height was set. In the “Record” settings, the following parameters were set for the electron beam in diffraction mode: a beam size of 20 µm in diameter, a spotsize of 11, and a C2 aperture of 50 µm. These settings resulted in an electron dose rate of approximately 0.0025 e-/(Å^2·s). MicroED datasets were collected in counting mode and electron event representation (EER) format using the “Record” mode of SerialEM following the protocol described in previously published work (Shiriaeva *et al.*, 2023). An in-house developed script was applied to insert the Selectris energy filter set to a slit width of 20 eV and the selected area aperture of ~2 µm in diameter and automatically collect continuous-rotation MicroED datasets for 420 s in EER format. A mdoc file and log file would be generated after each data collection to provide metadata and parameters to use for data processing. Typical datasets from blotted crystals and suspended-drop grids were collected by continuously rotating the stage at 0.19 ° / s for 420 s, resulting in a rotation range of 80°

MicroED data conversion

Movies in EER format were converted to SMV format using the latest version of MicroED tools (Martynowycz *et al.*, 2019*a*; Hattne *et al.*, 2015), which are publicly available from the UCLA Gonen laboratory website (https://cryoem.ucla.edu/downloads/snapshots).

isotropic B-factors, automatic water picking, and electron scattering factors.

MicroED data processing and structure determination of MPro

The MicroED datasets were loaded into XDS (Kabsch, 2010*b*) for indexing and integration. High quality datasets including the missing cone were scaled and merged in XSCALE (Kabsch, 2010*a*) and converted to MTZ format with supplemental 5% free R column in XDSCONV (Kabsch, 2010*b*). The MicroED data were phased by molecular replacement in Phaser (McCoy *et al.*, 2007) using the coordinates of an X-ray structure of Mpro deposited in the protein data bank (PDB entry 7K3T [10]). The solution was in space group C2 with the unit cell parameters of 115.54, 55.53, 45.37 (a, b, c) (Å), 90, 101.074, 90 (α, β, γ) (°). Structures were refined in Coot (Emsley *et al.*, 2010) and Phenix_refine (Afonine *et al.*, 2012).

Results

Preparation of suspended crystal drops

To reduce FIB milling time and thus the possibility of damaging the crystals in the suspended drops, it was important to prepare samples with minimal volume. Pipetting 0.3 – 0.5 μL of crystal slurry onto the support-free grid and spreading with a micro-brush was satisfactory, but pipetting such small volumes gave inconsistent results using standard micropipettes. The second application method explored was preparing a droplet of the crystal slurry on a siliconized coverslip and gently touching a support-free grid to the surface of the crystal slurry, which transferred a fraction of the drop to the grid bars. Although this improved the consistency of sample preparation, spreading with a micro-brush was still required. It was finally discovered that gently touching a pipet tip filled with the crystal slurry to the grid bars allows a minimal volume of the slurry to transfer by capillary motion. This method was highly reproducible and efficient leading to very small

volume. Immediately after application, the samples were manually plunged into liquid ethane or nitrogen. For Mpro, the grid was carefully blotted from the side after application to further reduce the volume of the sample. Samples were stored under liquid nitrogen until use.

Preparation of crystal lamellae of suspended Mpro crystals

For the Mpro suspended crystal sample, a cryogenically cooled Aquilos FIB/SEM (Thermo-Fisher) was used for lamellae milling. The grids were coated with platinum by sputter coating to protect the sample when SEM imaging and milling with the gallium ion FIB. Because the suspended drop of Mpro crystals was briefly blotted, only a minimal volume of sample was retained by the grid bars, which allowed for crystal morphological features to be observed and targeted. A 3 μm wide and 350 nm thick sample lamella was generated to thin the crystal of interest. The gallium ion milling current was set to 3 nA for rough milling and gradually decreased to 100 pA for final thickness milling and polishing.

Collection of MicroED data

All crystalline lamellae samples were subsequently transferred to a 300kV cryo-TEM for MicroED data collection using a Falcon4i camera operating in counting mode and a Selectris energy filter inserted. The lamellae were brought to eucentric height and manually scanned by sequentially previewing electron diffraction at different points along the length of the lamellae until a crystal site was located. MicroED data were collected as described previously (Hattne *et al.*, 2015) with modifications described in Materials and Methods (Figure 5.1).

Eliminating the missing cone in the MicroED structure of Mpro

For MPro, we collected data for both crystals blotted on support film (showing preferred orientation) and in suspension. Processing was accomplished in XDS (Kabsch, 2010*b*), and XSCALE (Kabsch, 2010*a*) was employed for dataset merging. We produced two separate datasets: one called “preferred orientation” and one called “missing cone eliminated”. These datasets were processed separately during phasing and refinement, and the observed reflections, statistics, and refined maps were subsequently compared. Mpro was phased using PDB entry 7K3T (Andi *et al.*, 2022) as the search model. The phased maps were refined in Phenix Refine (Afonine *et al.*, 2012). Data processing statistics for both preferred orientation and missing cone eliminated MPro datasets are in Table 5.1.

Phenix *2D Data Viewer* was used to render observed reflections in reciprocal space for both the preferred orientation datasets and the missing cone eliminated datasets. For Mpro, viewing 2D slices along the *L* axis, the missing cone of data was also clearly recovered (Figure 5.2a, b), consistent with the total number of unique reflection increasing from 27,905 to 14,825 (Table 5.1). Eliminating the missing cone of data was predicted to improve dataset completeness and the crystallographic correlation coefficient of half-sets of data ($CC_{1/2}$) for these two example proteins. The completeness across the various resolution shells for Mpro significantly improved after merging the missing cone dataset with the preferred orientation dataset (Figure 5.3a), corresponding with the overall dataset completeness increasing from 59.1 to 95.5% (Table 5.1). The $CC_{1/2}$ in both low- and high-resolution shells improved as well for Mpro (Figure 5.3b).

The density maps that were produced using the preferred orientation datasets and missing cone eliminated datasets were finally compared (Figure 5.4). Once the missing cone of reflections was eliminated, many regions of the maps that were originally irresolvable now showed continuous and refined densities that were easy to interpret. Several instances are illustrated wherein the improved maps facilitated precise positioning of amino acid sidechains during the construction of the molecular models.

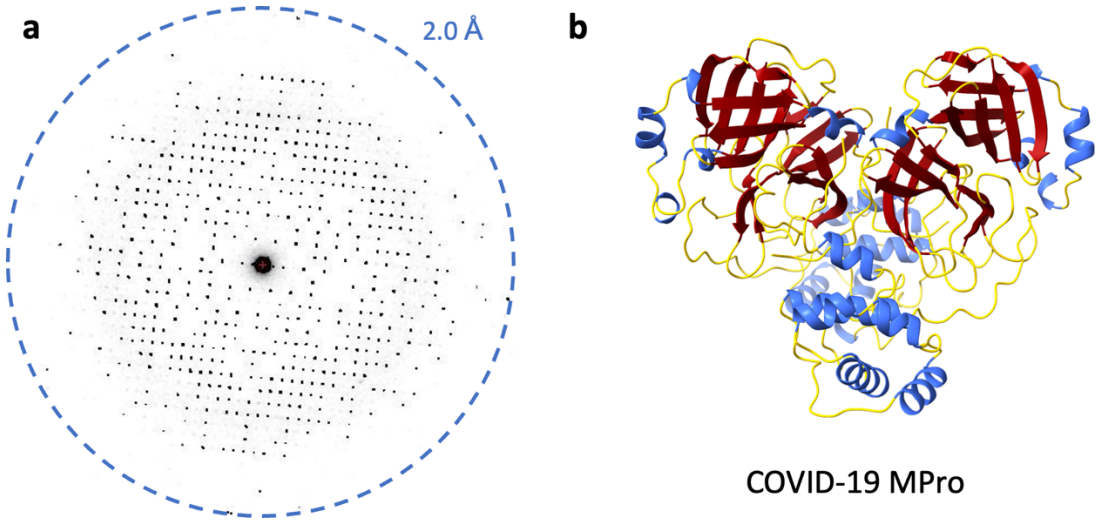

Figure 5.1. MicroED of Mpro. (a) Electron diffraction frame acquired from Mpro. (b) Ribbon model of Mpro.

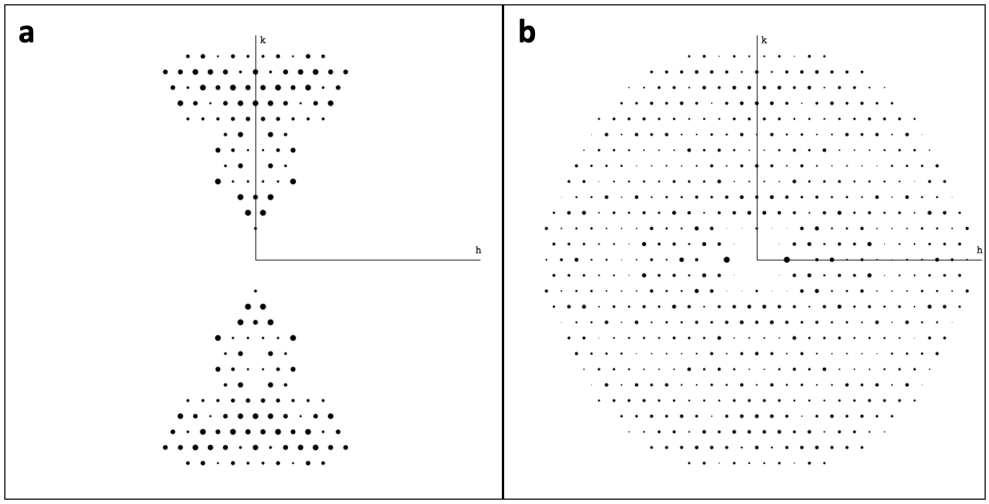

Figure 5.2. Recovery of missing reflections in the MicroED dataset Mpro. (a) A 2D slice of observed reflections in the preferred orientation dataset viewed along the l axis. (b) A 2D slice of observed reflections in the missing cone eliminated dataset viewed along the l axis.

Table 5.1. Preferred orientation vs. missing cone-eliminated dataset statistics for Mpro

COVID-19 MPro

Data Statistic	**Preferred Orientation**	**Missing Cone Eliminated**
# of crystals	1	4
Space group	C2	C2
a, b, c (Å)	115.54, 55.53, 45.37	115.54, 55.53, 45.37
α, β, ɣ (°)	90, 101.074, 90	90, 101.074, 90
Resolution (Å)	2.15	2.15
# of reflections	27,905	123,734
Unique reflections	9,189	14,825
I/σI	4.86	5.63
$CC_{1/2}$ (%)	98.8	98.7
Completeness (%)	**59.1**	**95.5**
Rwork (%)	22.81	22.63
Rfree (%)	27.12	25.87
RMS bond (Å)	0.014	0.002
RMS angle (°)	1.556	0.477
Ramachandran favored (%) /outlier (%)	95.07/0.66	96.38/0

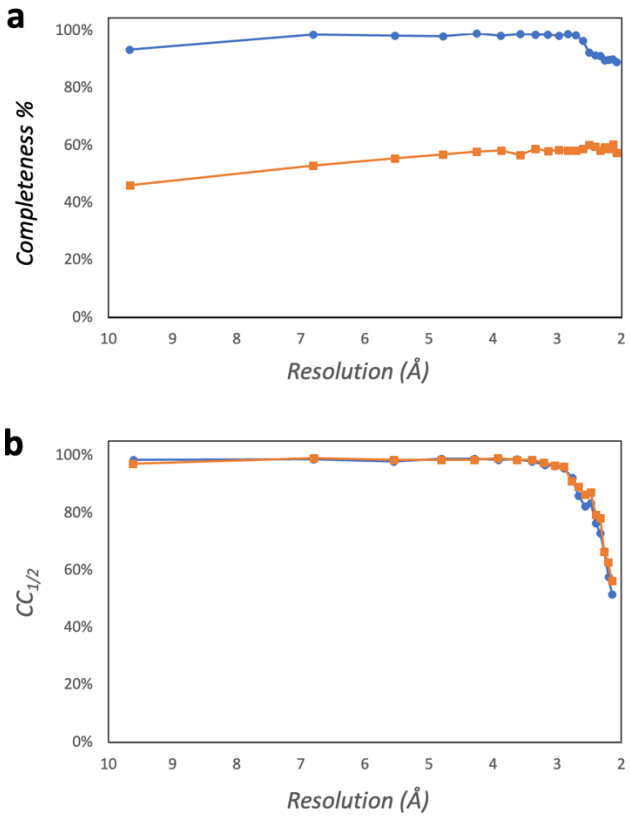

Figure 5.3. Statistics for preferred orientation data vs. missing cone-eliminated data for MPro. (a) Completeness (%) of Mpro, and (d) CC1/2 (%) of MPro as functions of Resolution (Å). Orange = preferred orientation data, Blue = missing cone eliminated data.

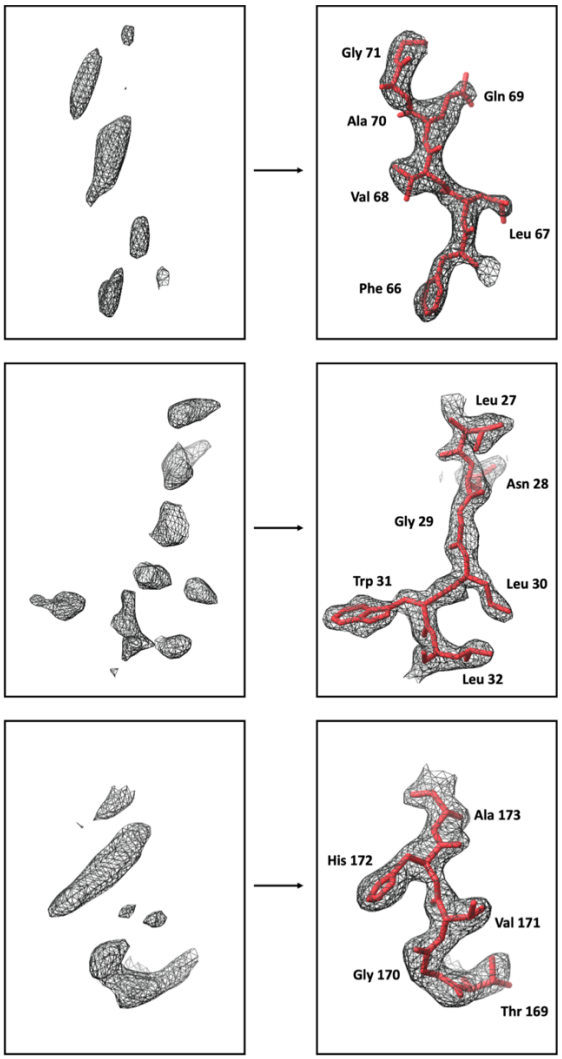

Figure 5.4. Density improvements upon completion of the reciprocal space. Several regions that exhibit significant density improvement are presented. 2mFo-DFc maps are all contoured at 1.2 σ and 2 Å carve. On the left in each panel, the preferred orientation map density (uninterpretable density) is compared to that for the missing cone eliminated (interpretable density).

Conclusions

Here, we report a method that enables direct targeting and capturing of the critical missing cone of MicroED data for crystals that adopt a systematic preferred orientation on the EM grid. Suspended crystals of the covid-19 main protease MPro were used as test cases. In both cases, crystals grew as rectangular plates that would normally adopt a preferred orientation on the carbon support film of the grid. However, the absence of a carbon support film precluded these crystal plates from having a surface to align with and were effectively frozen in random orientations as postulated in earlier studies (Gillman et al. 2023). FIB milling allowed thinning the surrounding material and the crystal to a thickness that was amenable to MicroED data collection.

The missing cone creates a substantial bottleneck in structure solution for crystals that adopt a preferred orientation. Addressing this challenge involves the laborious tasks of collecting, processing, and screening numerous datasets. In many instances, despite well-diffracting crystals, if the missing reflections are systematic, no amount of data collection and merging could improve dataset completeness. As a consequence, determining a structure may become impractical as densities appear elongated or disjoint and may be difficult to interpret. The approach presented here indicates that the preferred orientation bias can be eliminated by removal of the support film. When crystals of MPro were suspended and exposed for MicroED data collection by FIB milling, indeed complete datasets could be attained. Once the missing cone was eliminated, the densities became complete and interpretable, making structure building and refinement simple.

Crystals with a systematic preferential orientation are not common. We estimate that less than 10% of all protein crystals would fall under this category. The majority of

samples will likely adopt random orientations on the grid and may also have higher crystal symmetry. In such cases, even a single nanocrystal can be sufficient for a complete structure by MicroED. This has been observed in several examples already including for crystals of soluble proteins like lysozyme (Martynowycz & Gonen, 2021) and proteinase K (Martynowycz *et al.*, 2022), as well as samples of membrane proteins such as the the GPCR Adenosine A2a receptor (Martynowycz *et al.*, 2023). In these cases, FIB milling was critical for obtaining high quality data as the milling delivered a uniform crystalline lamellae. While the suspended drop crystallization approach described here eliminated the preferential orientation problem for MicroED, the missing cone problem remains a prevalent issue in cryotomography (Barth *et al.*, 1988). Even for single particle reconstructions, particles may preferentially orient at the water-air interface (Glaeser & Han, 2017) and innovative approaches may be needed to eliminate the preferential orientation problem.

As the methodologies for MicroED sample preparation are improved and continue to evolve, we anticipate the method to deliver structures for samples that remain beyond the technological reach of other structural biology methods.

Acknowledgments

The authors would like to thank Dr. Steve Halaby for early work on MPro. This study was supported by the National Institutes of Health P41GM136508 and the Department of Defense HDTRA1-21-1-0004. The Gonen laboratory is supported by funds from the Howard Hughes Medical Institute.

References

Afonine, P. V., Grosse-Kunstleve, R. W., Echols, N., Headd, J. J., Moriarty, N. W., Mustyakimov, M., Terwilliger, T. C., Urzhumtsev, A., Zwart, P. H. & Adams, P. D. (2012). *Acta Crystallogr D Biol Crystallogr* **68**, 352–367.

Andi, B., Kumaran, D., Kreitler, D. F., Soares, A. S., Keereetaweep, J., Jakoncic, J., Lazo, E. O., Shi, W., Fuchs, M. R., Sweet, R. M., Shanklin, J., Adams, P. D., Schmidt, J. G., Head, M. S. & McSweeney, S. (2022). *Sci Rep* **12**, https://doi.org/10.1038/S41598-022-15930-Z.

Barth, M., Bryan, R. K., Hegerl, R. & Baumeister, W. (1988). *Scanning Microsc Suppl* **2**, 277–284.

Bruhn, J. F., Scapin, G., Cheng, A., Mercado, B. Q., Waterman, D. G., Ganesh, T., Dallakyan, S., Read, B. N., Nieusma, T., Lucier, K. W., Mayer, M. L., Chiang, N. J., Poweleit, N., McGilvray, P. T., Wilson, T. S., Mashore, M., Hennessy, C., Thomson, S., Wang, B., Potter, C. S. & Carragher, B. (2021). *Front Mol Biosci* **8**, 648603.

Clabbers, M. T. B., Martynowycz, M. W., Hattne, J. & Gonen, T. (2022). *J Struct Biol X* **6**, 100078.

Emsley, P., Lohkamp, B., Scott, W. G. & Cowtan, K. (2010). *Acta Crystallogr D Biol Crystallogr* **66**, 486–501.

Foroughi, L. M., Kang, Y. N. & Matzger, A. J. (2011). *Cryst Growth Des* **11**, 1294–1298.

Gallagher-Jones, M., Glynn, C., Boyer, D. R., Martynowycz, M. W., Hernandez, E., Miao, J., Zee, C.-T., Novikova, I. V, Goldschmidt, L., McFarlane, H. T., Helguera, G. F., Evans, J. E., Sawaya, M. R., Cascio, D., Eisenberg, D. S., Gonen, T. & Rodriguez, J. A. (2018). *Nat Struct Mol Biol* **25**, 131–134.

Gillman, C., Nicolas, W. J., Martynowycz, M. W. & Gonen, T. (2023). *IUCrJ* **10**, https://doi.org/10.1107/s2052252523004141.

Glaeser, R. M. & Downing, K. H. (1993). *Ultramicroscopy* **52**, 478–486.

Glaeser, R. M. & Han, B.-G. (2017). *Biophys Rep* **3**, 1–7.

Griner, S. L., Seidler, P., Bowler, J., Murray, K. A., Yang, T. P., Sahay, S., Sawaya, M. R., Cascio, D., Rodriguez, J. A., Philipp, S., Sosna, J., Glabe, C. G., Gonen, T. & Eisenberg, D. S. (2019). *Elife* **8**, e46924.

Hattne, J., Reyes, F. E., Nannenga, B. L., Shi, D., Cruz, M. J. de la, Leslie, A. G. W. & Gonen, T. (2015). *Acta Crystallogr A Found Adv* **71**, 353–360.

Hattne, J., Shi, D., Glynn, C., Zee, C.-T., Gallagher-Jones, M., Martynowycz, M. W., Rodriguez, J. A. & Gonen, T. (2018). *Structure* **26**, 759--766.e4.

Kabsch, W. (2010*a*). *Acta Crystallogr D Biol Crystallogr* **66**, 133–144.

Kabsch, W. (2010*b*). *Acta Crystallogr D Biol Crystallogr* **66**, 125–132.

Martynowycz, M. W., Clabbers, M. T. B., Hattne, J. & Gonen, T. (2022). *Nat Methods* **19**, 724–729.

Martynowycz, M. W., Clabbers, M. T. B., Unge, J., Hattne, J. & Gonen, T. (2021). *Proc Natl Acad Sci U S A* **118**, 1–7.

Martynowycz, M. W. & Gonen, T. (2021). *STAR Protoc* **2**, 100686.

Martynowycz, M. W., Shiriaeva, A., Clabbers, M. T. B., Nicolas, W. J., Weaver, S. J., Hattne, J. & Gonen, T. (2023). *Nat Commun* **14**, 1086.

Martynowycz, M. W., Zhao, W., Hattne, J., Jensen, G. J. & Gonen, T. (2019*a*). *Structure* **27**, 545-548.e2.

Martynowycz, M. W., Zhao, W., Hattne, J., Jensen, G. J. & Gonen, T. (2019*b*). *Structure* **27**, 1594-1600.e2.

Mastronarde, D. N. (2003). *Microscopy and Microanalysis* **9**, 1182–1183.

Matricardi, V. R., Moretz, R. C. & Parsons, D. F. (1972). *Science (1979)* **177**, 268–270.

McCoy, A. J., Grosse-Kunstleve, R. W., Adams, P. D., Winn, M. D., Storoni, L. C. & Read, R. J. (2007). *J Appl Crystallogr* **40**, 658–674.

Mu, X., Gillman, C., Nguyen, C. & Gonen, T. (2021). *Annu Rev Biochem* **90**, 431–450.

Nannenga, B. L., Shi, D., Hattne, J., Reyes, F. E. & Gonen, T. (2014). *Elife* **3**, e03600.

Nannenga, B. L., Shi, D., Leslie, A. G. W. & Gonen, T. (2014). *Nat Methods* **11**, 927–930.

Purdy, M. D., Shi, D., Chrustowicz, J., Hattne, J., Gonen, T. & Yeager, M. (2018). *Proc Natl Acad Sci U S A* **115**, 13258–13263.

Shi, D., Nannenga, B. L., Iadanza, M. G. & Gonen, T. (2013). *Elife* **2**, e01345.

Shiriaeva, A., Martynowycz, M. W., Nicolas, W. J., Cherezov, V. & Gonen, T. (2023). *Biorxiv: The Preprint Server*.

Stahlberg, H., Biyani, N. & Engel, A. (2015). *Arch Biochem Biophys* **581**, 68–77.

Sumner, J. B. & Dounce, A. L. (1937). *Science (1979)* **85**, 366–367.

Yonekura, K., Kato, K., Ogasawara, M., Tomita, M. & Toyoshima, C. (2015). *Proceedings of the National Academy of Sciences* **112**, 3368–3373.

Chapter 6: The structure of the neurotoxin palytoxin determined by MicroED

Authors

Cody Gillman[1,2], Khushboo Patel[1], Johan Unge[1], Tamir Gonen[1,2,3,4*]

Affiliations

[1] Department of Biological Chemistry, University of California, Los Angeles CA, USA

[2] Molecular Biology Institute, University of California, Los Angeles CA, USA

[3] Department of Physiology, University of California, Los Angeles CA, USA

[4] Howard Hughes Medical Institute, University of California, Los Angeles CA, USA

* To whom correspondence should be sent T.G. tgonen@g.ucla.edu

Keywords

Microcrystal electron diffraction, MicroED, CryoEM, FIB milling, FIB/SEM, neurotoxin, ATPase

Abstract

Palytoxin (PTX) is a potent neurotoxin found in marine animals that can cause serious symptoms such as muscle contractions, haemolysis of red blood cells and potassium leakage. Despite years of research, very little is known about the mechanism of PTX. However, recent advances in the field of cryoEM, specifically the use of microcrystal electron diffraction (MicroED), have allowed us to determine the structure of PTX. It was discovered that PTX folds into a hairpin motif and is able to bind to the extracellular gate of Na,K-ATPase, which is responsible for maintaining the electrochemical gradient across the plasma membrane. These findings, along with molecular docking simulations, have

provided important insights into the mechanism of PTX and can potentially aid in the development of molecular agents for detecting and possibly treating cases of PTX exposure.

Introduction

Na,K-ATPase is an essential protein for maintaining proper cell function and is targeted by the potent marine toxin palytoxin (PTX)[1-4]. PTX is a non-proteinaceous natural product that was first isolated from tropical marine corals and later found in dinoflagellates[4–7]. PTX can accumulate to dangerous levels in seafood, leading to serious illness and death in those who consume it [8–11]. Aquarium hobbyists may also be exposed to PTX when mishandling *Palythoa* coral or inhaling aerosolized PTX [12,13]. Exposure to PTX from blooming events of *Ostreopsis* has also caused severe illness and hospitalization [14]. Understanding the structure of PTX and how it binds to Na,K-ATPase is crucial for developing molecular agents that can treat cases of PTX exposure and protect against its toxic effects.

PTX's binding to Na,K-ATPase with high affinity and its ability to convert it into a passive cation pore has serious implications for cellular function and can lead to a range of health effects, including skeletal muscle contractions, heart failure, hemolysis, and platelet aggregation [15–18]. The irreversible depolarization of the cell membrane caused by PTX can also contribute to bone resorption and tumorigenesis [19,20]. With an estimated LD_{50} of 45 ng/kg, the extremely low lethal dose for humans highlights the severity of PTX poisoning [21,22].

The development of anti-PTX molecules that can inhibit the binding of PTX on Na,K-ATPase is crucial for the treatment of PTX exposure. However, very little has been uncovered about the three-dimensional structure of PTX. Many studies have utilized anti-PTX antibodies to investigate PTX [5,23,24]. The structure of PTX when bound to an antibody fragment (scFv) was determined using microcrystal electron diffraction (MicroED)[25,26] at 3.2 Å resolution. This provided valuable information on the binding mode of PTX, which was then used to perform docking simulations to determine the potential binding mode of PTX on Na,K-ATPase. These findings pave the way for the development of molecular agents that can treat cases of PTX exposure by inhibiting the binding of PTX on Na,K-ATPase, and can potentially save many lives.

Results

Characterization of scFv-PTX complex and crystallization

The binding of PTX to scFv was confirmed using size exclusion chromatography (SEC). The shift in the SEC trace of free scFv and PTX-bound scFv indicates the formation of a stable complex (Figure 6.1a). Furthermore, the binding affinity of PTX to scFv was determined using microscale thermophoresis (MST). PTX binds to scFv at a K_D of 2.1 µM (Figure 6.1b).

SEC fractions corresponding to the stable scFv-PTX complex were collected, concentrated to 10 mg/mL, and subjected to sparse matrix crystallization screening to identify crystallization condition hits. The scFv-PTX complex was crystallized by the hanging drop vapor diffusion technique. The well solution contained 27 % Jeffamine ED-

2001 pH 7.0 and 100 mM sodium citrate tribasic dihydrate pH 5.6. The scFv-PTX complex was combined with the well solution at 2:1 (v/v) ratio. The crystals were thin rods that formed in dense bundles (Figure 6.1c). The average size of each crystal was 5 µm x 500 µm. The crystals in the drop were then transferred to an electron microscopy (EM) sample

Figure 6.1. Crystallization of scFv-PTX (a) Overlay of size-exclusion chromatography

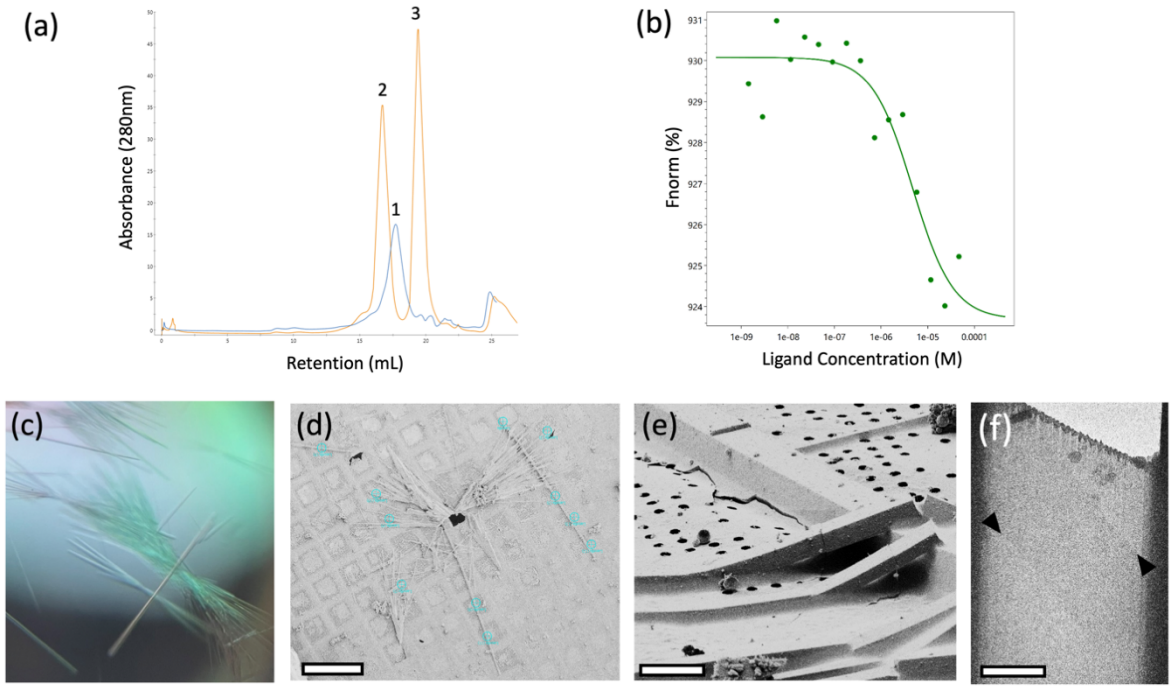

traces of scFv alone (blue trace) and scFv-PTX complex (orange trace). (b) Microscale thermophoresis binding assay confirming binding between scFv-PTX complex. This assay indicates that palytoxin binds to ScFv with K_D = 2.1 µM affinity (c) Light microscope image of scFv-PTX complex crystals (d) SEM image of crystals viewed normal to the grid support surface prior to FIB milling. Scale bar = 200 µm. (e) FIB image of a crystal milling site. Scale bar = 10 µm. (f) Lamella imaged normal to the grid surface in the TEM after milling. Scale bar = 10 µm. The lamella was 200nm thick.

grid, blotted to remove surrounding crystallization media, and vitrified by plunge freezing into liquid ethane. Crystals were stored in liquid nitrogen prior to use.

Preparing crystal lamellae and collection of MicroED data

The crystals that were obtained for this study were too thick for MicroED and needed to be thinned to a thickness that would allow for the transmission of electrons [27]. To achieve this, thin crystal lamellae were produced using a cryogenic focused ion beam scanning electron microscope (FIB/SEM) milling instrument [28]. The process began by loading the EM grid with crystals into the FIB/SEM at cryogenic temperature, followed by imaging using the SEM (Figure 6.1d). Potential milling sites were then observed in the FIB view of the specimen (Figure 6.1e), and the targeted crystal and surrounding media were milled into a thin lamella using the focused gallium ion beam. The final product was a lamella that measured 7 μm wide and 300 nm thick.

After the crystal lamellae were produced, they were transferred to a Titan Krios transmission electron microscope that was operating at 300 kV and cooled cryogenically. The sites of the lamellae were identified using low magnification imaging and adjusted to eucentric height. To ensure high-resolution diffraction, a preview of the lamella was taken (Figure 6.1f and 5.2a). The data were collected using continuous rotation MicroED [26], with a Falcon4 direct electron detector set to counting mode. The highest resolution spots were observed at 3.2 Å resolution.

Determining the MicroED structure of scFv-PTX complex.

MicroED data were converted to standard crystallographic formats using the latest version of conversion software that is freely available on our website (https://cryoem.ucla.edu/microed). The data were indexed and integrated in XDS [29] to a resolution of 3.2 Å, which corresponds to where the CC1/2 was approximately 32%. Reflection data from three crystal lamellae were merged to increase completeness. Phases for the MicroED reflections were determined by molecular replacement using anti-Mc11 scFv (PDB 6QF9)[30] as a search model. The space group was determined to be $P4_12_12$ and unit cell dimensions were 69.95, 69.95, 289.48 (a, b, c) (Å) and 90, 90, 90 (α, β, γ) (°). The structure was refined using electron scattering factors (Table 1) in phenix.refine[31]. The scFv-PTX complex is in dimeric form with one PTX bound to each scFv monomer. The density map contoured at 1.5 σ had continuous density for the

Table 6.1. MicroED structure statistics of scFv-PTX complex.

Data	Parameter	Measure
Data Collection	Accelerating voltage (kV)	300
	Electron source	field emission gun
	Total accumulated exposure ($e^-/Å^2$)	0.64
	Microscope	Thermo Fisher Titan Krios
	Camera	Falcon 4 electron counting
	Rotation rate (deg/sec)	0.2
	Wavelength (Å)	0.019687
Data analysis	No. of crystals	3
	Resolution range (Å)	46.80-3.20
	Space group	$P4_12_12$
	a, c, c (Å)	69.95, 69.95, 289.48
	α, β, ϒ (°)	90, 90, 90
	Reflections, total/unique	260311/12734
	Multiplicity	20.44
	Completeness (%)	99.3
	Mean I/Iσ(I)	2.59
	CC1/2	95.3
	Rwork	0.2830
	Rfree	0.3229

backbone of the scFv and the side chains of the amino acids were also well resolved (Figure 2B). After multiple rounds of refinement, density for PTX was observed for ligand modelling (Figure 2C). The R_{work} and R_{free} of the refinement were 30% and 33%, respectively.

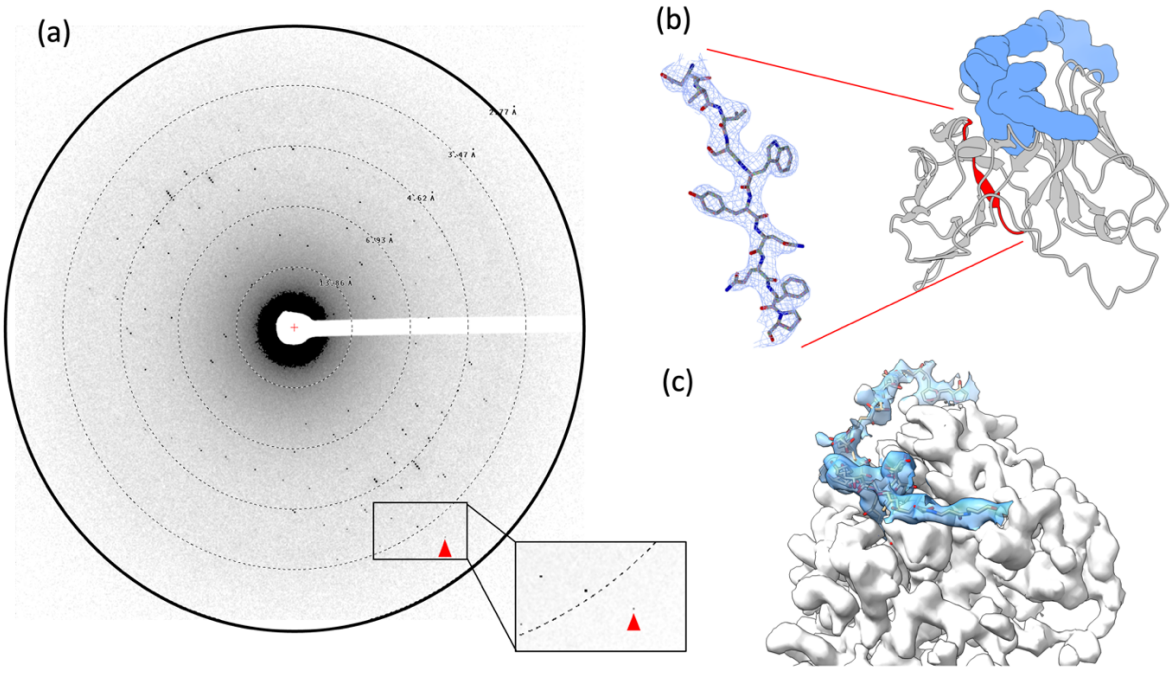

Figure 6.2. The MicroED structure of PTX in complex with scFv. (a) Representative MicroED image. The highest resolution spots were observed at 3.2 Å (red arrowhead). (b) Structure of scFv-PTX complex. The scFv is represented as a cartoon in grey and PTX is represented as a surface model in blue. A beta-strand was selected (red) to provide a sample of the 2mFo–DFc map (blue mesh), which was contoured at 1.5 σ with a 2-Å carve. (c) The overall 2mFo–DFc map of density for both PTX (solid blue) and scFv (solid white) in complex. The density map for PTX was contoured at 1.5 σ.

The scFv creates a binding pocket into which an internal segment of the PTX chain is inserted, forming a hairpin motif (Figure 3). At the deepest part of the pocket, a double ring containing two cyclic ethers of PTX forms hydrogen bonding interactions with residues Y106, E108, and Y169 of the scFv. This double ring of PTX is flanked by two hydrocarbon chains, which run antiparallel to each other inside the binding pocket.

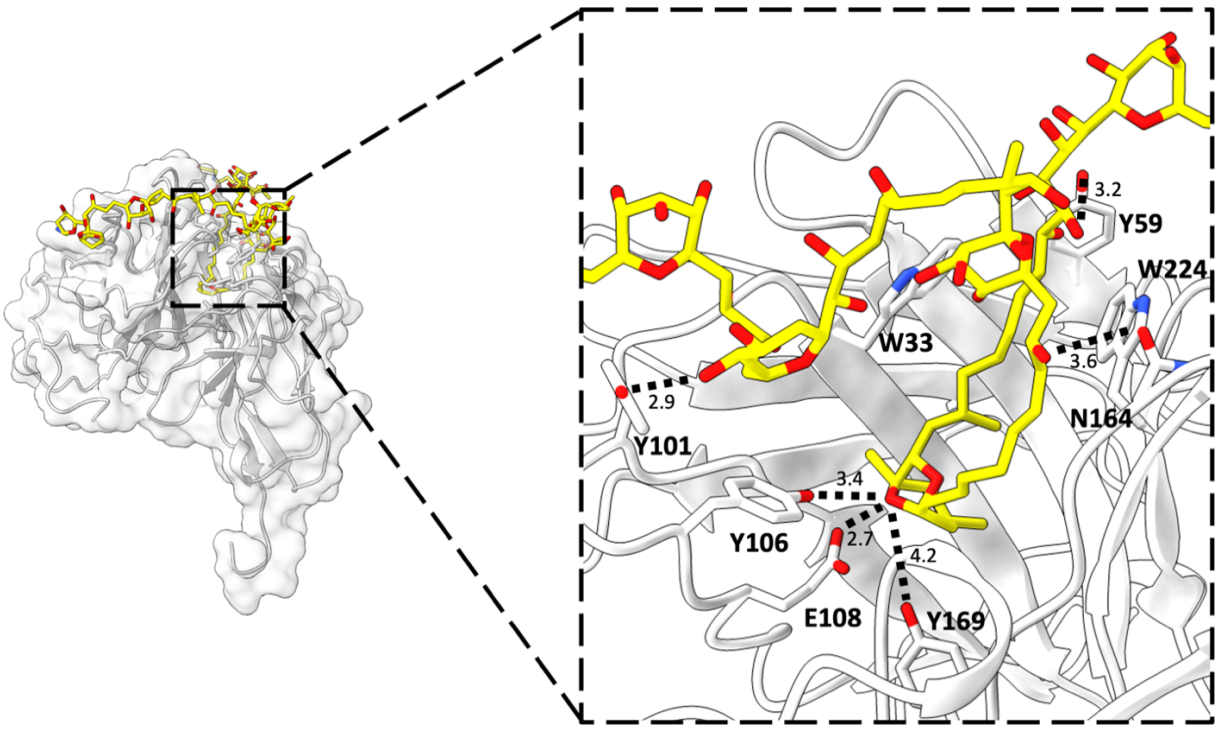

Figure 6.3. Binding interactions between scFv and PTX. An internal region of PTX (represented as yellow carbons and heteroatoms) folds into a hairpin motif and inserts into the scFv binding pocket. A double ring of PTX forms several H-bonding interactions with polar amino acid side chains at the deepest part of the scFv binding pocket (Y106, E108, Y169). Hydrophobic amino acid side chains stabilize the hydrophobic chains of PTX (W33, W224). Additional H-bond interactions take place near the mouth of the binding pocket (N164, Y59, Y101). Bond distances are in units of angstroms.

Hydrophobic amino acid side chains, including F59, W224, and W33 sequester these hydrophobic segments from the external aqueous environment. At the entrance of the binding pocket, PTX forms a network of intramolecular hydrogen bonds and interacts with The two tails of PTX, exposed to the solvent channels of the crystal, were interpreted as traveling away from one another. Importantly, this fitting of full-length PTX demonstrates residues N164, Y59, Y101. Outside the binding pocket, the conformation of the two extended tails of PTX was built into a poorly resolved density. This is because these regions are highly flexible and likely do not form specific bonds at the surface of the scFv. that PTX can fit in the crystal packing without steric clashes, but should be interpreted carefully as the density in this region is poor.

Molecular docking

The MicroED structure we determined of PTX in the scFv-PTX complex was used to investigate the potential binding of PTX to Na,K-ATPase protein using molecular docking simulations (Figure 6.4). The experimental structure of PTX adopting a hairpin motif was used as the ligand and the structure of human Na,K-ATPase in E1-3Na-ATP state [32] was used as the receptor protein molecule. Rigid docking simulations were performed using the Patchdock server [33]. The rigid docking result suggested that the hairpin motif of PTX would bind the extracellular gate of the Na,K-ATPase protein in a similar location to ouabain (Larson *et al.,* 2013).

The cyclic ether of PTX potentially forms hydrogen bonds, while the hydrocarbon chains are protected by hydrophobic transmembrane alpha-helices. Although PTX occupies a similar location as ouabain, PTX does not block the transport pathway but

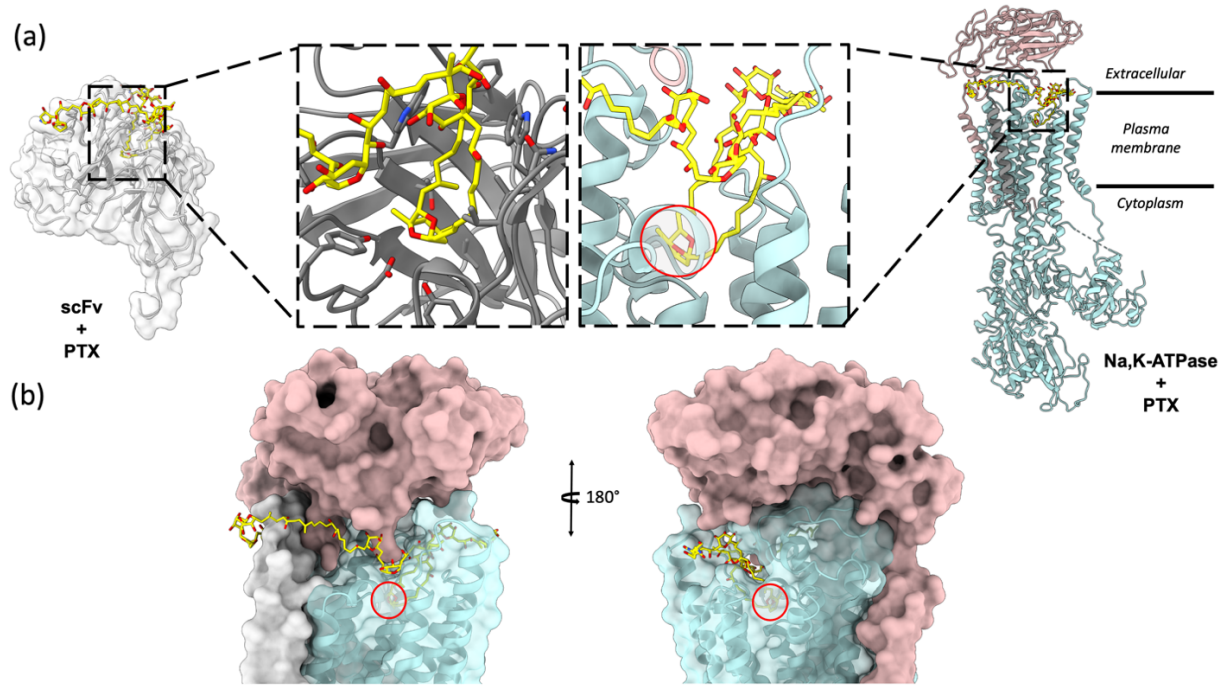

Figure 6.4: Molecular docking of PTX to Na,K-ATPase. (A) Comparison of binding modes of PTX to scFv and Na,K – ATPase. The hairpin motif of PTX shown as yellow sticks interacts with both scFv shown as white surface and Na, K – ATPase shown as cyan and salmon pink ribbons. (B) Surface representation of Na,K-ATPase shows that the hairpin motif of PTX binds the extracellular gate of the pump in a plug-like manner.

instead is known to convert the transporter to a passive channel. Outside the extracellular gate, the two tails of PTX are between the alpha and beta subunits of Na,K-ATPase. Flexible docking simulations using the linear structure of PTX were also performed using Autodock Vina[34] to support the result of the rigid binding simulation generated by Patchdock (Figure 6.5). The flexible docking results indicated that PTX adopts a similar hairpin motif again predicted to occupy the same site as above in the Na,K-ATPase. These docking simulations are consistent with previously reported functional assays [35,36].

Both the rigid and flexible binding simulations suggest that PTX's hairpin motif could be necessary for binding Na,K-ATPase, leading to a possible explanation for the cytotoxic effects of PTX.

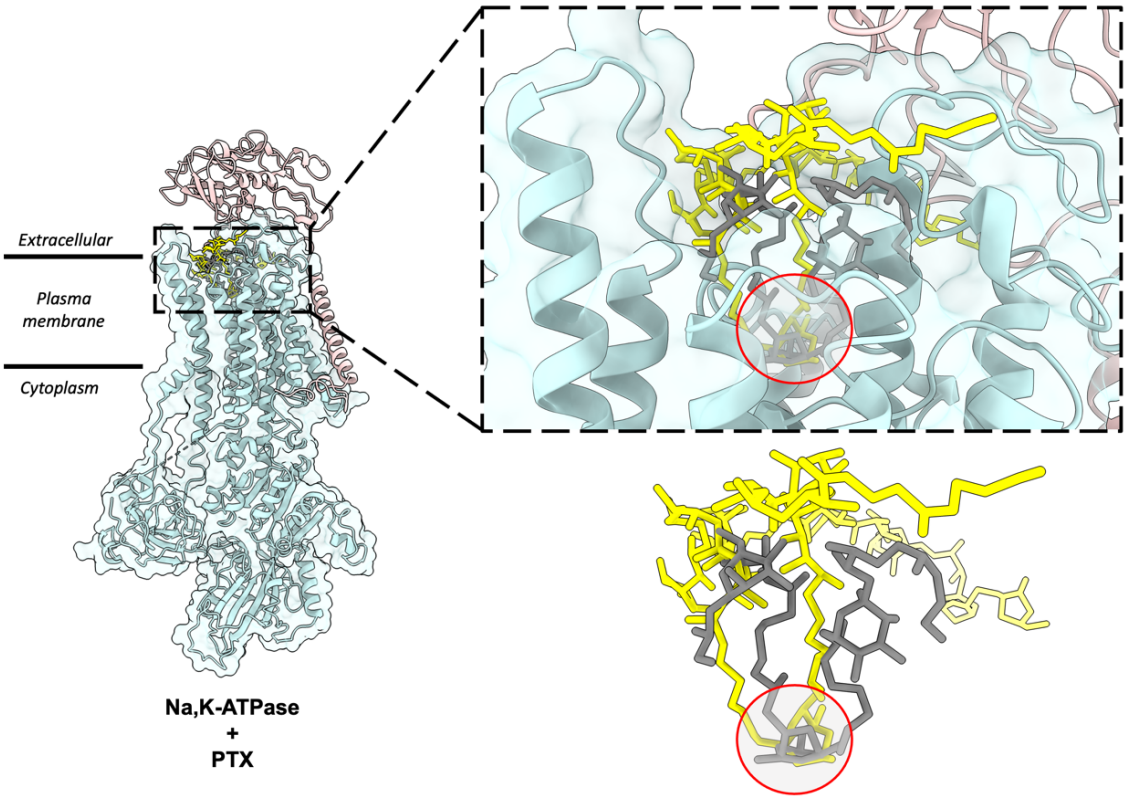

Figure 6.5: Comparison of top docking solutions from patchdock and autodock vina. The patchdock solution (yellow sticks) and vina solution (grey sticks) show that the finger motif of PTX binds to the extracellular gate of the Na,K-ATPase. In both solutions, the double ring (highlighted by red circle) interacts with Na,K-ATPase by forming hydrogen bonds and the surrounding helices form hydrophobic interactions with the hydrocarbon chains of the hairpin motif.

Discussion

The findings of this study provide significant insights into the interaction between PTX and Na,K-ATPase. The MicroED structure of the PTX-scFv complex indicates that the hydrophobic region of PTX adopts a hairpin motif. PTX binds to the scFv by forming several key interactions with amino acid residues in the complementarity-determining regions (CDRs) of the scFv. In particular, PTX binds to the CDR H3 loop of the scFv, which is known to be a critical region for antigen binding (Figure 2B). The results of the molecular docking simulations suggest that this same hairpin fold is necessary for PTX binding to the extracellular gate of Na,K-ATPase. This interaction is likely an essential step in the mechanism by which PTX converts Na,K-ATPase into a passive ion channel. This corroborates earlier reports that this region of PTX is likely chiefly responsible for the conversion of Na,K-ATPase [37,38]. The docking simulations performed in this study suggest that PTX is able to bind Na,K-ATPase in the E1-3Na-ATP state, which has a closed extracellular gate and should be less favored for PTX binding. In future studies, it will be important to determine differences in how PTX binds other states in the catalytic cycle of Na,K-ATPase. For instance, previous studies suggested that PTX has the highest affinity for the E2P conformation of Na,K-ATPase where the extracellular gate is open (Artigas & Gadsby, 2004; Rakowski et al., 2007). Overall, this study represents an important step towards a better understanding of the molecular mechanisms involved in PTX binding and its effects on Na,K-ATPase.

The use of scFv in this study allowed for the determination of the 3D structure of the scFv-PTX complex using MicroED. The scFv-PTX complex was crystallized using the

hanging drop vapor diffusion method, and the crystals were thinned using cryogenic FIB milling prior to MicroED diffraction. The needle-shaped crystals of the scFv-PTX complex that were obtained for this study were typically thin (3-5 μm) and long (several hundred microns) and they formed in bundles. Such morphologies are extremely challenging for analyses by x-ray crystallography, often leading to multiple lattices and weak scattering. Using MicroED and FIB milling was advantageous in this case because the entire crystal bundle could be transferred to the EM grid and crystal sites were accessed by using a FIB mill to generate crystal lamellae and ultimately a MicroED structure.

The detailed structural information obtained from our MicroED study could aid in the creation of new inhibitors that block the binding of PTX to Na,K-ATPase, thus preventing its toxic effects. Additionally, the knowledge gained from this study can be applied to develop methods for identifying and monitoring the accumulation of PTX and its analogues in the environment, potentially preventing harmful exposure to both humans and marine life. Significantly, this study reinforces the utility of MicroED as a powerful tool for revealing the structures of important biomolecules, such as the long-awaited structure of palytoxin, which has been elusive to x-ray crystallography.

Methods and Materials

Materials

All reagents were made with MilliQ water. Palytoxin was purchased from Fuji Film (Japan). Crystallization reagents were purchased from Hampton Research (Aliso Viejo, CA). Monolith protein labeling kit RED-NHS 2nd generation was purchased from NanoTemper Technologies (Munich, Germany).

Microscale thermophoresis

The anti-PTX scFv was prepared in 25 mM HEPES (pH 7.4), 150 mM NaCl at a concentration of 13 μM, and labeled with RED-NHS dye (NanoTemper) . PTX was prepared in 25 mM HEPES (pH 7.4), 150 mM NaCl at a concentration of 93 μM. Labeled scFv was diluted to 80 nM and added in a 1:1 ratio to a dilution series of 46.5 μM down to 4.65 x 10^-15 μM of PTX and 0 μM of PTX. Mixtures were loaded into premium capillaries (Monolith Capillaries, NanoTemper Technologies). Thermophoresis was measured at 21°C for 15 sec with 50% LED power and 100% (auto-detect) power.

Crystallization

The complex was purified by size-exclusion chromatography and the elution fractions were concentrated to 10 mg/mL. Palytoxin was incubated with scFv at a 2:1 molar ratio for 30 minutes at room temperature. A sparse matrix screening hit was identified in the PEGRxHT well condition C01 (Hampton Research) by sitting drop vapor diffusion using a Mosquito crystallization robot. This condition was optimized for robust crystallization using hanging drop vapor diffusion. In the final condition, the complex was crystallized by mixing with 27 % Jeffamine ED-2001 pH 7.0, and 100 mM sodium citrate tribasic dihydrate pH 5.6 in 1.5 uL drops with a 2:1 sample-to-mother liquor ratio.

Cryo-preservation

The cover slip with crystal drop was removed from the screening tray and the drop was gently applied to a Cu200 R2/2 holey carbon EM grid (quantifoil). The EM grid was negatively glow-discharged prior to sample application. The grid was blotted in a Leica

GP2 set to 95% humidity and 12°C and plunge-frozen into liquid ethane. The sample was stored in liquid nitrogen until further use.

Machining crystal lamellae using the cryo-FIB/SEM

The vitrified EM grid was loaded into a Thermo Fisher Aquilos dual-beam FIB/SEM operating at cryogenic temperature following established procedures [28]. The sample was sputter coated with a thin layer of platinum to preserve the sample during imaging and ion beam milling. A whole-grid atlas of the drop was acquired by the SEM and potential milling sites were selected. The targeted crystal and surrounding media were milled into a thin lamella using the gallium ion beam. The first stage of milling used a beam current of 0.5 nA and gradually decreased to a minimum of 10 pA as the lamella became thinner at later stages of milling. The final lamellae were 7 µm wide and 200 nm thick.

MicroED Data Collection

Grids with milled lamellae were transferred to a cryogenically cooled Thermo Fisher Scientific Titan Krios G3i TEM operating at an accelerating voltage of 300 kV. The Krios was equipped with a field emission gun and a Falcon4 direct electron detector. A low magnification atlas of the grid was acquired using EPUD (Thermo Fisher) to locate milled lamellae. The stage was translated to the lamellae position and the eucentric height was set. The 100 µm selected area aperture was inserted and centered on the crystal to block background reflections. In diffraction mode, the beam was defined using a 50 µm C2 aperture, a spotsize of 11, and a beam diameter of 20 µm. MicroED data were collected

by continuously rotating the stage at 0.2 ° / s. MicroED data from three different crystal lamellae were selected for downstream data processing.

MicroED Data Processing

Diffraction movies in MRC format were converted to SMV format using MicroED tools (https://cryoem.ucla.edu/microed) [28,41]. The diffraction dataset was indexed and integrated in *XDS* [42]. Integrated intensities from three different crystal lamella were merged and scaled in *XSCALE* [43].

Structure solution and refinement

Phases for the MicroED reflections were determined by molecular replacement in PHASER [44] using anti-Mcl1 scFv (PDB 6QF9) as the search model [30]. The solution was space group $P4_12_12$ and unit cell dimensions 69.95, 69.95, 289.48 (a, b, c) (Å) and 90, 90, 90 (α, β, γ) (°). The first refinement was performed with Coot and phenix.refine [31] using isotropic B-factors and electron scattering factors. Occupancies were refined for alternative side chain conformations and SO_4 and waters were manually placed during refinement. The final refinement used anisotropic B-factors, automatic water picking, and electron scattering factors and resulted in R_{work}/R_{free} = 0.2830/0.3229 and resolution of 3.2 Å.

Molecular docking

A human Na,K-ATPase structure in E1 state (PDB ID: 7E21) [32] without cofactors, waters and ligands was used as a receptor molecule and the 3D model of PTX from the scFv-PTX complex was used as a rigid ligand. For patchdock simulations, the PDB files of

receptor and ligand molecules were submitted to the patchdock server (http://bioinfo3d.cs.tau.ac.il/PatchDock/php.php). The clustering RMSD was selected to be 4.0 and the complex type was selected to be protein-ligand complex. The results were emailed within 24h with a list of potential binding solutions of PTX numbered on the basis of geometric shape complementarity score. Higher complementarity scores indicate less possibility of steric clashes in the solution.

Full length PTX did not provide any solution when simulation was performed using Autodock vina, hence, a flexible fragment of PTX molecule consisting of only the hairpin motif was used to perform the binding simulations. The receptor and ligand were prepared using the MGL tools suite (https://ccsb.scripps.edu/mgltools/) and saved as pdbqt files. The receptor file contained partial charges and polar hydrogens. Any cofactors, waters and ligands were removed. For the ligand file, polar hydrogens were added and all the original torsion angles were kept intact. The receptor was treated as rigid while the ligand fragment was flexible. The simulations were run and the solutions were scored on the basis of binding energy (kcal/mol).

References

1. Habermann, E. Palytoxin acts through Na+, K+-ATPase. *Toxicon* **27**, 1171–1187 (1989).

2. Christian Skou, J. I. & Esmann, M. I. The Na,K-ATPase. *J Bioenerg Biomembr* **24**, (1992).

3. Tubaro, A., Sosa, S. & Hungerford, J. *Toxicology and diversity of marine toxins. Veterinary toxicology: basic and clinical principles*. (Academic press, 2012).

4. Usami, M. *et al.* Palytoxin analogs from the dinoflagellate Ostreopsis siamensis. *J Am Chem Soc* **117**, 5389–5390 (1995).

5. Taniyama, S. *et al.* Ostreopsis sp., a possible origin of palytoxin (PTX) in parrotfish Scarus ovifrons. *Toxicon* **42**, 29–33 (2003).

6. Ukena, T. *et al.* Structure Elucidation of Ostreocin D, a Palytoxin Analog Isolated from the Dinoflagellate Ostreopsis siamensis. *Biosci Biotechnol Biochem* **65**, 2585–2588 (2014).

7. Moore, R. E. & Scheuer, P. J. Palytoxin: A New Marine Toxin from a Coelenterate. *Science (1979)* **172**, 495–498 (1971).

8. Patocka, J., Gupta, R. C., Wu, Q. & Kuca, K. Toxic potential of palytoxin. *Journal of Huazhong University of Science and Technology [Medical Sciences]* **35**, 773–780 (2015).

9. Deeds, J. R. & Schwartz, M. D. Human risk associated with palytoxin exposure. *Toxicon* **56**, 150–162 (2010).

10. Fukui, M., Murata, M., Inoue, A., Gawel, M. & Yasumoto, T. Occurrence of palytoxin in the trigger fish Melichtys vidua. *Toxicon* **25**, 1121–1124 (1987).

11. Rhodes, L., Towers, N., Briggs, L., Munday, R. & Adamson, J. Uptake of palytoxin-like compounds by shellfish fed Ostreopsis siamensis (Dinophyceae). *N Z J Mar Freshwater Res* **36**, 631–636 (2002).

12. Hoffmann, K. *et al.* A case of palytoxin poisoning due to contact with zoanthid corals through a skin injury. *Toxicon* **51**, 1535–1537 (2008).

13. Rumore, M. M. & Houst, B. M. Palytoxin poisoning via inhalation in pediatric siblings. *Int J Case Rep Images* **5**, 501–504 (2014).

14. Ciminiello, P. *et al.* The Genoa 2005 Outbreak. Determination of Putative Palytoxin in Mediterranean Ostreopsis o vata by a New Liquid Chromatography Tandem Mass Spectrometry Method. *Anal Chem* **78**, 6153–6159 (2006).

15. Böttinger, H., Béress, L. & Habermann, E. Involvement of (Na+ + K+)-ATPase in binding and actions of palytoxin on human erythrocytes. *BBA - Biomembranes* **861**, 165–176 (1986).

16. Riobó, P. & Franco, J. M. Palytoxins: Biological and chemical determination. *Toxicon* **57**, 368–375 (2011).

17. Artigas, P. & Gadsby, D. C. Na+/K+-pump ligands modulate gating of palytoxin-induced ion channels. *Proc Natl Acad Sci U S A* **100**, 501–505 (2003).

18. Wang, X. & Horisberger, J. D. Palytoxin effects through interaction with the Na,K-ATPase in Xenopus oocyte. *FEBS Lett* **409**, 391–395 (1997).

19. Lazzaro, M., Tashjian Jr., A., Fujiki, H. & Levinef, L. Palytoxin : An Extraordinarily Potent Stimulator of. *Endocrinology* **120**, 1338–1345 (1987).

20. Aligizaki, K., Katikou, P., Milandri, A. & Diogène, J. Occurrence of palytoxin-group toxins in seafood and future strategies to complement the present state of the art. *Toxicon* **57**, 390–399 (2011).

21. Tubaro, A. *et al.* Case definitions for human poisonings postulated to palytoxins exposure. *Toxicon* **57**, 478–495 (2011).

22. Wiles, J. S., Vick, J. A. & Christensen, M. K. Toxicological evaluation of palytoxin in several animal species. *Toxicon* **12**, 427–433 (1974).

23. Lau, C. O. *et al.* Lophozozymus pictor toxin: A fluorescent structural isomer of palytoxin. *Toxicon* **33**, 1373–1377 (1995).

24. Levine, L., Fujiki, H., Gjika, H. B. & Van Vunakis, H. Production of antibodies to palytoxin: Neutralization of several biological properties of palytoxin. *Toxicon* **25**, 1273–1282 (1987).

25. Shi, D., Nannenga, B. L., Iadanza, M. G. & Gonen, T. Three-dimensional electron crystallography of protein microcrystals. *Elife* **2**, e01345 (2013).

26. Nannenga, B. L., Shi, D., Leslie, A. G. W. & Gonen, T. High-resolution structure determination by continuous-rotation data collection in MicroED. *Nat Methods* **11**, 927–930 (2014).

27. Martynowycz, M. W., Clabbers, M. T. B., Unge, J., Hattne, J. & Gonen, T. Benchmarking the ideal sample thickness in cryo-EM. *Proc Natl Acad Sci U S A* **118**, 1–7 (2021).

28. Martynowycz, M. W., Zhao, W., Hattne, J., Jensen, G. J. & Gonen, T. Collection of Continuous Rotation MicroED Data from Ion Beam-Milled Crystals of Any Size. *Structure* **27**, 545-548.e2 (2019).

29. Kabsch, W. XDS. *Acta Crystallogr D Biol Crystallogr* **66**, 125–132 (2010).

30. Luptak, J. *et al.* Antibody fragments structurally enable a drug-discovery campaign on the cancer target Mcl-1. *Acta Crystallographica Section D* **75**, 1003–1014 (2019).

31. Afonine, P. V. *et al.* Towards automated crystallographic structure refinement with phenix.refine. *Acta Crystallogr D Biol Crystallogr* **68**, 352–367 (2012).

32. Guo, Y. *et al.* Cryo-EM structures of recombinant human sodium-potassium pump determined in three different states. *Nat Commun* **13**, (2022).

33. Schneidman-Duhovny, D., Inbar, Y., Nussinov, R. & Wolfson, H. J. PatchDock and SymmDock: servers for rigid and symmetric docking. *Nucleic Acids Res* **33**, W363–W367 (2005).

34. Trott, O. & Olson, A. J. AutoDock Vina: Improving the speed and accuracy of docking with a new scoring function, efficient optimization, and multithreading. *J Comput Chem* NA-NA (2009) doi:10.1002/jcc.21334.

35. Vale, C. & Ares, I. R. Biochemistry of palytoxins and ostreocins. *Phycotoxins: chemistry and biochemistry* 95–118 (2007).

36. Ramos, V. & Vasconcelos, V. Palytoxin and Analogs: Biological and Ecological Effects. *Mar Drugs* **8**, 2021–2037 (2010).

37. Harmel, N. & Apell, H.-J. Palytoxin-induced Effects on Partial Reactions of the Na,K-ATPase. *J Gen Physiol* **128**, 103–118 (2006).

38. Habermann, E., Ahnert-Hilger, G., Chhatwal, G. S. & Beress, L. Delayed haemolytic action of palytoxin general characteristics. *Biochimica et Biophysica Acta (BBA) - Biomembranes* **649**, 481–486 (1981).

39. Artigas, P. & Gadsby, D. C. Large Diameter of Palytoxin-induced Na/K Pump Channels and Modulation of Palytoxin Interaction by Na/K Pump Ligands. *Journal of General Physiology* **123**, 357–376 (2004).

40. Rakowski, R. F. *et al.* Sodium Flux Ratio in Na/K Pump-Channels Opened by Palytoxin. *J Gen Physiol* **130**, 41–54 (2007).

41. Hattne, J. *et al.* MicroED data collection and processing. *Acta Crystallogr A Found Adv* **71**, 353–360 (2015).

42. Kabsh, W. XDS. *Acta Crystallogr D Biol Crystallogr* **66**, 125–132 (2010).

43. Kabsch, W. Integration, scaling, space-group assignment and post-refinement. *Acta Crystallogr D Biol Crystallogr* **66**, 133–144 (2010).

44. McCoy, A. J. *et al.* Phaser crystallographic software. *J Appl Crystallogr* **40**, 658–674 (2007).

Concluding Remarks

Crystallography is a widely used technique for determining the structures of both small and large molecules such as proteins. MicroED, still an emerging technique, provides a solution for molecules that form crystals that are too small for X-ray diffraction. Difficult-to-handle samples, including those embedded in viscous media and sensitive to mechanical stress, can be challenging to work with in MicroED. Moreover, certain crystals, especially those that resemble sheets, may exhibit a preferred orientation on the EM grid carbon support film, which can limit the reciprocal space available for sampling the crystal lattice. These various challenges are intrinsic to MicroED, and in large part are due to the way in which MicroED samples are prepared following conventional procedures. To this end, there is currently a demand for the development of innovative approaches for MicroED sample preparation.

The novel approach for crystallizing molecules that we named suspended drop crystallization, presented in Chapter 4, provides an alternative sample preparation workflow that can alleviate the issues mentioned above. However, suspended drop crystallization incorporates FIB milling, which unfortunately is a time intensive phase of this experimental procedure. Automating the FIB milling instrument so that sample lamellae can be generated around the clock is an attractive avenue that will lead to more rapid determination of novel structures. Additionally, the apparatus that was designed for suspended drop crystallization is compatible with high throughput screening of crystallization conditions and even the implementation of robotics. With continued development of suspended drop crystallization, it is reasonable to envisage that one day, facilities could be established that automate 1) sparse matrix screening of suspended

crystallization drops, 2) FIB milling, and 3) MicroED data collection. A facility of this sort could make it possible to determine molecular structure by MicroED upon the first instances of observable crystal growth. Advanced machine learning and image analysis programs would need to be developed in parallel to achieve this possible paradigm.